Oxide hetero-interfaces: superconductivity, magnetism, defects and Lifshitz transition

A. Taraphder

Department of Physics and Centre for Theoretical Studies
IIT Kharagpur

http://www.phy.iitkgp.ernet.in/physics/home/faculty/home.php?id=arghya

N. Mohanta, **A. Taraphder**, *J. Phys. Cond. Mat.* **26**, 025705 (2014); ***ibid***. **26**, 215703 (2014)

N. Mohanta and **A. Taraphde**r, *Europhys. Lett*. 108, 60001 (2014).

* N. Mohanta, S. Bandyopadhyay, S. Lal and **A. Taraphder,** *arXiv:*1407.6539 (2014)

N. Mohanta and **A. Taraphder**, *Phys. Rev. B*. 92, 174531 (2015)

* G. Daptary**,** **AT** et al. *Phys Rev B* **94**, 085104 (2016)

S. Nandy, S. Acharya, D. Dey, **A Taraphder**, *Phys. Rev. B* ***94**, 155103* (2016)

* S. Kumar, **AT** et al. *Phys. Rev. B.* 95, 174502 (2017)

* Not included in the talk

Interfaces: ***AlO_2 / LaO(n-type) or SrO(p-type) / TiO_2***

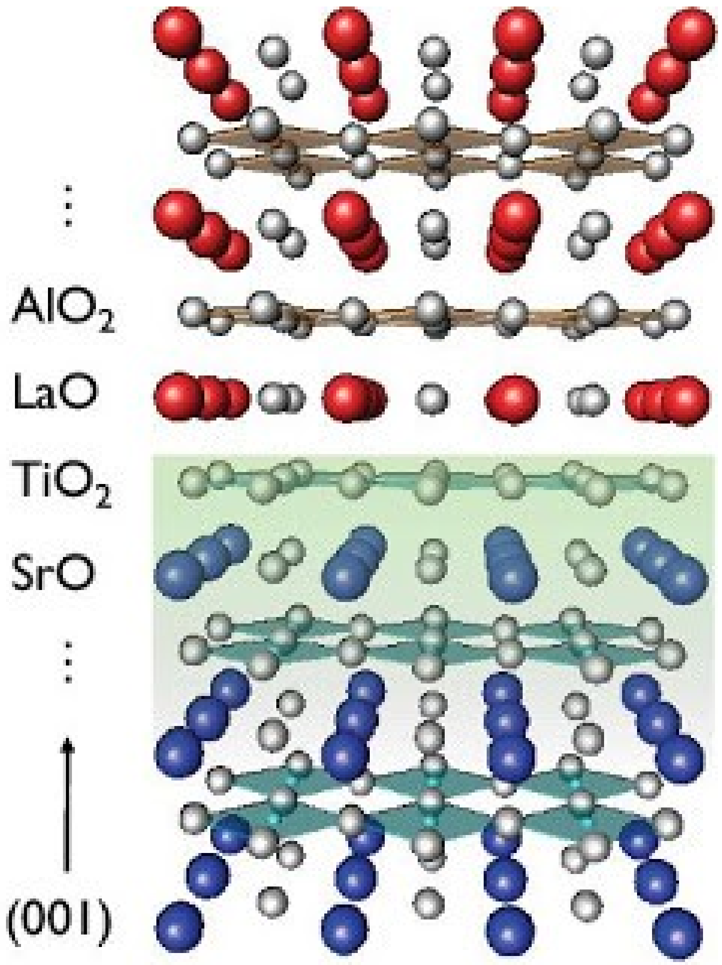

The n-type heterointerface

$LaAlO_3$:
Band Insulator
(Band gap = 5.6 eV)
Non-magnetic

→ Metallic conduction

$SrTiO_3$:
Band Insulator
(Band gap = 3.2 eV)
Non-magnetic

Oxides for semiconductors: an odd exchange

- Semiconductors: Brawn but no brain. Excellent materials with good control. No exciting physics.
- Correlated Oxides: Intelligent but wayward. Not controllable, poor materials.
- Marriage of semiconducting Oxides: A marriage in heaven or hell?
- The Classic conundrum: Super-offspring ? 50:50 chance.

Discovery: 2DEL at the interface, the first emergence

A high-mobility electron gas at the $LaAlO_3/SrTiO_3$ heterointerface

A. Ohtomo[1,2,3] **& H. Y. Hwang**[1,3,4]

[1]*Bell Laboratories, Lucent Technologies, Murray Hill, New Jersey 07974, USA*
[2]*Institute for Materials Research, Tohoku University, Sendai, 980-8577, Japan*
[3]*Japan Science and Technology Agency, Kawaguchi, 332-0012, Japan*
[4]*Department of Advanced Materials Science, University of Tokyo, Kashiwa, Chiba, 277-8651, Japan*

Nature **427**, 423 (2004)

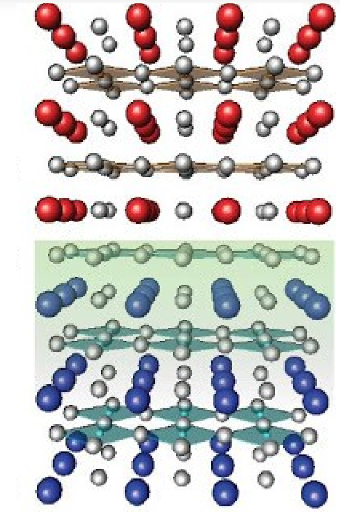

Less O vacancy, less carriers

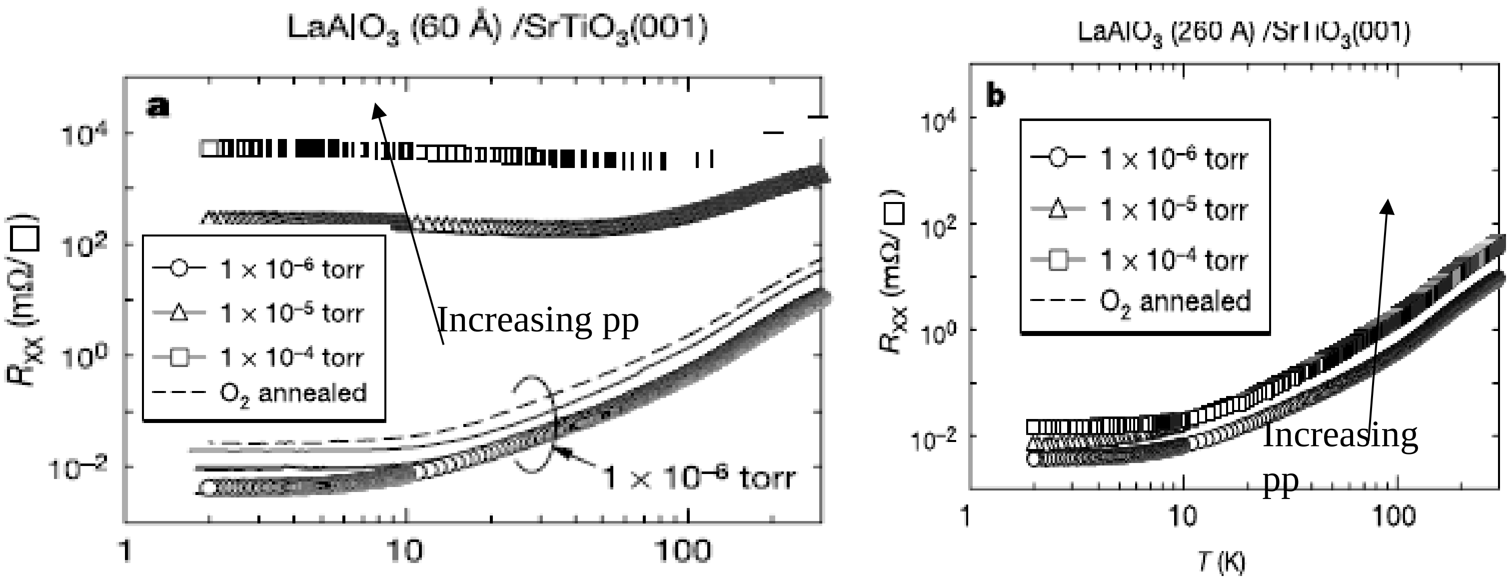

Figure 2 Transport properties of the $(LaO)^+/(TiO_2)^0$ interface for different oxygen partial pressures p_{O_2} during growth at 10^{-4}, 10^{-5}, and 10^{-6} torr, as well as for 10^{-6} torr growth followed by annealing in 1 atm of O_2 at 400 °C for 2 h. **a**, **c**, **e**, The temperature dependence of $R_{xx}(T)$, $R_H(T)$ and $\mu_H(T)$ for the interface between 60-Å-thick $LaAlO_3$ and $SrTiO_3$, respectively. **b**, **d**, **f**, The temperature dependence of $R_{xx}(T)$, $R_H(T)$ and $\mu_H(T)$ for the interface between 260-Å-thick $LaAlO_3$ and $SrTiO_3$, respectively.

Applications in devices

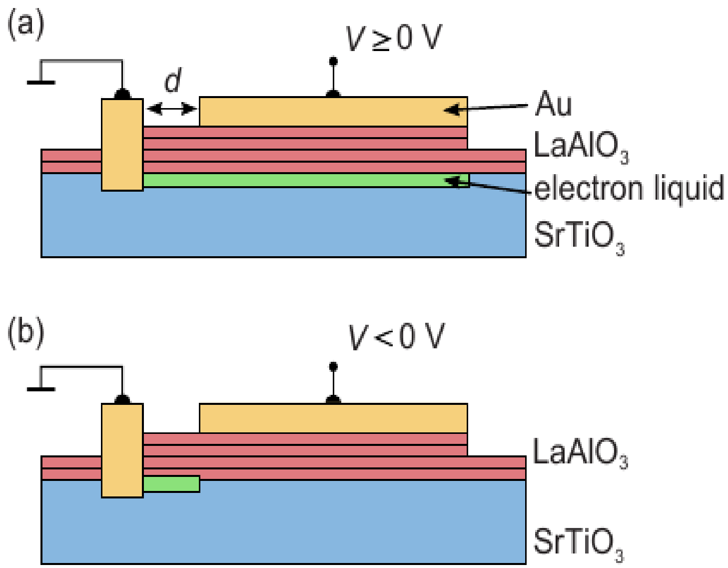

FIG. 1. (Color online) Illustration of the operation of a device consisting of 4 uc $LaAlO_3$ layer deposited on $SrTiO_3$. Gold layers provide contacts to the interface and to the top of the $LaAlO_3$. In forward direction, with a positive voltage applied to the top contact (a), a conducting electron system is formed at the $LaAlO_3$–$SrTiO_3$ interface, which is electrically separated from the top electrode by 4 uc of $LaAlO_3$ only. In reverse direction, with a negative voltage applied to the top electrode (b), the electron system is depleted and, undergoing a metal-insulator transition, becomes completely insulating. The effective length of the insulating region is enlarged.

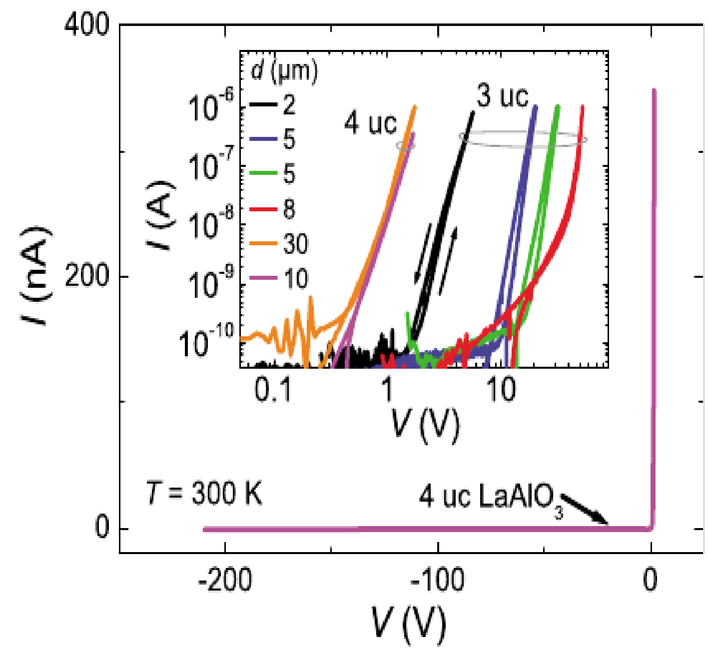

FIG. 2. (Color online) Current-voltage characteristics of diodes as measured at $T=300$ K. The characteristics show a rectifying behavior with reverse breakdown voltages up to $|V|>200$ V. In the device with the 4 uc thick $LaAlO_3$ layer, the interface is conducting at $V=0$ V, and the device therefore has a much smaller turn-on voltage than the 3 uc samples (inset). The two measurements with $d=5$ μm were performed on different samples.

APL 96 183504 (2010)

Back-gated tunnel junction for dI/dV

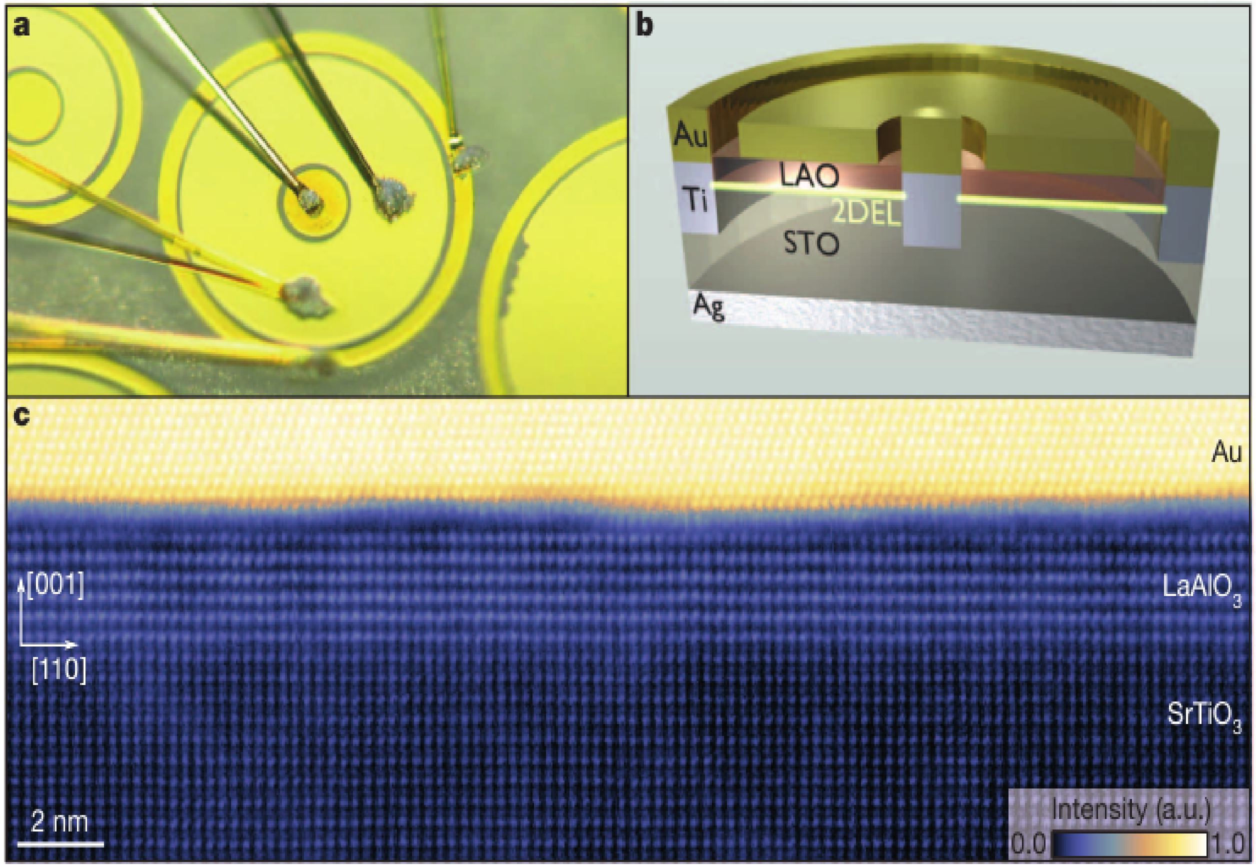

Figure 1 | Device layout. **a**, **b**, Photograph (**a**) and schematic cross section (**b**) of a typical Au–$LaAlO_3$–$SrTiO_3$ tunnel device. The broad gold ring (inner diameter, 160 μm) lies on top of the $LaAlO_3$ layer, which serves as a tunnel barrier between the 2DEL and the Au. The outer ring and the centre contact of the device are Au-covered Ti contacts to the 2DEL. **c**, Cross-sectional high-angle annular dark-field STEM image of a Au–$LaAlO_3$–$SrTiO_3$ tunnel junction. The image is taken along the $[1\bar{1}0]$ zone axis of the perovskite unit cells. a.u., arbitrary units.

Richter, et al., Nat. Lett. 502 (2013)

The critical LAO thikness puzzle: 4 layers of $LaAlO_3$

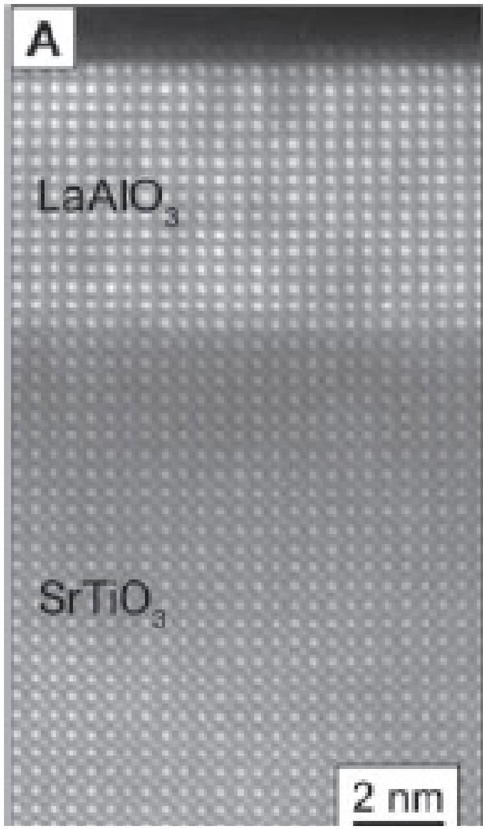

d layers of $LaAlO_3$

d big enough: conduction

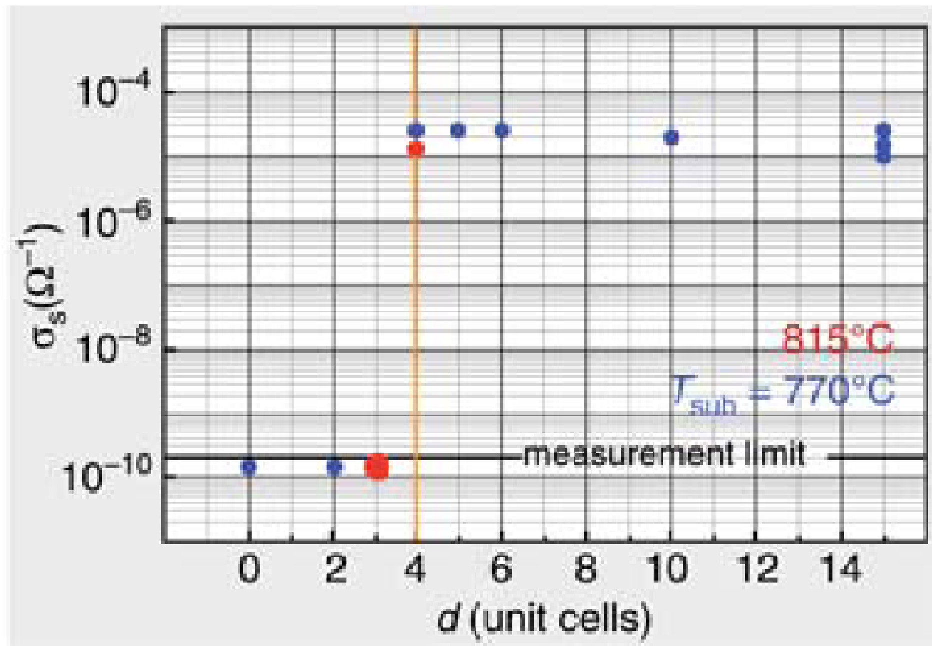

J. Mannhart et al, MRS Bull. 33 1027 (2008)

Tunable Quasi–Two-Dimensional Electron Gases in Oxide Heterostructures

S. Thiel,[1] G. Hammerl,[1] A. Schmehl,[2] C. W. Schneider,[1] J. Mannhart[1*]

Science **313**, 1942 (2006)

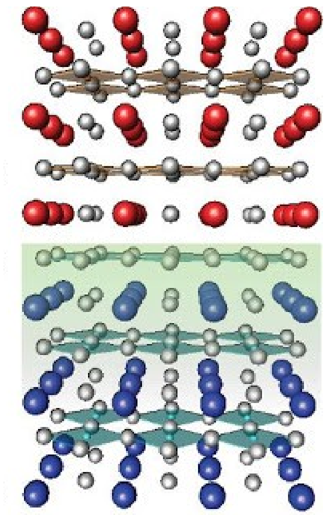

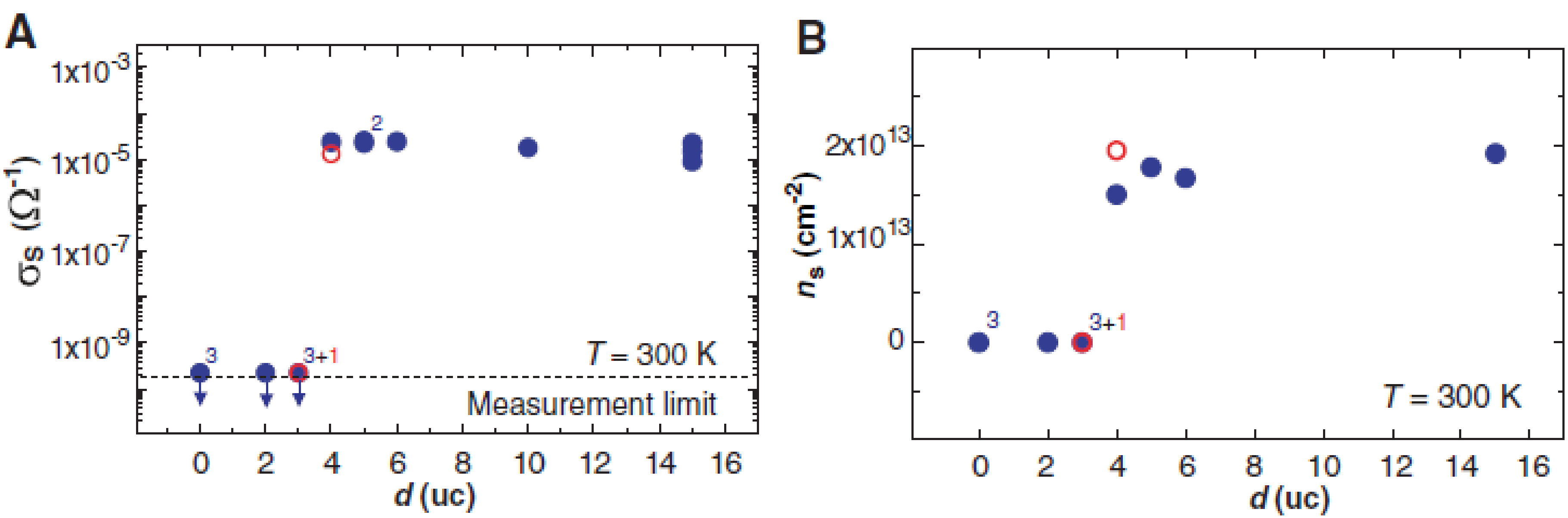

ABO_3 perovskite

crystal structure, cubic phase

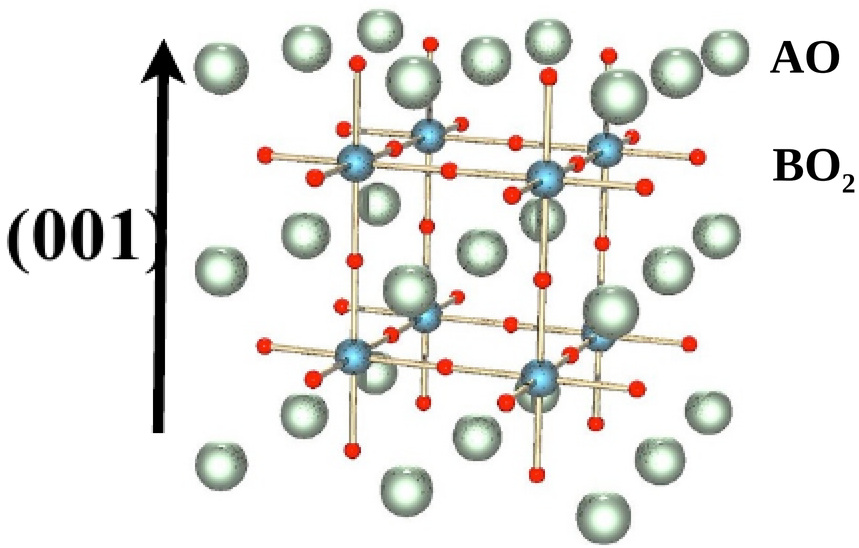

View along (001) axis

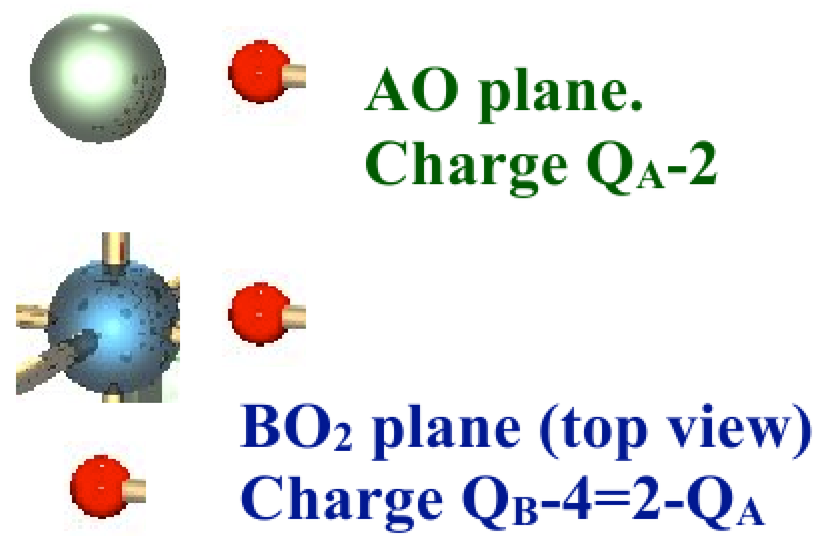

Sheets of alternating charge. 2 common cases:

Q_A=2 (A: Sr,Ca): sheet charge 0: non-polar Q_B=4

Q_A=3 (A: La, Y.) : sheet charge +/-1: polar Q_B=3

$LaAlO_3$ Q_A=3: polar

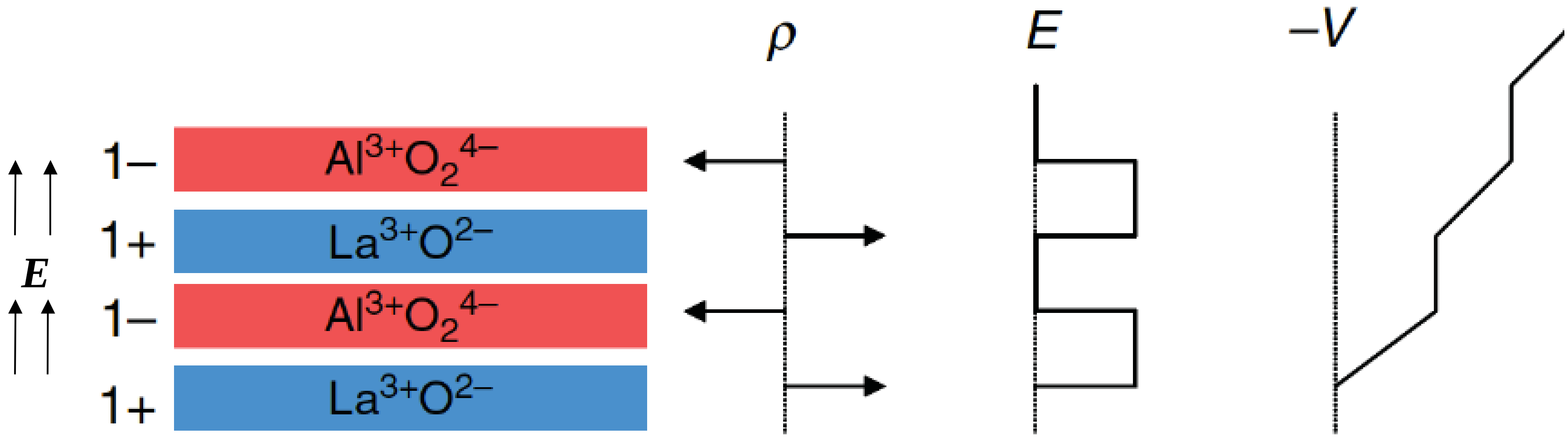

n-th layer:
$V_n = - E\, d + V_{n-1}$

$$\nabla \cdot \mathcal{E} = 4\pi \mathbf{n}$$

Alternating charged layers=>nonzero average internal field=>voltage increases with distance

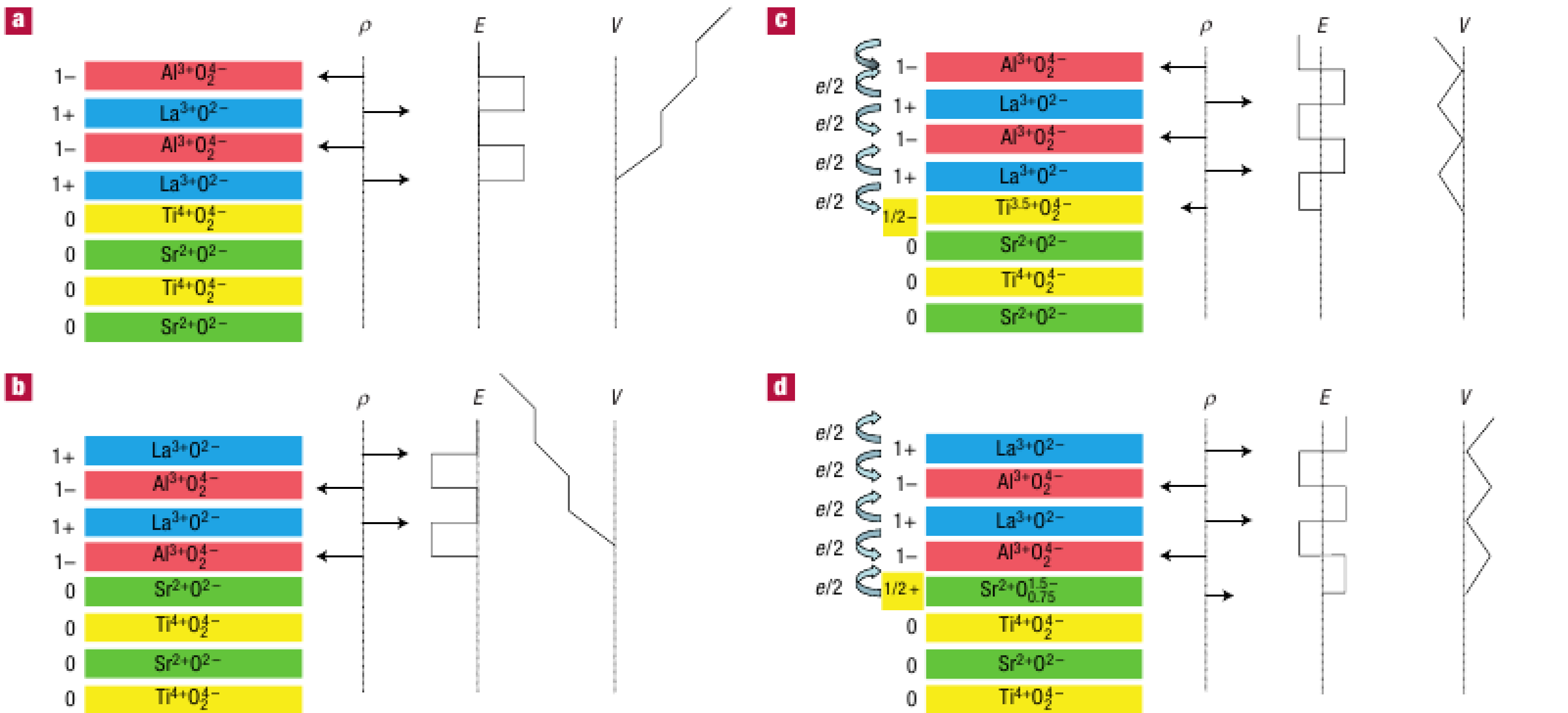

Figure 1 The polar catastrophe illustrated for atomically abrupt (001) interfaces between $LaAlO_3$ and $SrTiO_3$. a, The unreconstructed interface has neutral (001) planes in $SrTiO_3$, but the (001) planes in $LaAlO_3$ have alternating net charges (ρ). If the interface plane is $AlO_2/LaO/TiO_2$, this produces a non-negative electric field (E), leading in turn to an electric potential (V) that diverges with thickness. **b**, If the interface is instead placed at the $AlO_2/SrO/TiO_2$ plane, the potential diverges negatively. **c**, The divergence catastrophe at the $AlO_2/LaO/TiO_2$ interface can be avoided if half an electron is added to the last Ti layer. This produces an interface dipole that causes the electric field to oscillate about 0 and the potential remains finite. The upper free surface is not shown, but in this simple model the uppermost AlO_2 layer would be missing half an electron, which would bring the electric field and potential back to zero at the upper surface. The actual surface reconstruction is more complicated[21]. **d**, The divergence for the $AlO_2/SrO/TiO_2$ interface can also be avoided by removing half an electron from the SrO plane in the form of oxygen vacancies.

Nakagawa, et al. Nat. Mater. 5, 204 (2006)

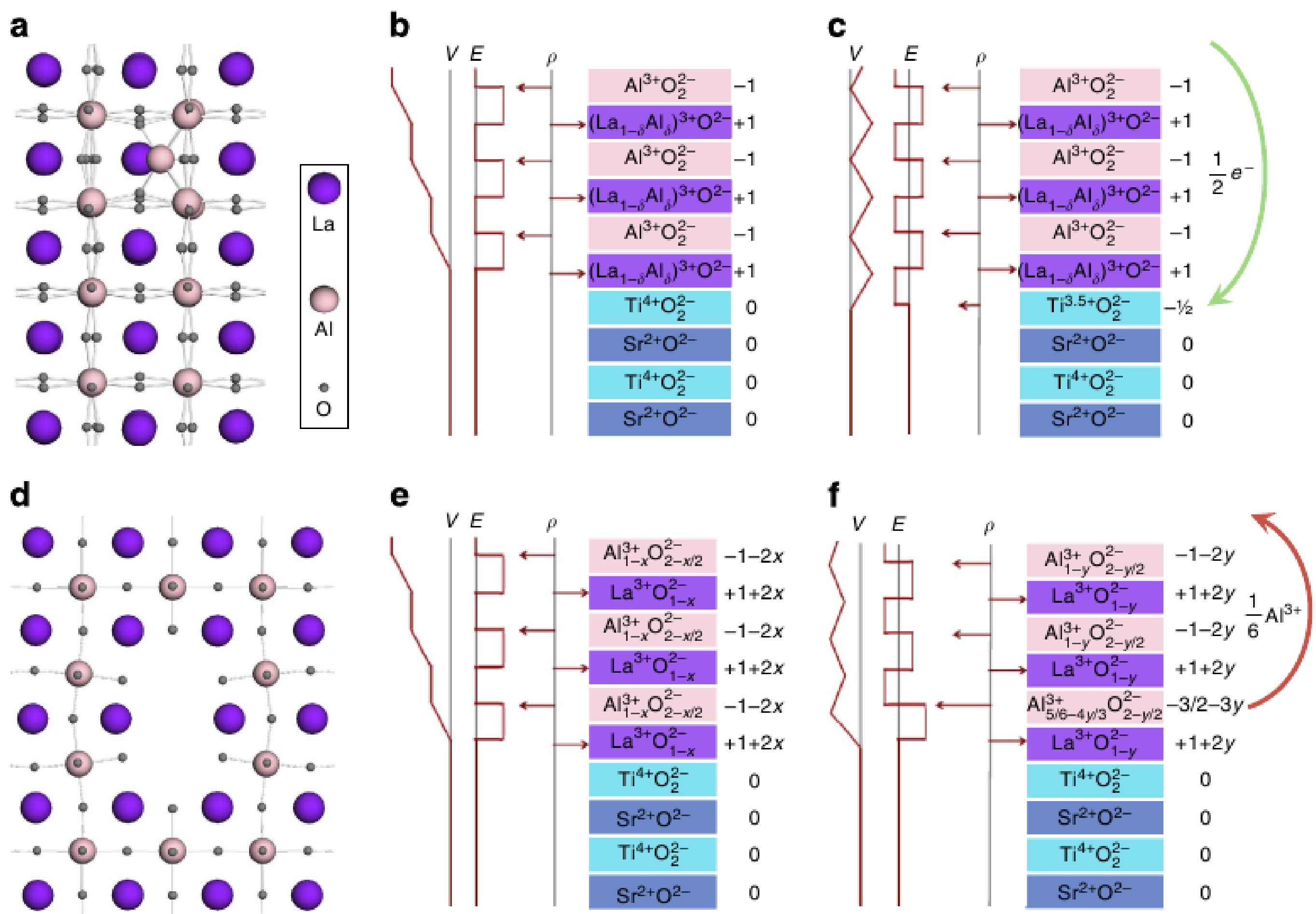

Figure 5 | Lowest energy structures and illustrations of the polar catastrophe. (**a**) In Al-rich films, aluminum substitutes for lanthanum and shifts off the cuboctahedron centre. The lowest-energy structure is shown as viewed along the [100] direction. (**b**) The alternating charges (ρ) of the (001) planes in Al-rich $La_{(1-\delta)}Al_{(1+\delta)}O_3$ and the charge neutral (001) planes in $SrTiO_3$ generates a positive average electric field (E) and a diverging potential (V). Note: $\rho/\varepsilon = \nabla \cdot E = -\nabla^2 V$. The substitution of Al^{3+} for La^{3+} does not modify the alternating polarity from that of a stoichiometric $LaAlO_3$ film. (**c**) In thick Al-rich films, the system reconstructs electronically, transferring half an electron per unit cell from the surface to the interface. (**d**) In La-rich films, Al_2O_3-vacancy complexes form, which are periodic in the [001] direction. The smallest Al_2O_3-vacancy complex is shown as viewed along the [001] direction. (**e**) The extended Al_2O_3-vacancy complexes in the unreconstructed La-rich films also remove oxygen from the nominal $(LaO)^+$ layers. The aluminum deficiency is given by $x = -2\delta/(1-\delta)$. A diverging potential results in the unreconstructed films from the alternately charged (001) planes of $La_{(1-\delta)}Al_{(1+\delta)}O_3$. (**f**) In thick La-rich films, extra aluminum vacancies can move to the interface through the Al_2O_3-vacancy complexes to screen the diverging potential. The aluminum deficiency y now depends on the stoichiometry (δ) and the film thickness.

Composition (La/Al ratio)-dependence: extrinsic carriers (O-vacancies) not necessary

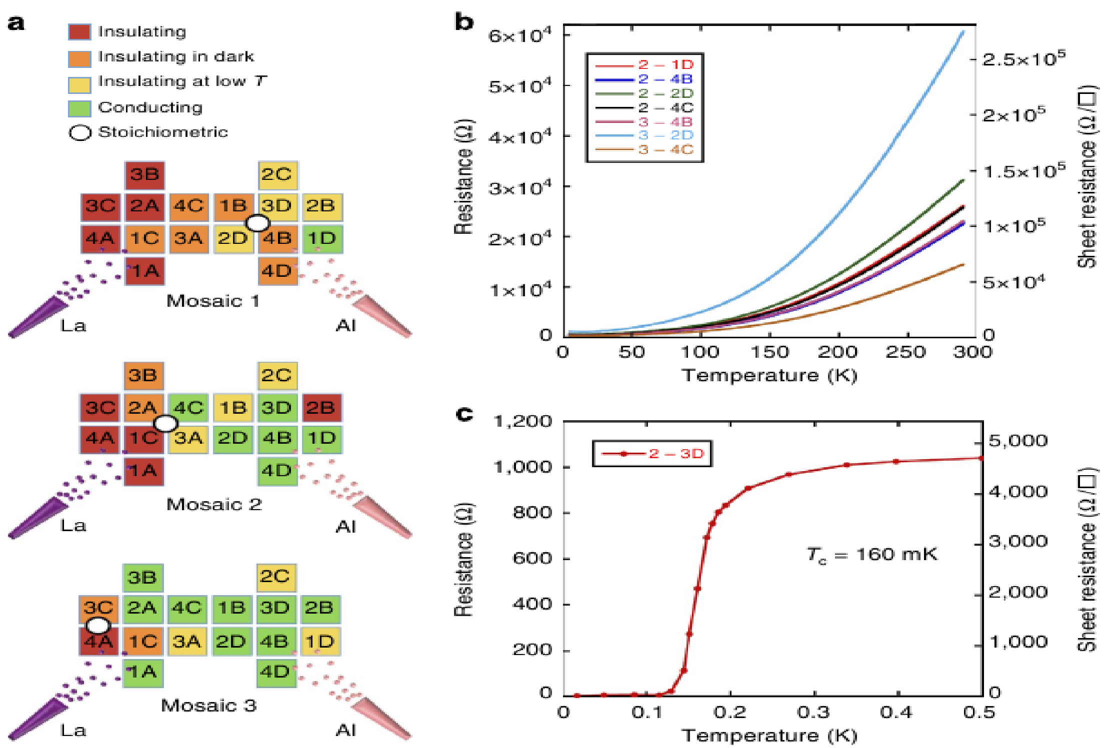

Figure 1 | Flux gradients and interfacial conductivity of mosaic samples. (**a**) Mosaic arrangement of substrates for each growth. The location of lanthanum and aluminum effusion cells relative to the mosaic of substrates is also indicated. The La/Al ratio decreases on moving from left to right across each mosaic. The position of stoichiometric $LaAlO_3$, determined by *ex situ* RBS measurements for each mosaic growth, is shown by a white circle. Samples with a conducting interface are shown in green and are only found to the right of the white circle in each mosaic. (**b**) Temperature dependence of resistance of the 2-DEL is plotted for a representative set of conducting samples from the mosaic growths. The samples are labelled with the mosaic number followed by substrate number—for example, 2-1D indicates mosaic 2, piece D of substrate 1. (**c**) A representative low-temperature resistance versus temperature plot shows the 2-DEL is superconducting. The scaling between resistance and sheet resistance is approximate.

NATURE COMMUNICATIONS | 4:2351 | DOI: 10.1038/ncomms3351 | www.nature.com/naturecommunications

Mannhart, et al., ncomms 4, 3351 (2013)

Metallic 2DEL for La/Al < 0.97

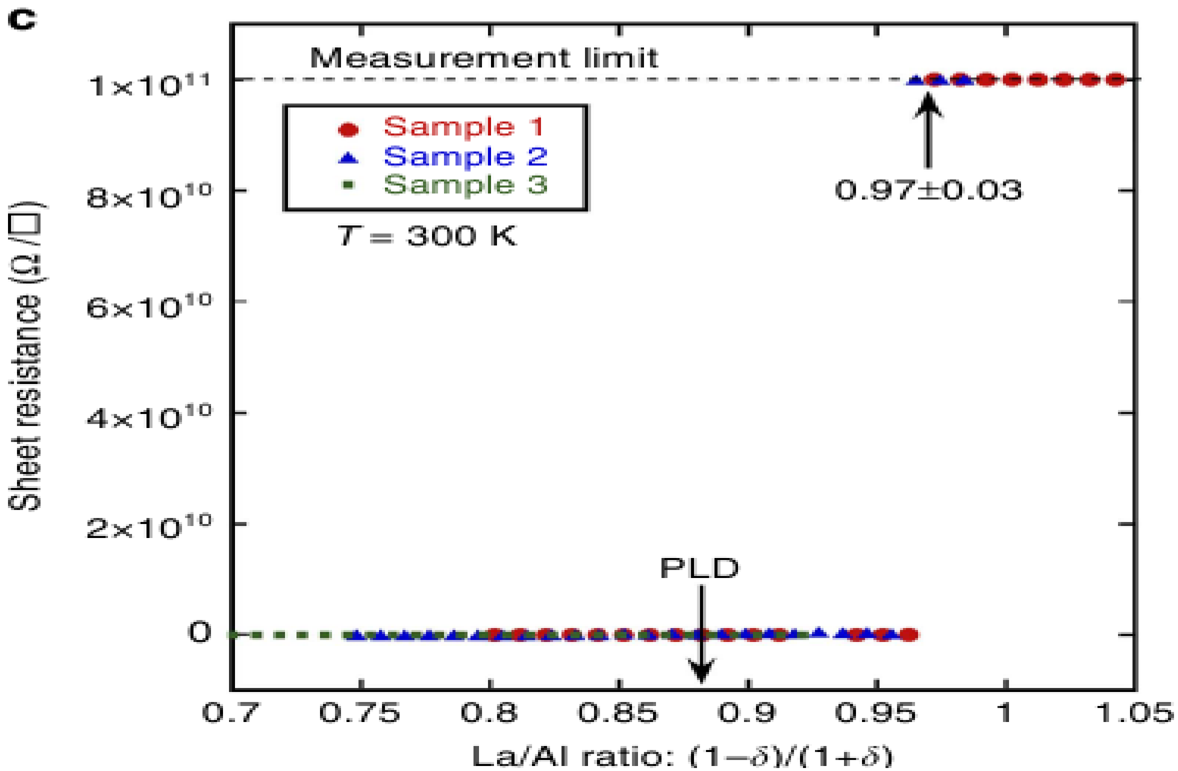

(**c**) Room temperature sheet resistance of $La_{(1-\delta)}Al_{(1+\delta)}O_3$/(001) $SrTiO_3$ interfaces obtained by local four-point resistance measurements is plotted as a function of the La/Al ratio determined by RBS measurements. A sharp jump in sheet resistance is observed at La/Al $= 0.97 \pm 0.03$, consistently in all three samples. See text for error analysis and see Supplementary Fig. S4 for resistance of conducting devices. An arrow indicates the stoichiometry of a PLD-grown companion sample similar to the samples studied in ref. 2.

Mannhart, et al. Ncomms3351 (2013)

The second emergence

Superconducting Interfaces Between Insulating Oxides

Science **317**, 1196 (2007)

N. Reyren,[1] S. Thiel,[2] A. D. Caviglia,[1] L. Fitting Kourkoutis,[3] G. Hammerl,[2] C. Richter,[2] C. W. Schneider,[2] T. Kopp,[2] A.-S. Rüetschi,[1] D. Jaccard,[1] M. Gabay,[4] D. A. Muller,[3] J.-M. Triscone,[1] J. Mannhart[2]*

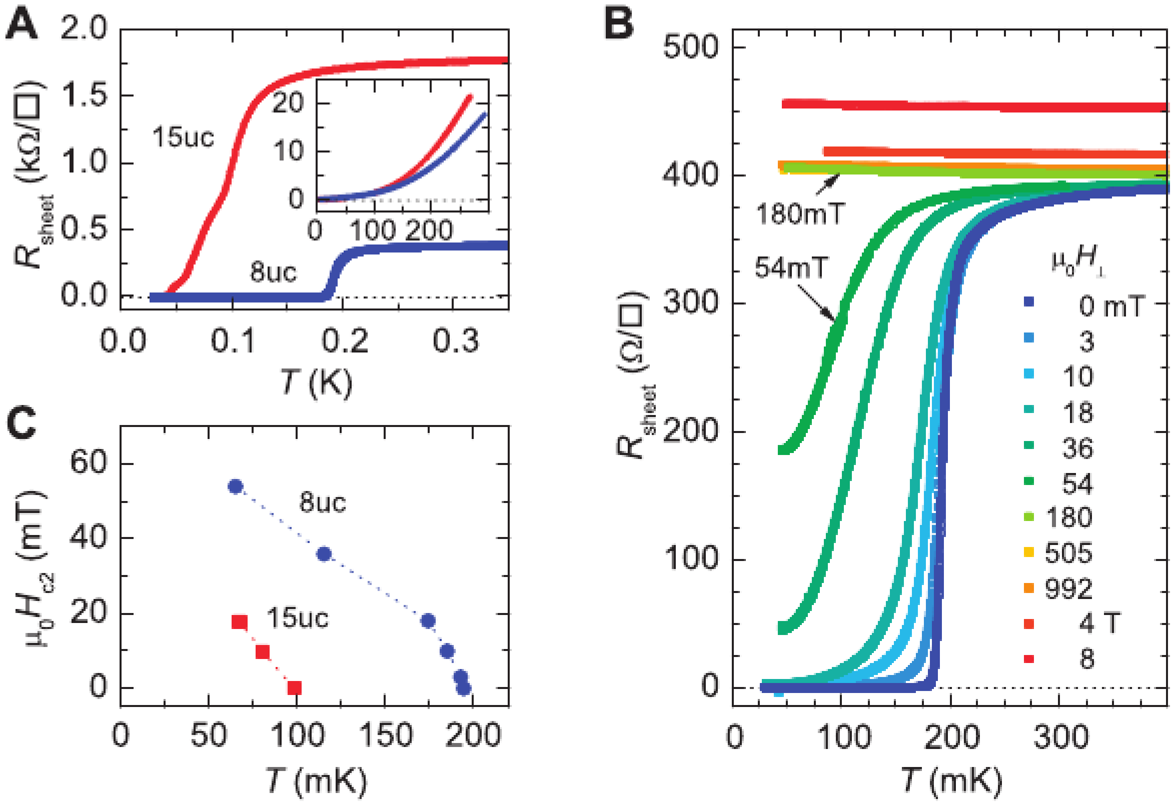

Fig. 2. Transport measurements on $LaAlO_3/SrTiO_3$ heterostructures. (**A**) Dependence of the sheet resistance on T of the 8-uc and 15-uc samples (measured with a 100-nA bias current). (Inset) Sheet resistance versus temperature measured between 4 K and 300 K. (**B**) Sheet resistance of the 8-uc sample plotted as a function of T for magnetic fields applied perpendicular to the interface. (**C**) Temperature dependence of the upper critical field H_{c2} of the two samples.

Superconductivity at different V_G

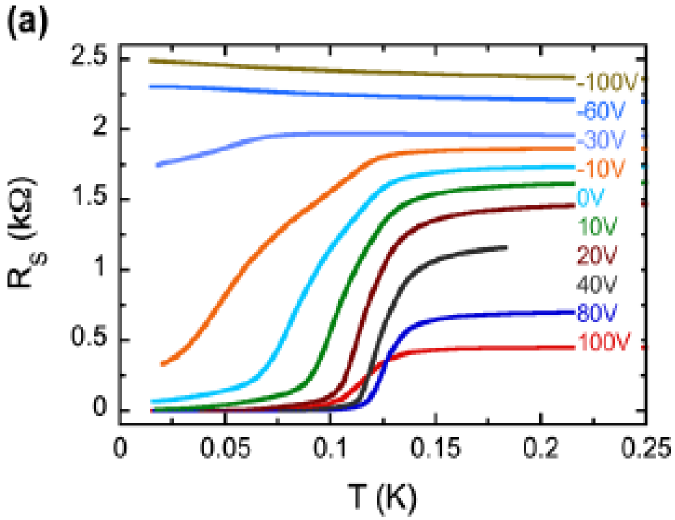

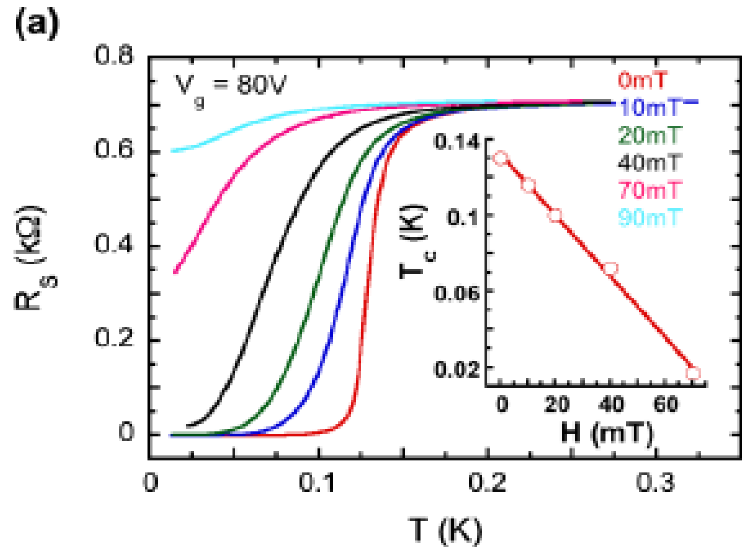

FIG. 2 (color online). (a) Superconducting transition for $V_g = 80$ V, at a few different magnetic fields. Inset: T_c vs H obtained

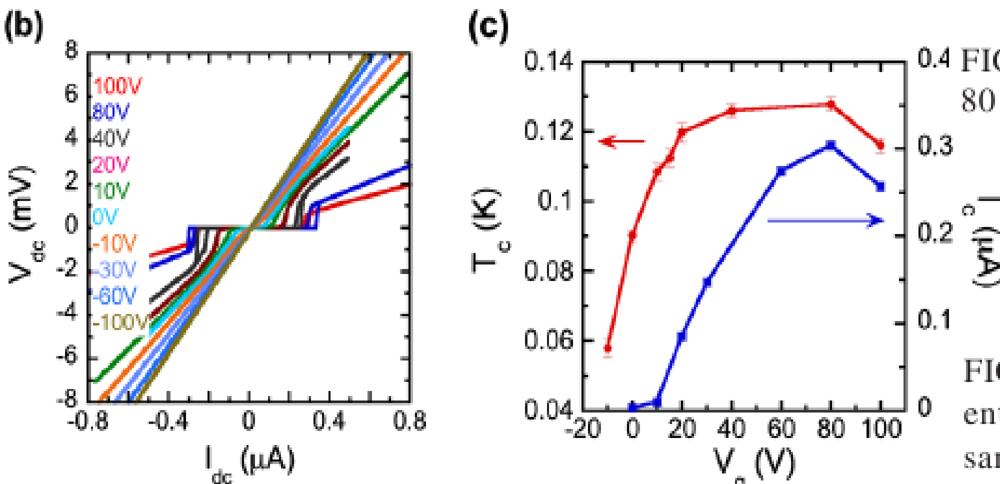

FIG. 1 (color online). (a) Superconducting transition at different gate voltages V_g. (b) Current-voltage characteristics of the sample at 15 mK. (c) Transition temperature T_c (defined as the midpoint of the resistive transition) and critical current (defined as the current at which the sample switches to the resistive state on ramping the current up from zero) as a function of V_g. Both measures indicate that the maximal superconducting properties are obtained for $V_g \simeq 80$ V. Error bars indicate the difference in T_c measured between cooling and warming traces.

Dikin, et al. PRL **107,** 056802 (2011)

Field (gate voltage)-control of transport

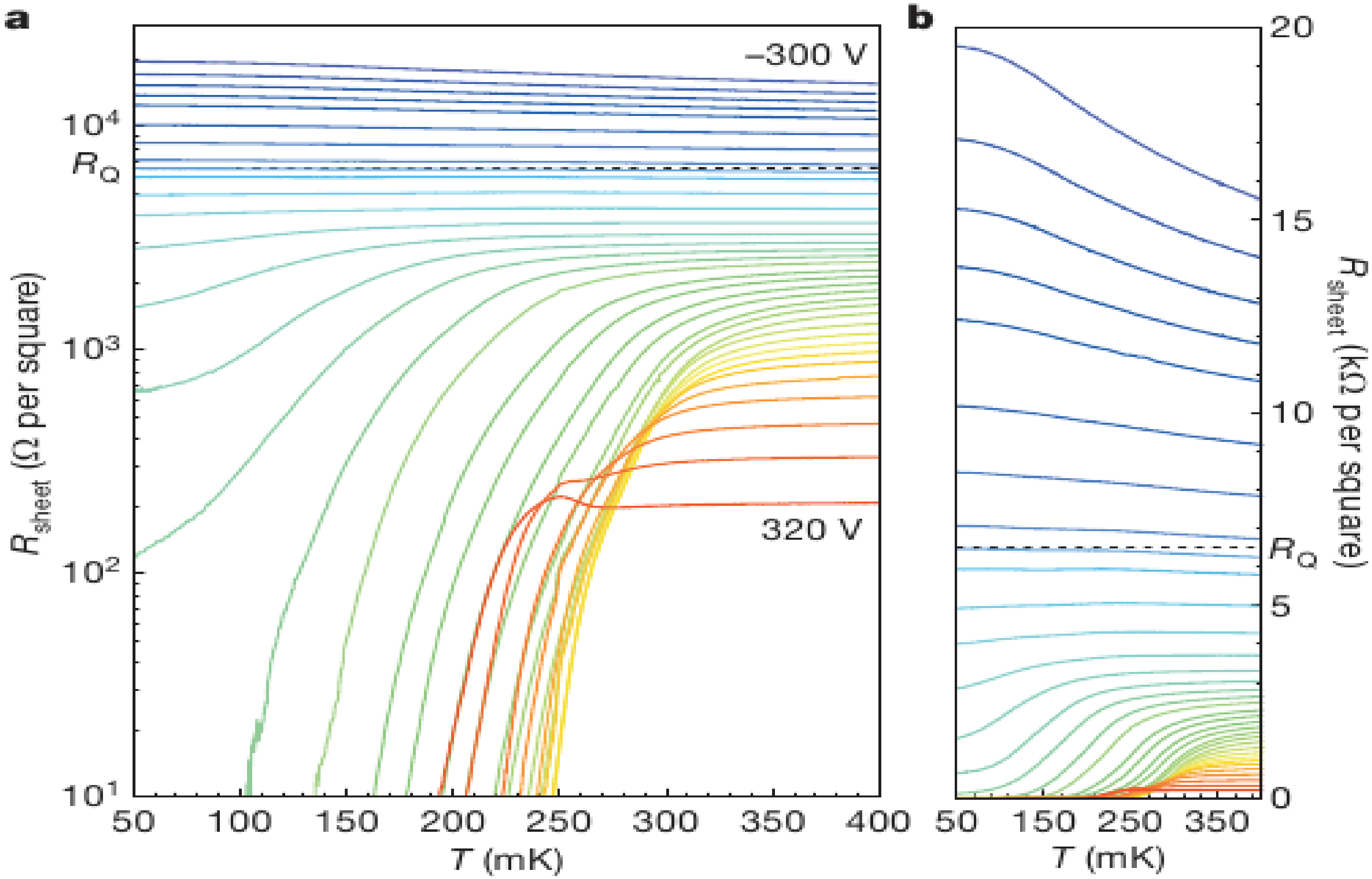

Figure 2 | Field-effect modulation of the transport properties. **a**, Measured sheet resistance as a function of temperature, plotted on a semi-logarithmic scale, for gate voltages varying in 10-V steps between −300 V and −260 V, 20-V steps between −260 V and 320 V, and for −190 V. The dashed line indicates the quantum of resistance R_Q. **b**, The same data plotted on a linear resistance scale.

Caviglia, Nature 456, 624 (2008),
Behnia, PRL 112 (2014)

Features of SC

- LO phonon mediated
- Low carrier density ($10^{-13}/cm^2$)
- Tc shows BKT behaviour
- $2\Delta_0/(k_B\ T_g) \sim 3.4$, Tg is the so-called gap-closing temperature
- It coexists with inhomogeneous ferromagnetic puddles of large moments ($\sim 0.4\mu_B$ per interface unit cell)
- Enhancement of superconductivity by magnetic field
- The magnetic-field-assisted transient superconductivity leading to a possible "hidden order."

Superconducting phase diagram

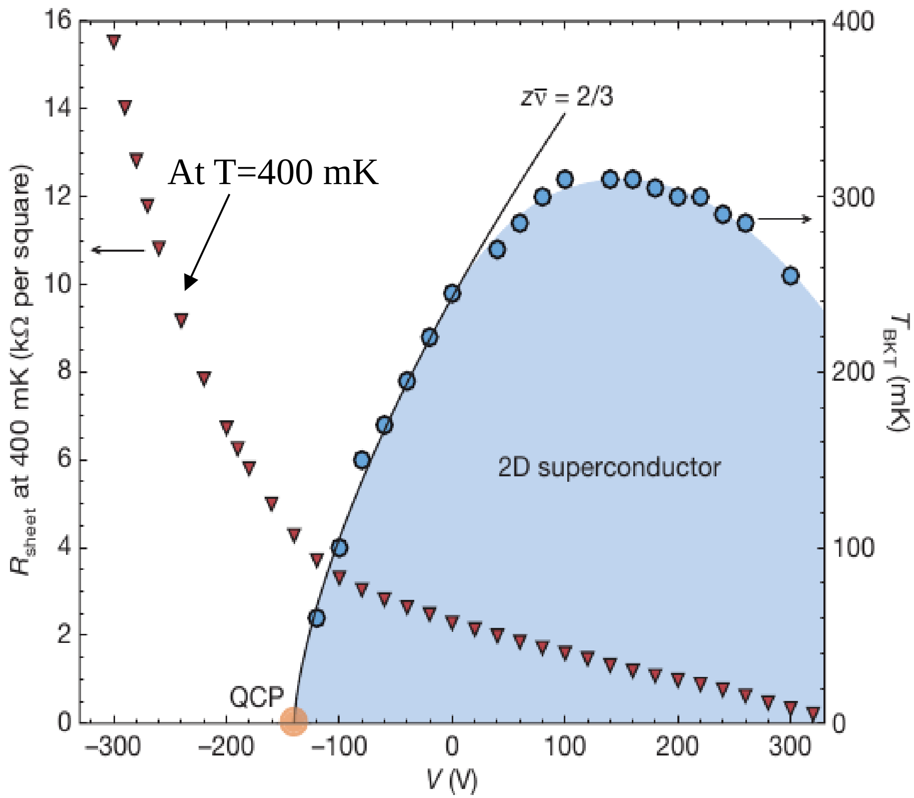

Figure 3 | Electronic phase diagram of the $LaAlO_3/SrTiO_3$ interface. Critical temperature T_{BKT} (right axis, blue dots) is plotted against gate voltage, revealing the superconducting region of the phase diagram. The solid line describes the approach to the quantum critical point (QCP) using the scaling relation $T_{BKT} \propto (V - V_c)^{z\bar{\nu}}$, with $z\bar{\nu} = 2/3$. Also plotted is normal-state sheet resistance, measured at 400 mK (left axis, red triangles) as a function of gate voltage.

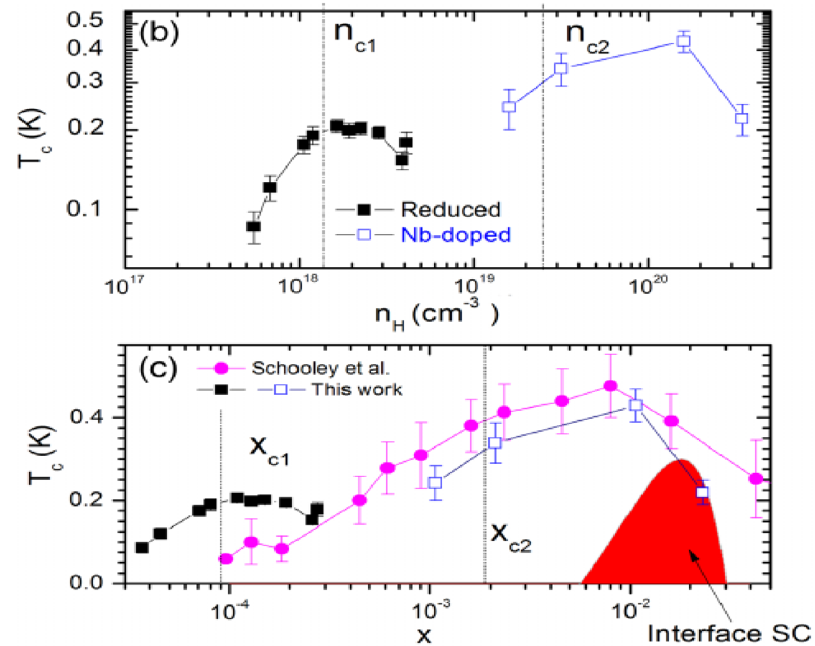

FIG. 1 (color online). (a) Detected frequencies of quantum oscillations as a function of carrier concentration. At two critical doping levels, designated as n_{c1} and n_{c2}, a new frequency emerges. At each critical doping a new band starts to be occupied. (b) Superconducting resistive transition temperature (on a logarithmic axis) as a function of carrier concentration. Solid squares represent reduced samples ($SrTiO_{3-\delta}$) and open squares Nb-doped samples ($SrTi_{1-x}Nb_xO_3$ with $x = 0.02$, 0.01, 0.002, and 0.001). Error bars represent the width of transition. (c) T_c (on a linear axis) as a function of carrier per formula unit. Our data are compared with those reported by Schooley and co-workers [2]. The red shaded region shows the rough contours of superconductivity in the $SrTiO_3/LaAlO_3$ interface [4,17,18].

Caviglia, Nature 456, 624 (2008), Behnia, PRL 112 (2014)

BKT signature and QCP

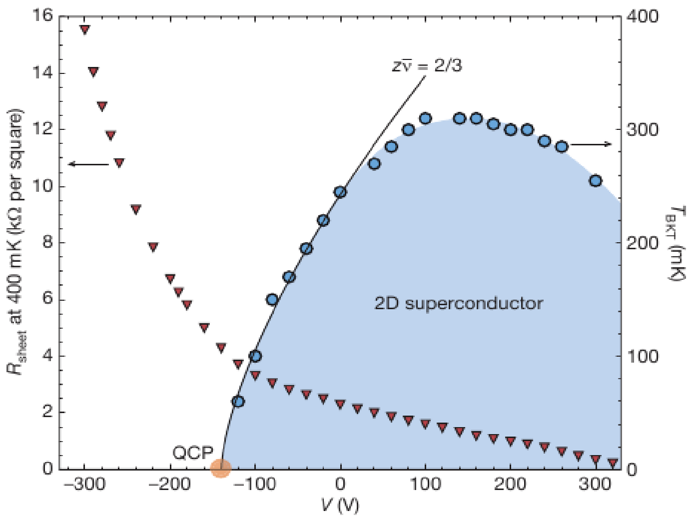

$$R \propto \exp\left(-\frac{b_R}{(T-T_{\mathrm{BKT}})^{1/2}}\right)$$

quantum critical region is characterized by a spatial and a temporal correlation length that diverge respectively as $\xi \propto (\delta n_{2D})^{-\bar{\nu}}$ and $\xi_\tau \propto (\delta n_{2D})^{-\nu_\tau}$. The quantum dynamic critical exponent is defined through the ratio $z = \nu_\tau/\bar{\nu}$. According to the scaling theory of quantum critical phenomena[20–22] the phase transition line $T_{\mathrm{BKT}}(\delta V)$ presented in Fig. 3 is expected to scale, near the quantum critical point, as

$$T_{\mathrm{BKT}} \propto (\delta n_{2D})^{z\bar{\nu}} \propto (\delta V)^{z\bar{\nu}} \qquad z\bar{\nu} = 2/3; \quad (3)$$

Gap and superconducting phase diagram

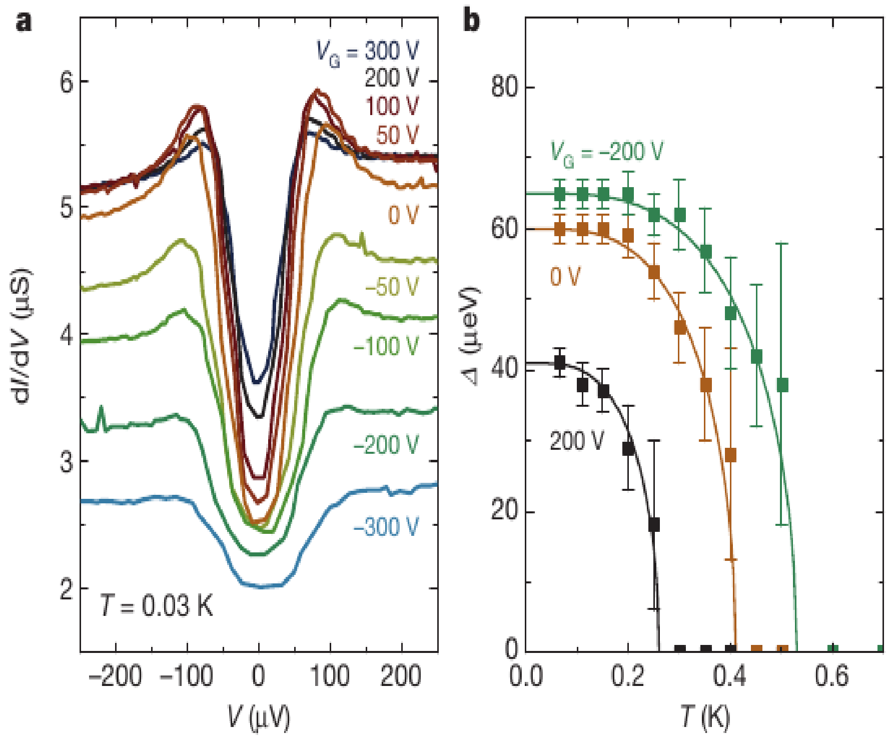

Figure 3 | Dependence of the tunnel spectra on gate voltage. **a**, Tunnel spectra as a function of the back-gate voltage, V_G (positive voltage corresponds to carrier accumulation). The device area is 0.5 mm^2. **b**, Temperature dependence of Δ for different values of V_G. The solid lines are the predictions of the BCS model. Error bars define the 90% confidence interval.

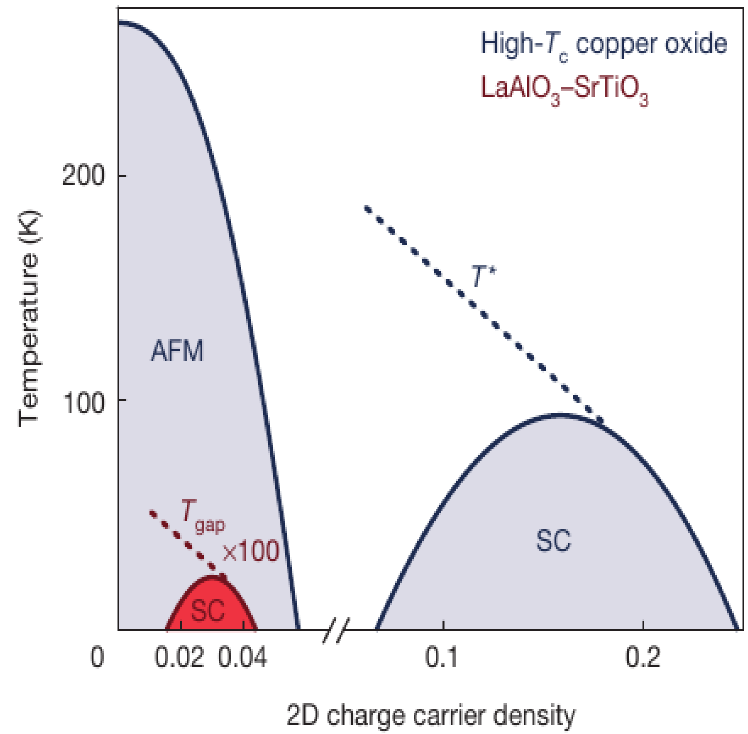

Figure 5 | Comparison between phase diagrams for $LaAlO_3$–$SrTiO_3$ and copper oxide superconductors. Illustration of the doping-versus-temperature phase diagram of the n-doped $LaAlO_3$–$SrTiO_3$ interface 2DEL and the p-doped high-T_c copper oxide superconductors. The charge carrier density is given in units of charge carriers per 2D unit cell. AFM, antiferromagnetic; SC, superconducting.

24 OCTOBER 2013 | VOL 502 | NATURE | 529

Richter, Nature Lett. 502 (2013)

Direct imaging of the coexistence of ferromagnetism and superconductivity at the $LaAlO_3/SrTiO_3$ interface

Julie A. Bert[1], Beena Kalisky[1], Christopher Bell[1], Minu Kim[1,2], Yasuyuki Hikita[1], Harold Y. Hwang[1,2] and Kathryn A. Moler[1]*

Nature Physics **7**, 767 (2011)

Ferromagnetic landscape

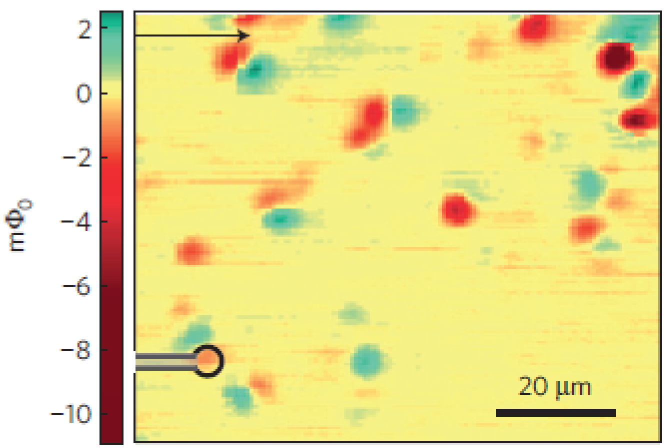

Scanning SQUID Magnetometry image
(Ferromagnetic order)

Superconducting landscape

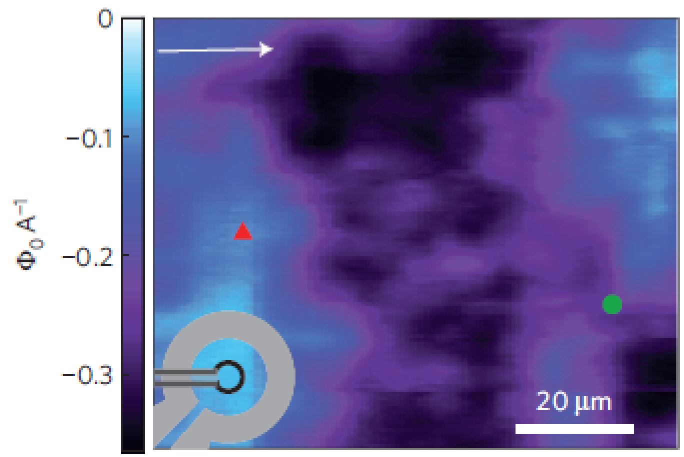

Scanning SQUID Susceptometry image
(Superfluid density)

Bert, et al.

NATURE PHYSICS DOI: 10.1038/NPHYS2079 Nature Physics 7, 767 (2011) LETTERS

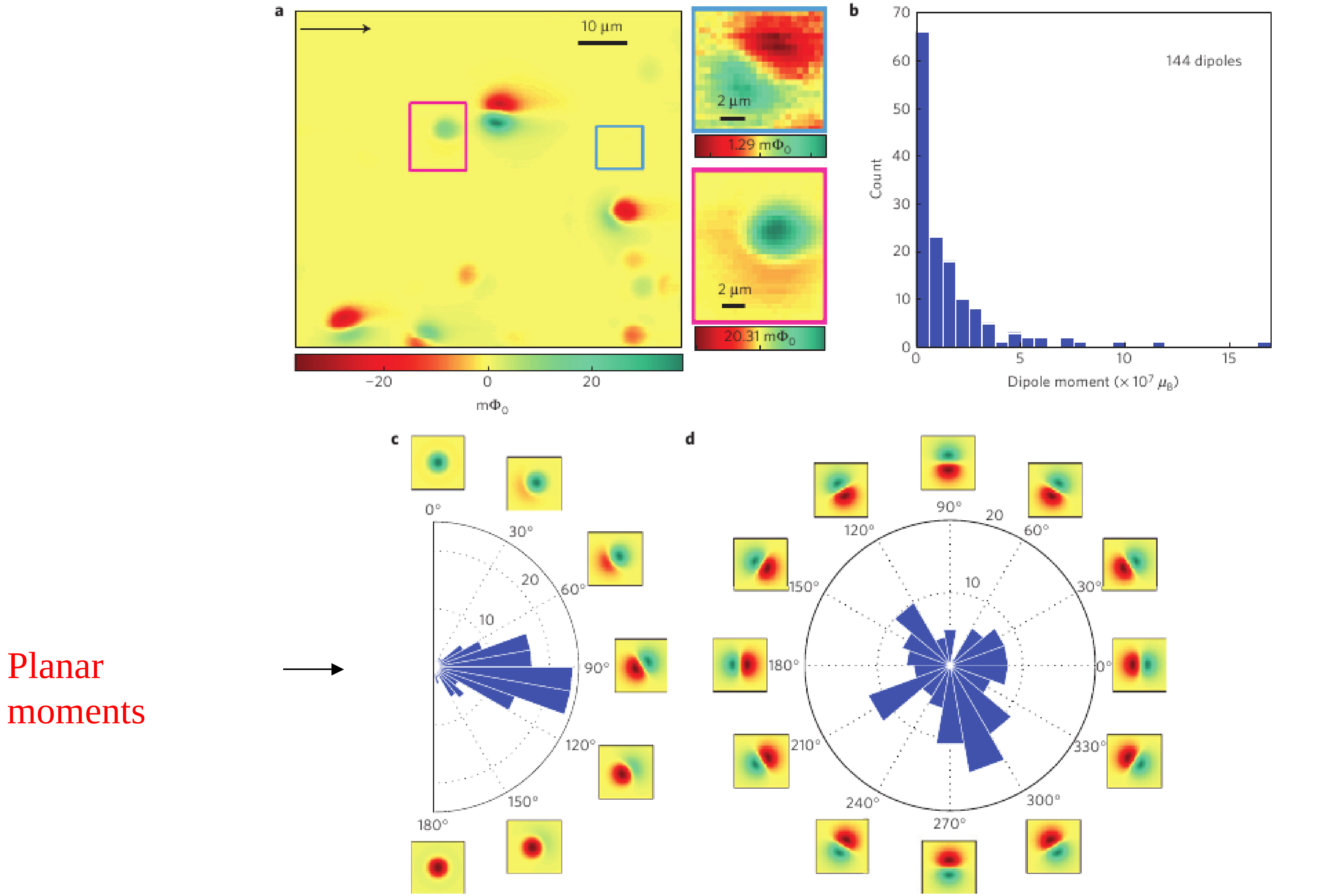

Figure 2 | Analysis of the dipole distribution. a, Magnetometry scan showing ferromagnetic dipoles. The arrow shows the scan fast axis and the SQUID orientation. Insets: Individual dipoles from the areas indicated in the larger image. **b–d**, Histograms of the moment and orientation of 144 dipoles taken from six large-area scans similar to the one shown in **a**. **b**, The magnetic moment of each dipole in Bohr magnetons, μ_B. **c**, The inclination angle from the normal to the sample surface (an inclination angle of 90° means the dipole lies in the plane of the interface). **d**, The azimuthal angle with respect to the scan's x axis.

XMCD: magnetism is in-plane & in Ti^{3+}

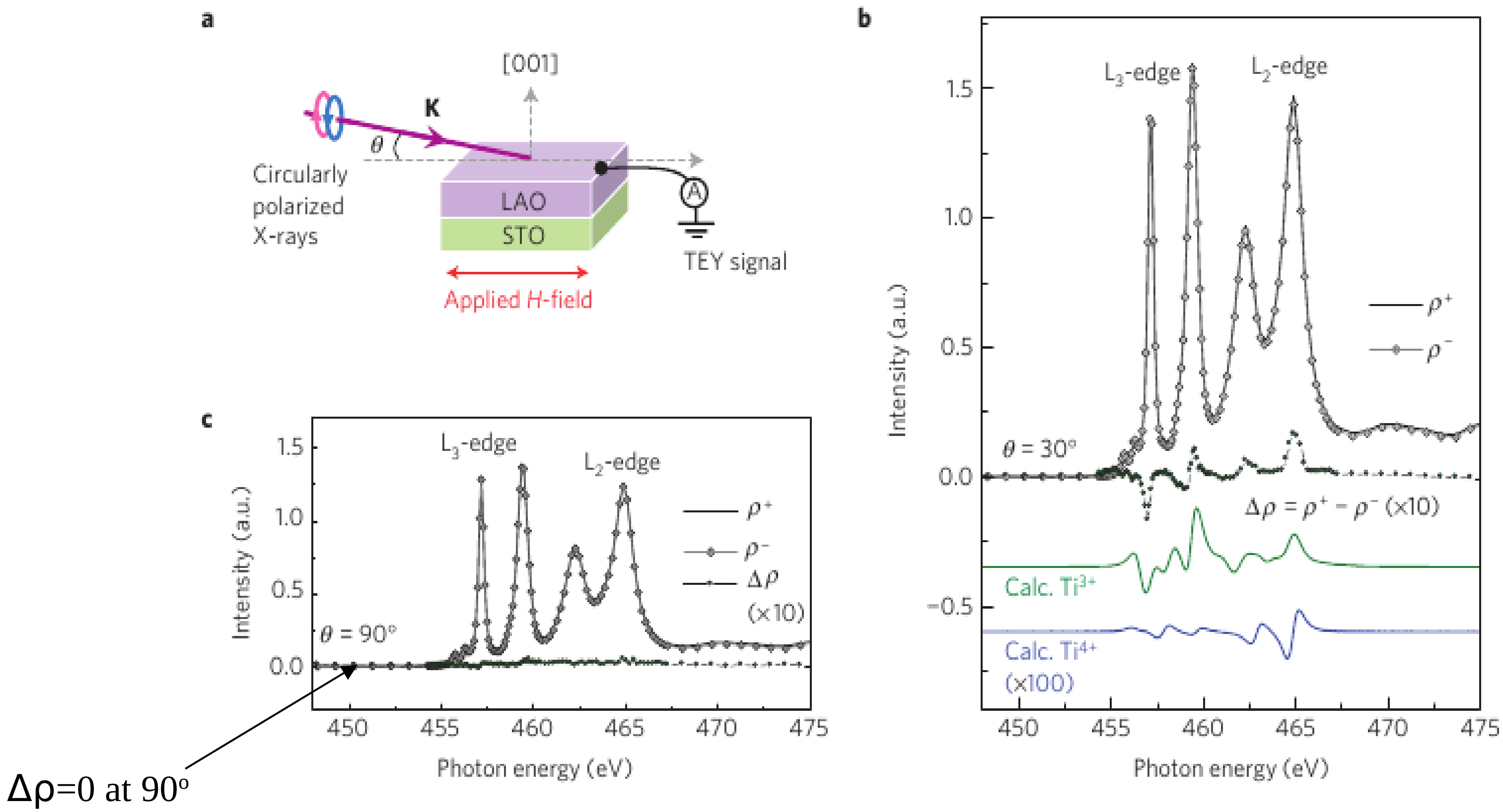

Figure 1 | X-ray magnetic circular dichroism (XMCD) on a $LaAlO_3/SrTiO_3$ heterostructure. a, Schematic picture of the experimental configurations for the XMCD measurement. **b**, XMCD observed for the in-plane geometry, showing ferromagnetic Ti at $T = 10$ K (the $\Delta\rho$ shown is the result of averaging 20 scans). The green and blue coloured lines are the Ti^{3+} and Ti^{4+} XMCD spectra obtained from multiplet calculations, respectively. The calculated Ti^{4+} spectrum has been multiplied by 100. **c**, XMCD in the out-of-plane geometry ($\theta = 90°$). All samples were zero-field cooled and measured in a constant applied field of ± 0.2 T.

Lee, et al. Nat. Mater. **12**, 703 (2013)

Angular dependence of M: nearly planar

NATURE PHYSICS DOI: 10.1038/NPHYS2080 **LETTERS**

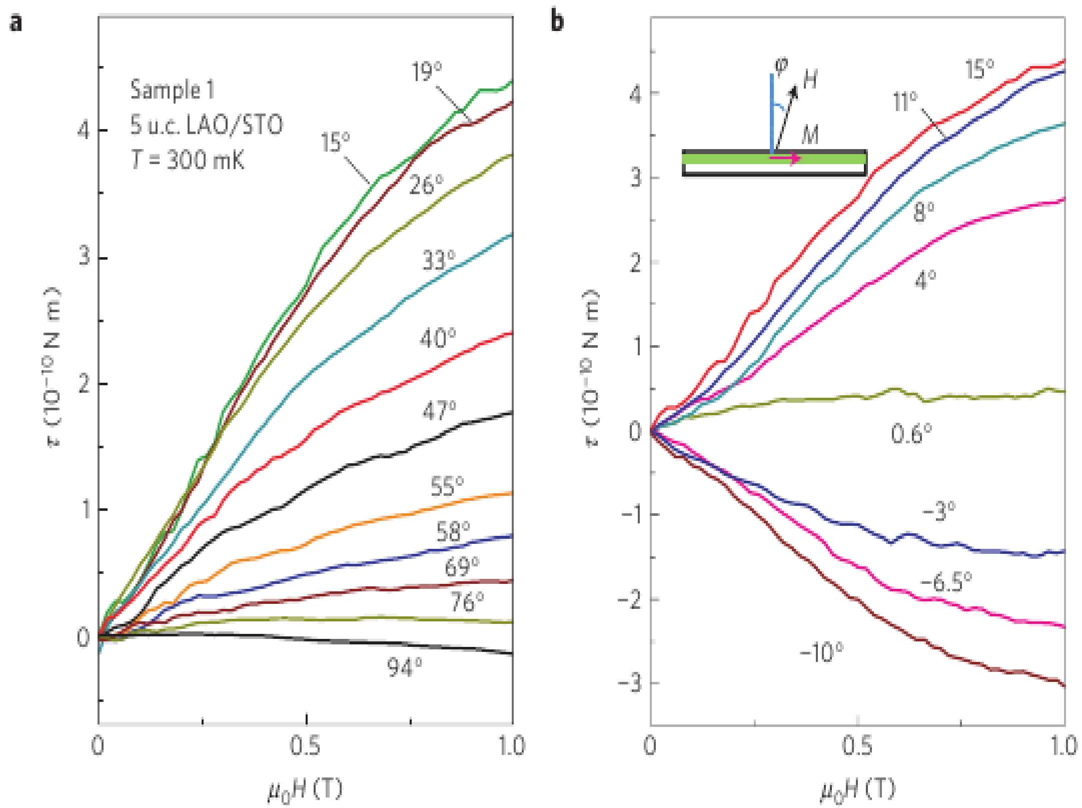

Figure 4 | Angular dependence of the interface torque indicating an in-plane saturation magnetic moment. a,b, At $T = 300$ mK, the magnetic torque of the 5 u.c. LAO/STO sample is measured at various tilt angles φ between 15° and 94° (**a**) and between −10° and 15° (**b**). The inset of **b** shows the geometry of the field H and magnetization M, and the definition of the tilt angle φ.

Bert et al. Nat. Phys. *op cit.*

Torque T vanishes for field-angle (ϕ)~ 90 deg. T=M x B=MB sin (90-ϕ) => M is planar

Contact & non contact SQUID measurement

dx.doi.org/10.1021/nl301451e | Nano Lett. 2012, 12, 4055–4059

Surface texture of FM: Phase seaparation

Nano Letters Letter

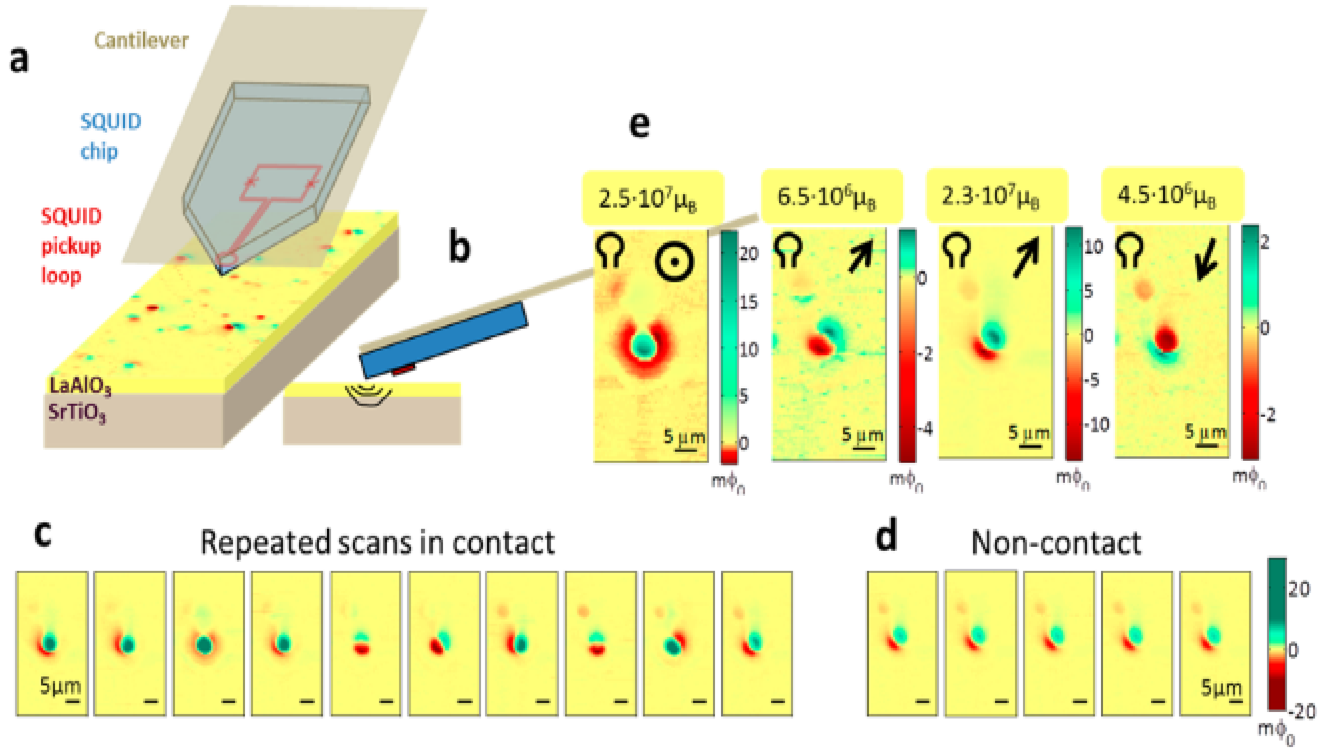

Figure 1. Ferromagnetic patches change with local contact applied by the SQUID's tip. (a) Cartoon of the measurement configuration. (b) The SQUID chip is mounted on a cantilever and can be pushed onto the sample surface during a scan. The sensing area is ~7 μm away and 1 μm above the contact point. (c) Ten successive scans (4 K; 15 uc sample) of a 25 μm × 45 μm area reveal changes in a ferromagnetic patch. The tip is out of contact between scans and brought into contact at the start of the next scan. (d) Five successive scans obtained directly after the scans in (c) but without contact with the sample surface (1 μm higher than in (c)) show no change in the patch. (e) Four scans in contact plotted on the full flux scale show the change in orientation and moment (noted above each scan). The small arrow on each scan marks the orientation angle of the dipole, which is extracted directly from the data using the magnitude and orientation of the dipole. A weaker ferromagnetic patch in the scanned region follows the same behavior, although the orientation of the two patches in the scans do not appear to be related.

Kalisky, et al. Nano Lett. **12**, 4055 (2012)

Phase separation in LAO/STO interface: hysteresis

Ariando, Dhar, et al. Nat. Comm. (2011)

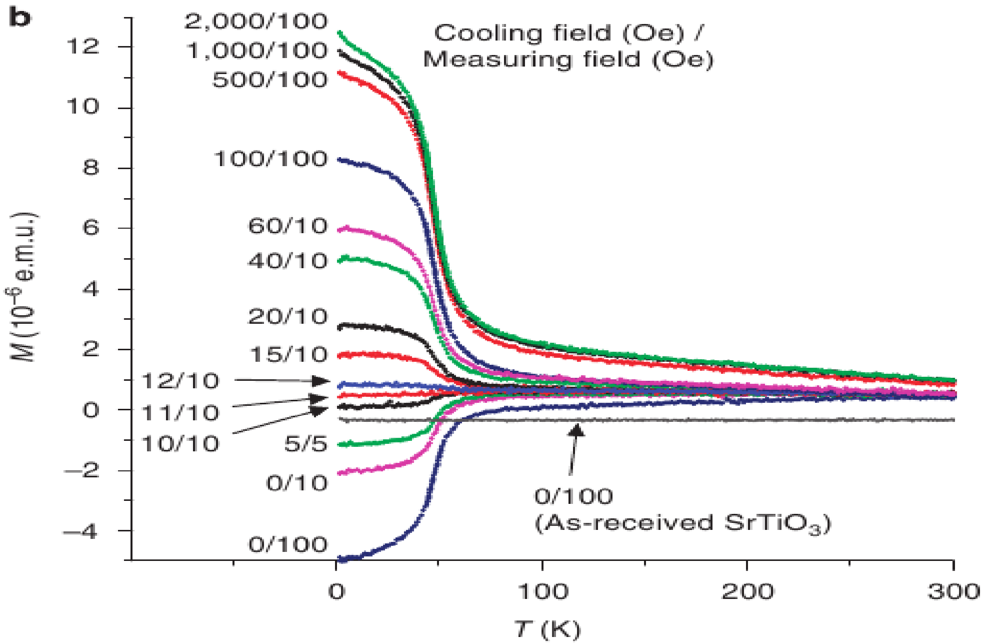

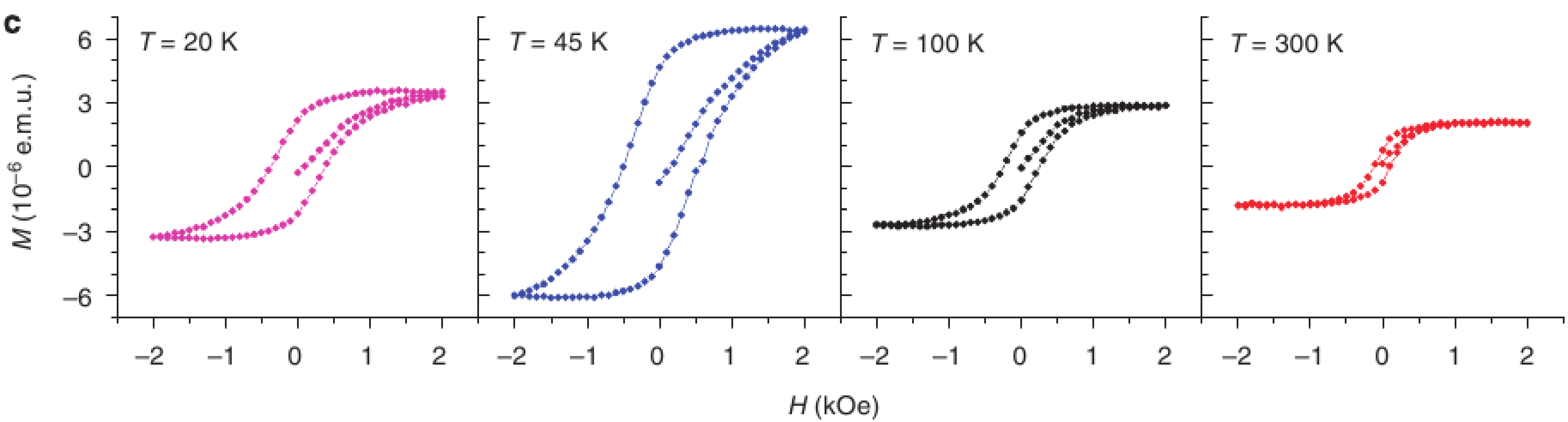

branch when the hysteresis loops are collected after FC (not shown here for clarity). (**b**) Magnetization as a function of temperature under various cooling temperatures and magnetic fields for the ten unit cells of $LaAlO_3/SrTiO_3$ samples prepared at $P_{O2} = 1\times10^{-2}$ mbar. (**c**) The temperature-dependent ferromagnetic loops in **a** after diamagnetic and paramagnetic subtraction.

Issues at a glance

- ❖ **Formation of quasi-2DEG at the interface**
- ❖ **Low temperature (< 300mK) superconductivity**
- ❖ **Ferromagnetic order (upto 200 K) from two non-magnetic oxides**
- ❖ **Coexistence of superconductivity and ferromagnetism**
- ❖ **Electric field induced superconductor to insulator transition**
- ❖ **Critical LAO film thickness for the appearance of 2DEG**
- ❖ **Vortices and possible excitations: Majorana bound states?**
- ❖ **Nature of SC (BKT?), helical magnetisation, ...**
- ❖ **"Hidden superconducting" state above nominal Tc**
- ❖ **Oxygen vacancies, vacancy ordering, disorder, more oxides?**
- ❖ **BKT transition from resistive noise.**
- ❖ **Signature of Lifshitz transition**
- ❖ **Sign change in magnetoresiatance**

Local electronic structure from DFT

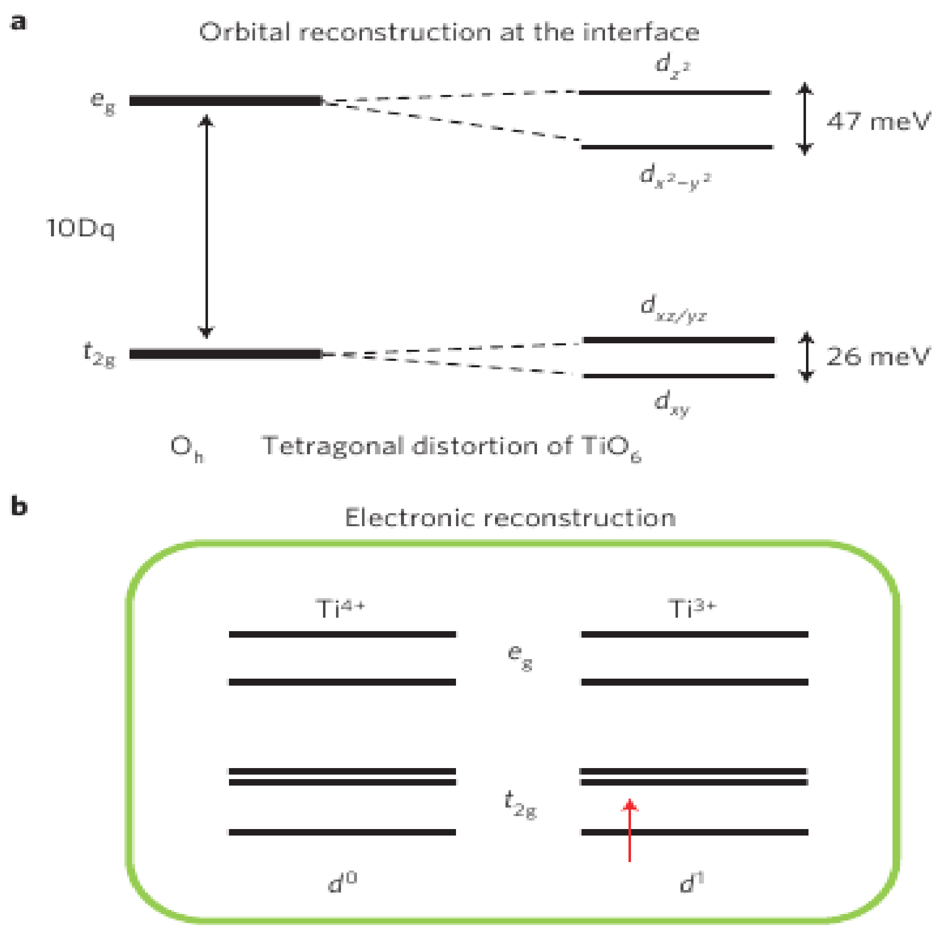

Figure 3 | Spectroscopic diagram of the LAO/STO interface. a, Schematic energy diagrams of the crystal field splitting and 3*d* orbital degeneracy, showing the orbital reconstruction at the interface and local bonding change. O_h denotes the octahedral environment. **b**, The mixed valence Ti^{3+} and Ti^{4+} states at the interface.

Lee, et al. Nat. Mater. **12**, 703 (2013)

Band Structure:

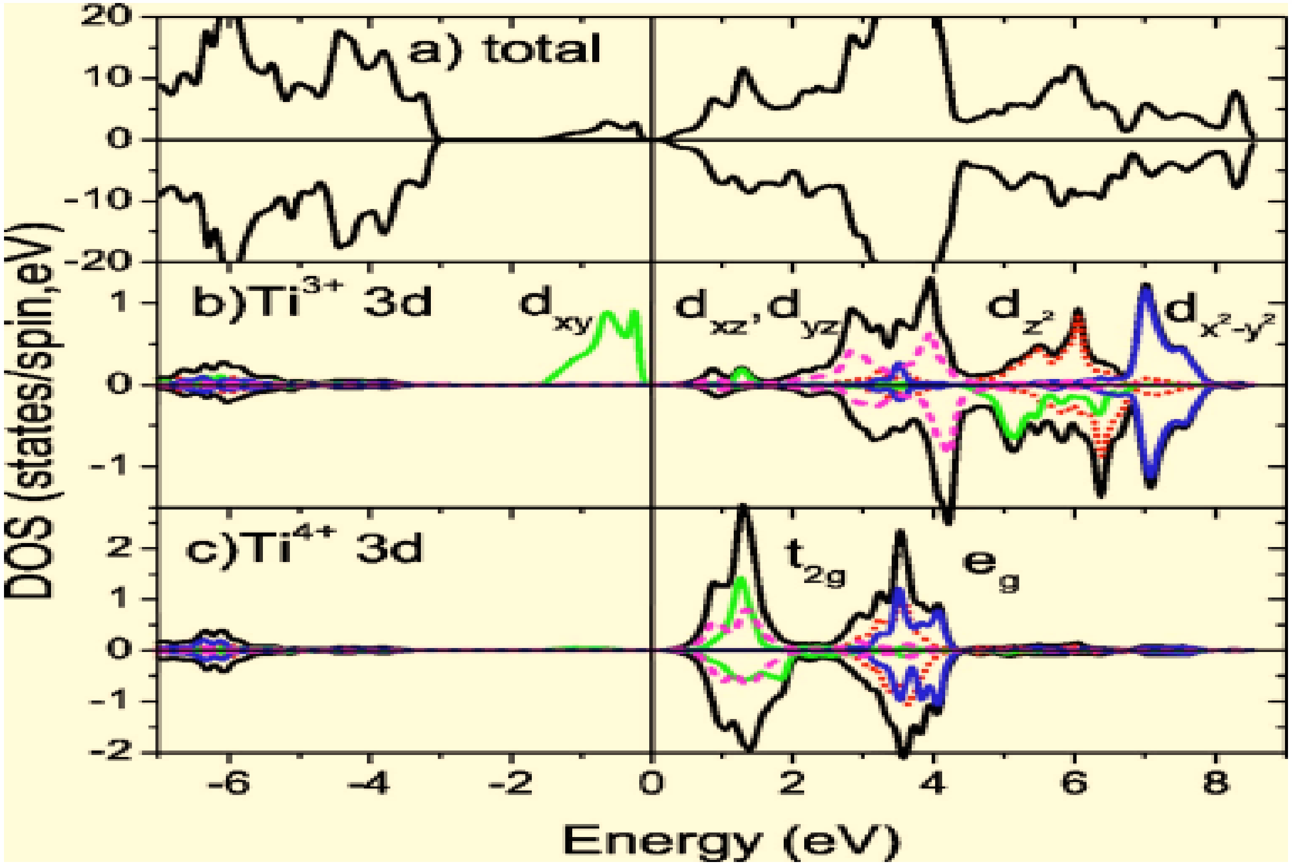

FIG. 10. (Color online) Density of states of the n-type interface: (a) total; (b) d states of magnetic Ti^{3+} showing the split-off majority d_{xy} band, with the corresponding minority states lying at +5 eV; the other 3d states are not strongly polarized; (c) the nonmagnetic Ti^{4+} ion, showing the conventional (although not perfect) $t_{2g}-e_g$ crystal field splitting. d_{xy} orbitals are marked by a green (light gray) line, d_{xz} and d_{yz} states by a magenta dashed line, states with d_{z^2} and $d_{x^2-y^2}$ character by a red dotted and blue (dark gray) solid lines, respectively.

Pentcheva & Pickett, PRB 74, 035115 (2006)

Band Picture: Formation of Local Moments at the Interface

- Electrons at the interface occupies the three t_{2g} bands of Titanium

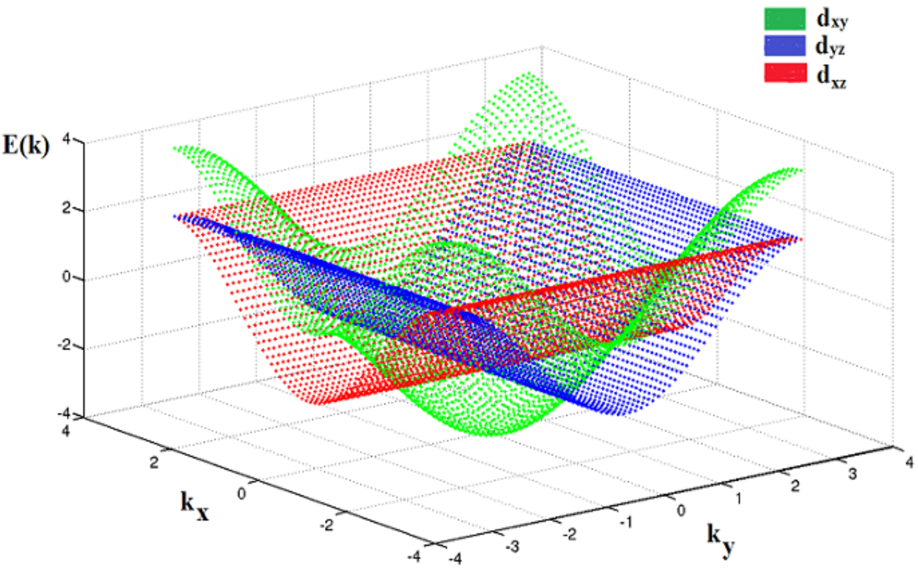

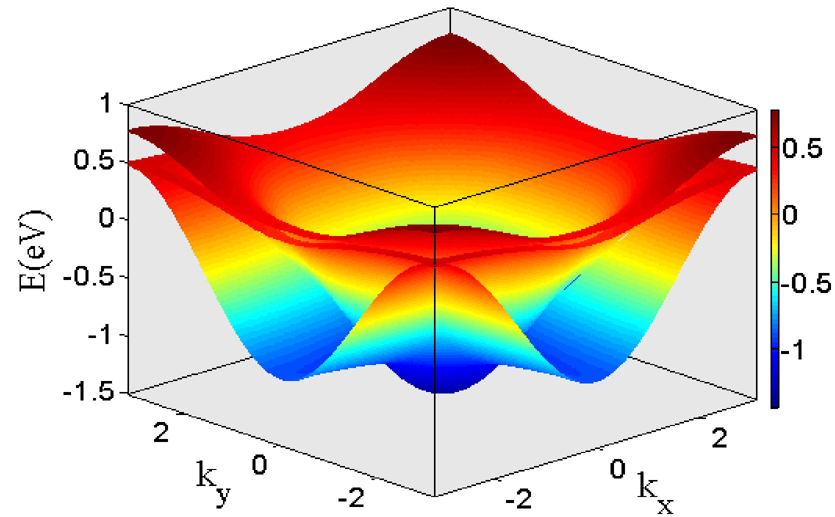

- Electrons are in d_{xy} band, form localized moments, other two have ~ 1D dispersion

- The exchange between the local moments and the itinerant electrons leads to ferromagnetic order

Model Hamiltonian: single (d_{xy}) band theory

$$\mathrm{H}_{tot} = \mathrm{H}_0 + \mathrm{H}_{ex} + \mathrm{H}_{so} + \mathrm{H}_{sc}$$

$$\mathrm{H}_0 = \sum_{k,\sigma} \varepsilon_k c^{\dagger}_{k\sigma} c_{k\sigma}$$ → Dispersion of electrons

$$\mathrm{H}_{ex} = -\sum_{k,\sigma,\sigma'} (\mathrm{h} \cdot \sigma)_{\sigma\sigma'} c^{\dagger}_{k\sigma} c_{k\sigma'}$$ → Zeeman field due to FM exchange

$$\mathrm{H}_{so} = \alpha \sum_{k,\sigma,\sigma'} (\mathrm{g}_k \cdot \sigma)_{\sigma\sigma'} c^{\dagger}_{k\sigma} c_{k\sigma'}$$ → Rashba spin-orbit coupling

$$\mathcal{H}'_{\mathrm{RSO}} = (\gamma/\hbar)(\vec{\sigma} \times \vec{p}) \cdot \hat{z},$$

$$\mathrm{H}_{sc} = \sum_{k} (\Delta c^{\dagger}_{k\uparrow} c^{\dagger}_{-k\downarrow} + h.c.)$$ → BCS pairing term

where

$$\varepsilon_k = -2t(\cos k_x + \cos k_y) - \mu$$

$$h = (\mathrm{h}_x, \mathrm{h}_y, 0)$$

$$\sigma = (\sigma_x, \sigma_y, \sigma_z)$$ Pauli Matrices

$$\mathrm{g}_k = (\sin k_y, -\sin k_x, 0)$$

$$\Delta = -U < c_{k\uparrow} c_{-k\downarrow} >$$

Electron pairing at finite momentum

Modification in bands:

$$\begin{pmatrix} c_{k\uparrow} \\ c_{k\downarrow} \end{pmatrix} = \frac{1}{\sqrt{2}} \begin{pmatrix} 1 & 1 \\ e^{i\phi} & -e^{i\varphi} \end{pmatrix} \begin{pmatrix} \gamma_{k+} \\ \gamma_{k-} \end{pmatrix} \qquad \text{where} \quad \phi = \tan^{-1}\left(\frac{-\sin k_x - h_y}{\sin k_y - h_x} \right)$$

New energy bands: $\varepsilon_{\pm}(\vec{k}) = \varepsilon_k \pm |\alpha \vec{g}_k - \vec{h}\,|$

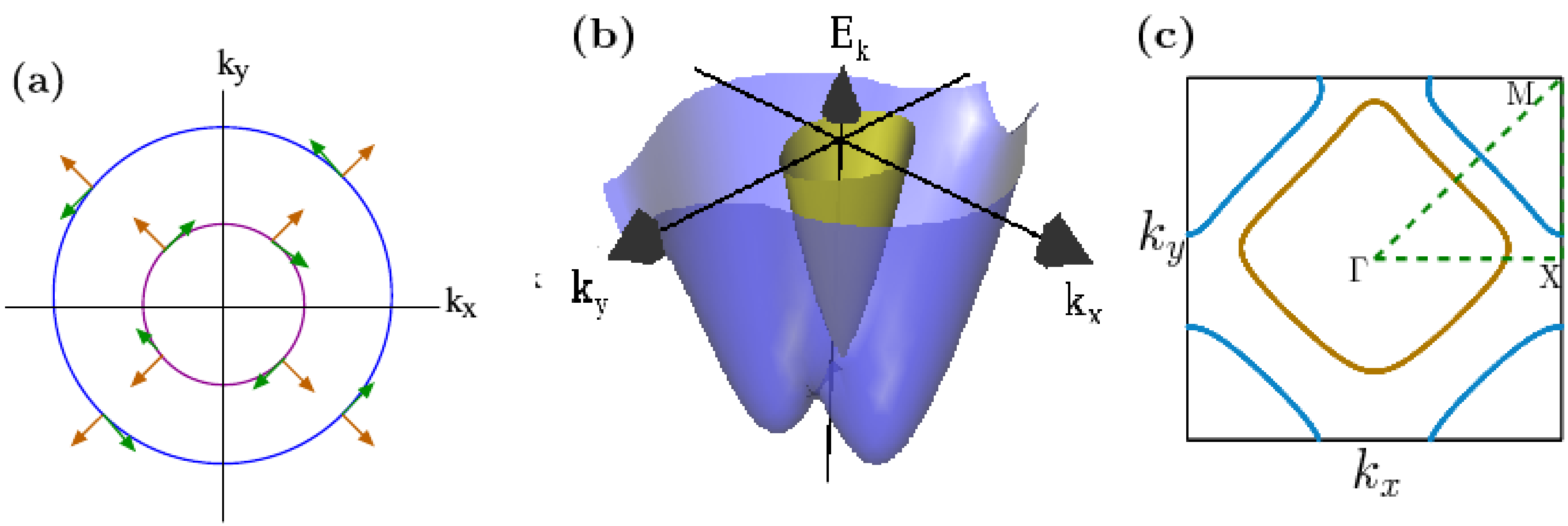

Figure 1. (a) Two-sheeted Fermi surface of the Rashba-split bands showing the helical alignment of the spins (green) and corresponding momentum (orange). (b) The resultant bands and (c) the asymmetric Fermi surface created by Rashba spin–orbit interaction with the Zeeman field along the $\hat{x}$ direction.

Electron pairing at finite momentum

Modification in surface bands:

$$\begin{pmatrix} c_{k\uparrow} \\ c_{k\downarrow} \end{pmatrix} = \frac{1}{\sqrt{2}} \begin{pmatrix} 1 & 1 \\ e^{i\phi} & -e^{i\varphi} \end{pmatrix} \begin{pmatrix} c_{k+} \\ c_{k-} \end{pmatrix} \qquad \text{where} \quad \phi = \tan^{-1}\left(\frac{-\sin k_x - h_y}{\sin k_y - h_x} \right)$$

New energy bands: $\varepsilon_{\pm}(k) = \varepsilon_k \pm |\alpha \vec{g}_k - \vec{h}|$

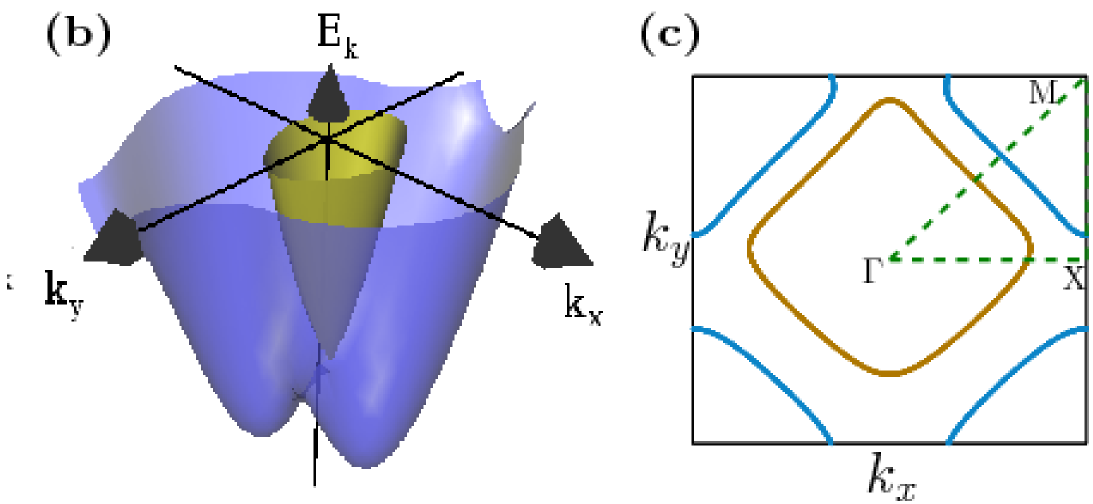

Pairing of electrons at a finite momentum and spin-mixing

Self-consistent Bogoliubov-de Gennes (BdG) analysis

Mean-field Hamiltonian:

$$\hat{H}_{BdG} = -t\sum_{<ij>,\sigma}(c^{\dagger}_{i\sigma}c_{j\sigma} + h.c.) - (\mu - V_d)\sum_{i,\sigma} c^{\dagger}_{i\sigma}c_{i\sigma} - H_x \sum_{i,\sigma,\sigma'}(\sigma_x)_{\sigma\sigma'}c^{\dagger}_{i\sigma}c_{i\sigma'}$$

$$-i\frac{\alpha}{2}\sum_{<ij>,\sigma,\sigma'} c^{\dagger}_{i\sigma}(\vec{\sigma}\times\vec{d}_{ij})^{\sigma\sigma'}_{z}c_{j\sigma'} + \sum_i \Delta(r_i)(c^{\dagger}_{i\uparrow}c^{\dagger}_{i\downarrow} + h.c.)$$

$$V_d = [-W, W]$$

Disorder

Bogoliubov transformation:

$$\hat{c}_{i\sigma}(r_i) = \sum_{i,\sigma'}\left[u_{n\sigma\sigma'}(r_i)\hat{\gamma}_{n\sigma'} + v^{*}_{n\sigma\sigma'}(r_i)\hat{\gamma}^{\dagger}_{n\sigma\sigma'}\right]$$

BdG equation:

$$\hat{H}_{BdG}\phi_n(r_i) = \varepsilon_n\phi_n(r_i)$$ with $$\phi_n(r_i) = [u_{n\uparrow}(r_i), u_{n\downarrow}(r_i), v_{n\uparrow}(r_i), v_{n\downarrow}(r_i)]^T$$

Self-consistent solutions:

$$\Delta(r_i) = -U < c_{i\downarrow}c_{i\uparrow} > = -U\sum_n\left[u_{n\uparrow}(r_i)v^{*}_{n\downarrow}(r_i)(1 - f(E_n)) + u_{n\downarrow}(r_i)v^{*}_{n\uparrow}(r_i)f(E_n)\right]$$

$$\mathrm{m}(r_i) = < c^{\dagger}_{i\uparrow}c_{i\downarrow} + c^{\dagger}_{i\downarrow}c_{i\uparrow} > = \sum_{n,\sigma}\left[u^{*}_{n\sigma}(r_i)u_{n\sigma'}(r_i)f(E_n) + v_{n\sigma}(r_i)v^{*}_{n\sigma'}(r_i)(1 - f(E_n))\right]$$

Role of disorder: Phase segregation of SC and FM

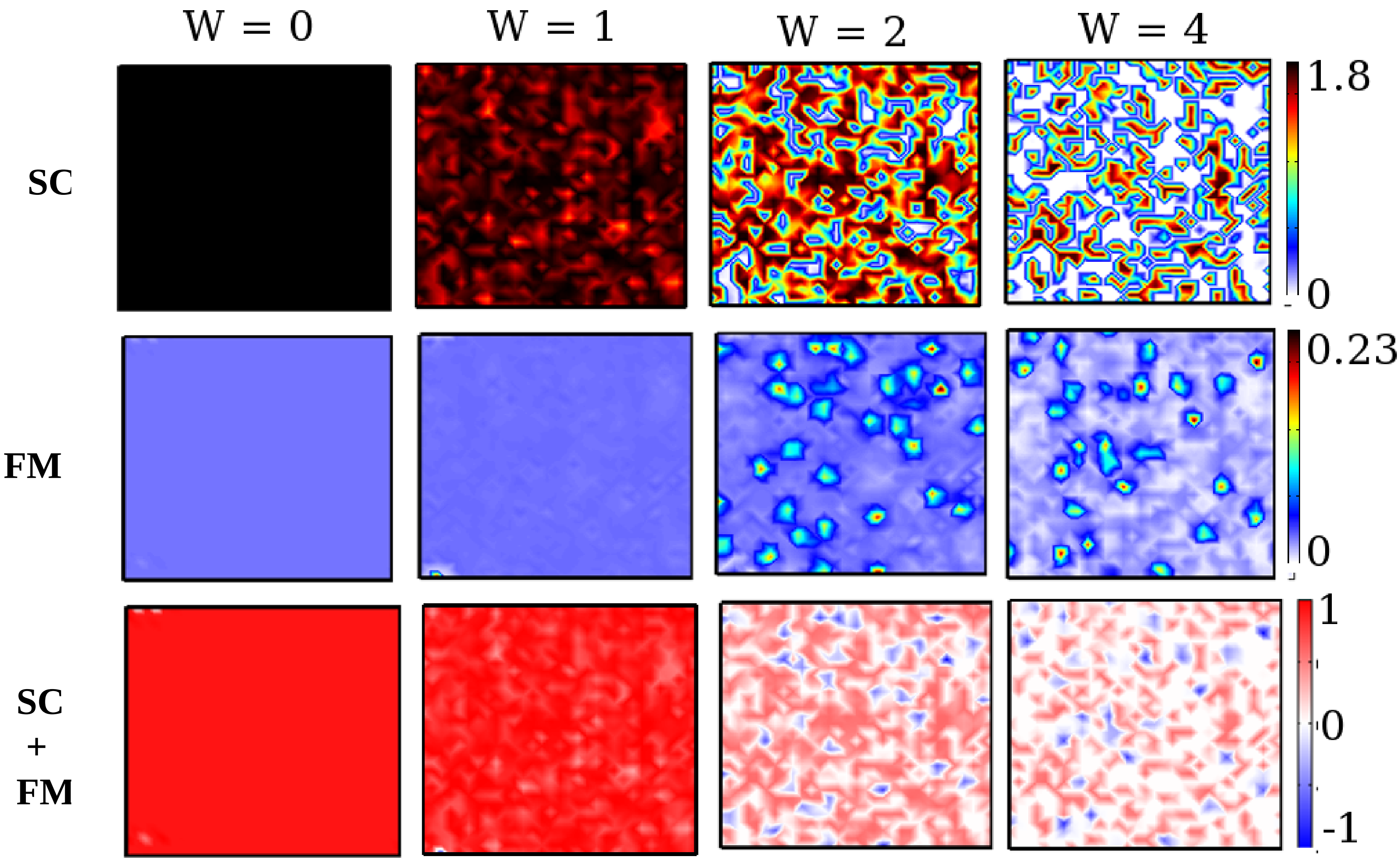

Figure 2. The spatial distribution of the local pairing amplitude $|\Delta(r_i)|$ (top row) and magnetization (middle row). The columns are for disorder strength $W = 0$, 1, 2 and 4 (from left to right). The lowest row shows the coexistence in combined plots of magnetization and local pairing amplitude; red and blue represent regions of superconductivity and ferromagnetism. The parameters used are $H_x = 0.5$ and $\alpha = 0.8$.

N. Mohanta and A. Taraphder JP

Distribution of gap and M

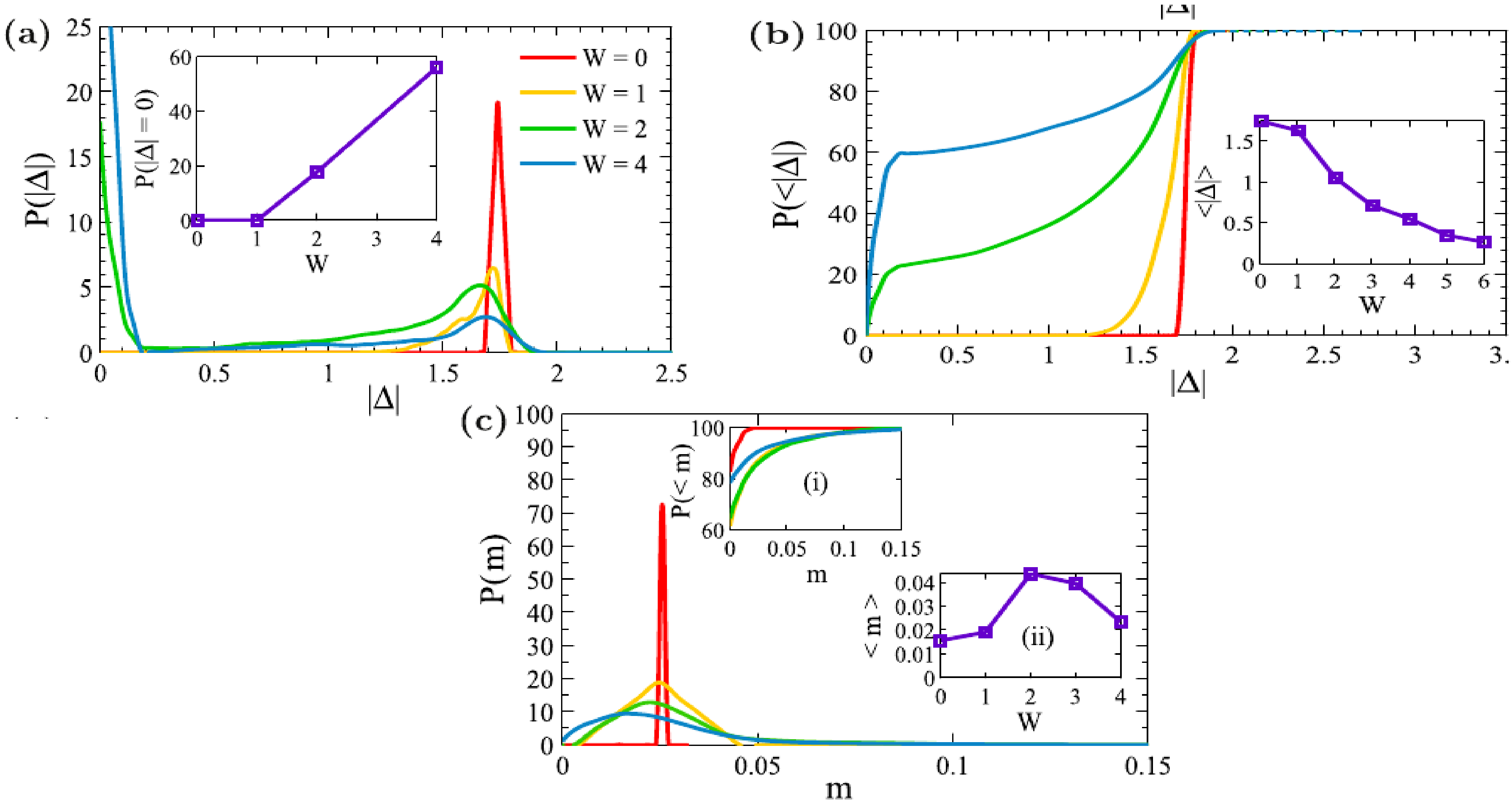

Figure 3. (a) Probability distribution of local pairing amplitudes. The inset shows the variation of the probability at zero gap with disorder strength. (b) The curves show the probability $P(<\Delta)$ that the gaps are less than a given Δ for different disorder strengths. The inset is $\langle|\Delta|\rangle$ as a function of disorder strength. (c) The probability distribution of local magnetization. Inset (i) is $P(<m)$ as a function of m and inset (ii) is the variation of average magnetization with disorder. The parameters used are $H_x = 0.5$, $\alpha = 0.8$ at $W = 4$.

Correlation fn. describes a disordered SC

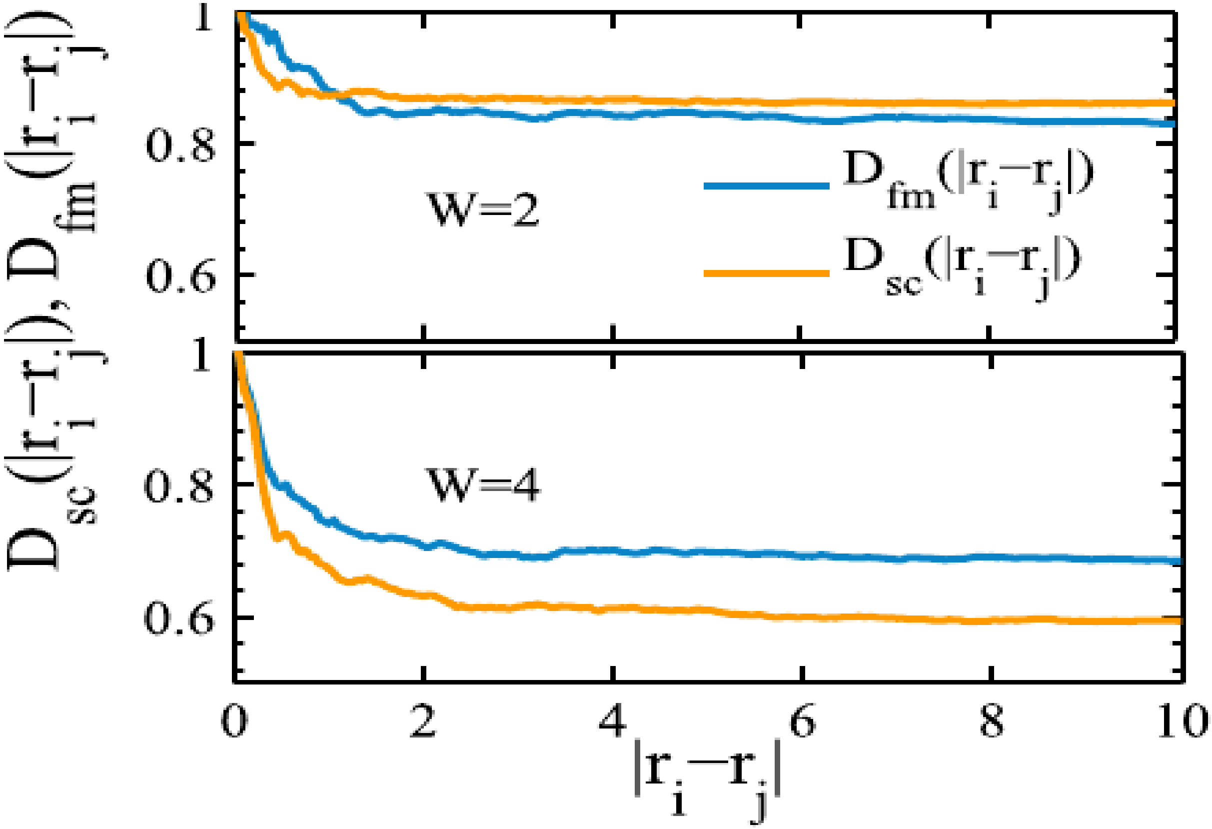

Figure 4. Plots of the correlation functions $D_{\rm fm}(|r_i - r_j|)$ and $D_{\rm sc}(|r_i - r_j|)$ (see text) for local magnetizations and superconducting pair amplitudes respectively as a function of the separation $|r_i - r_j|$. All the plots are normalized to unity at zero separation. The parameters used are $H_x = 0.5$, $\alpha = 0.8$ at $T = 0$.

Nature of SC and FM: DOS and superfluid density

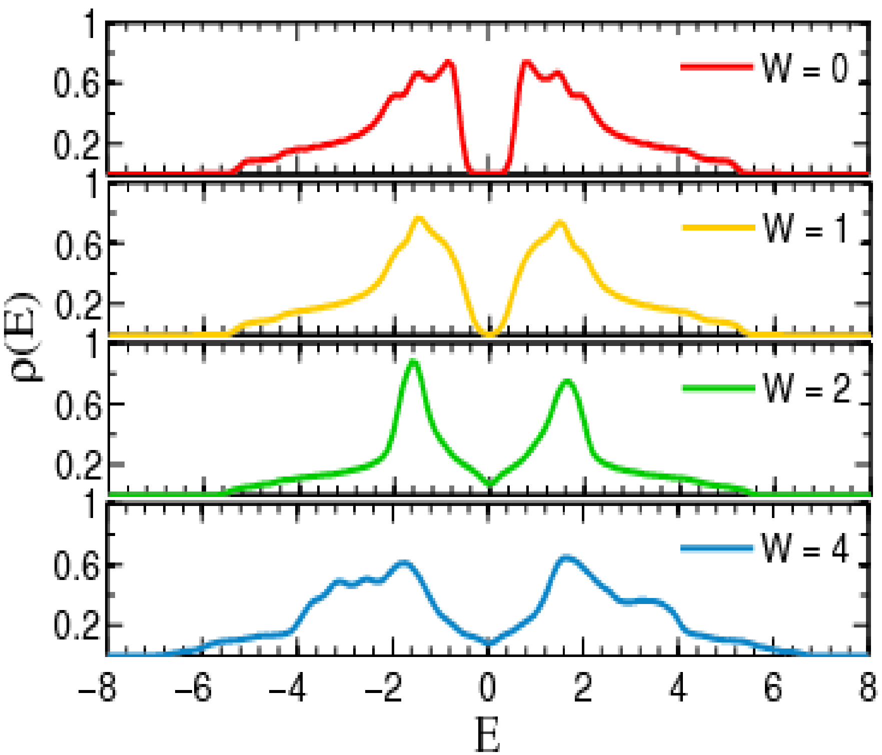

Figure 5. Variation of local density of states with disorder strength ranging from $W = 0$ (homogeneous) to $W = 4$ (highly disordered) with $H_x = 0.5$ and $\alpha = 0.8$ at $T = 0$.

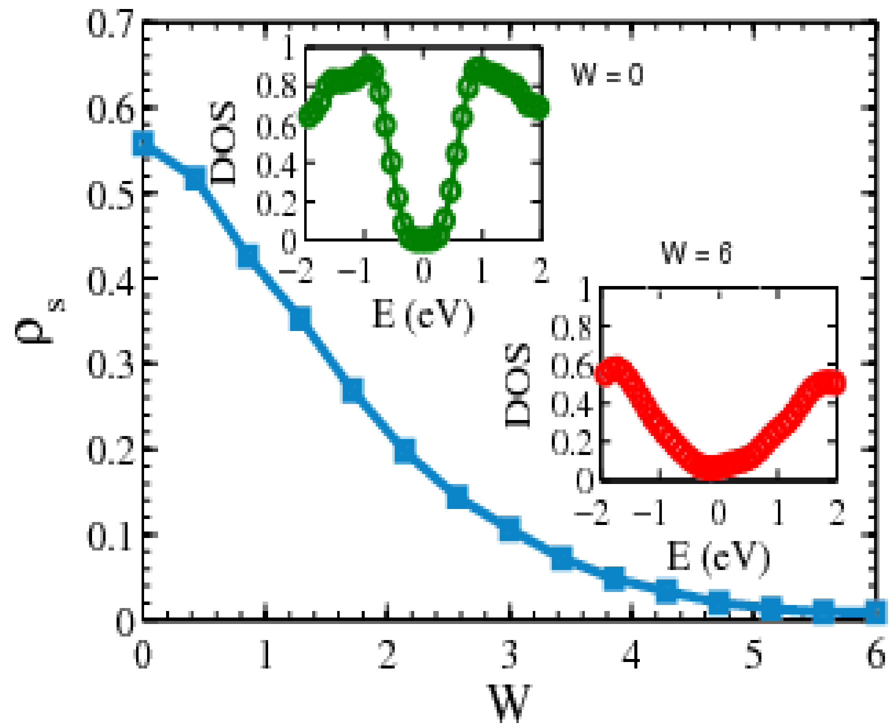

Figure 6. Superfluid density as a function of disorder. Insets show the DOS on both sides of the superconducting transition. Parameters used: $T = 0$, $H_x = 0.5$ and $\alpha = 0.8$.

$$\rho_s \equiv \frac{D_s}{\pi e^2} = -\langle K_x \rangle + \Pi_{xx}(q \to 0, \omega \to 0).$$

N. Mohanta and A. Taraphder JPCM **26**, 025705 (2014)

Finite temperature

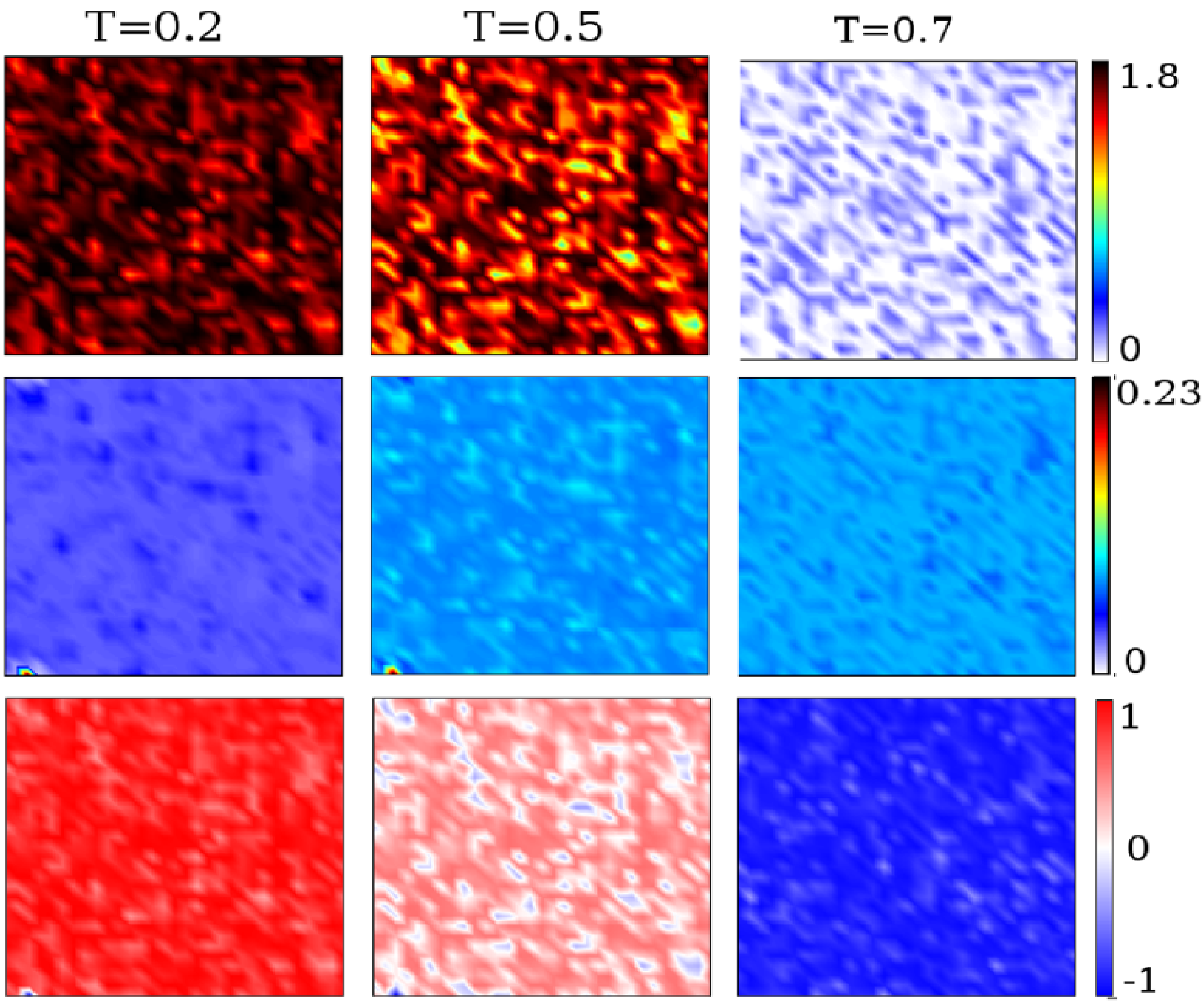

Figure 7. The spatial distribution of the local pairing amplitude $|\Delta(r_i)|$ (top row) and magnetization (middle row). In the bottom row, red and blue represent regions of superconductivity and magnetism respectively. The three columns are for temperature $T = 0.2$, 0.5 and 0.7. The lowest row shows coexistence in combined plots of magnetization and local pairing amplitude. The parameters used are $H_x = 0.5$ and $\alpha = 0.8$ at $W = 1$.

Finite T nature: SC and FM <M> and the correlation function

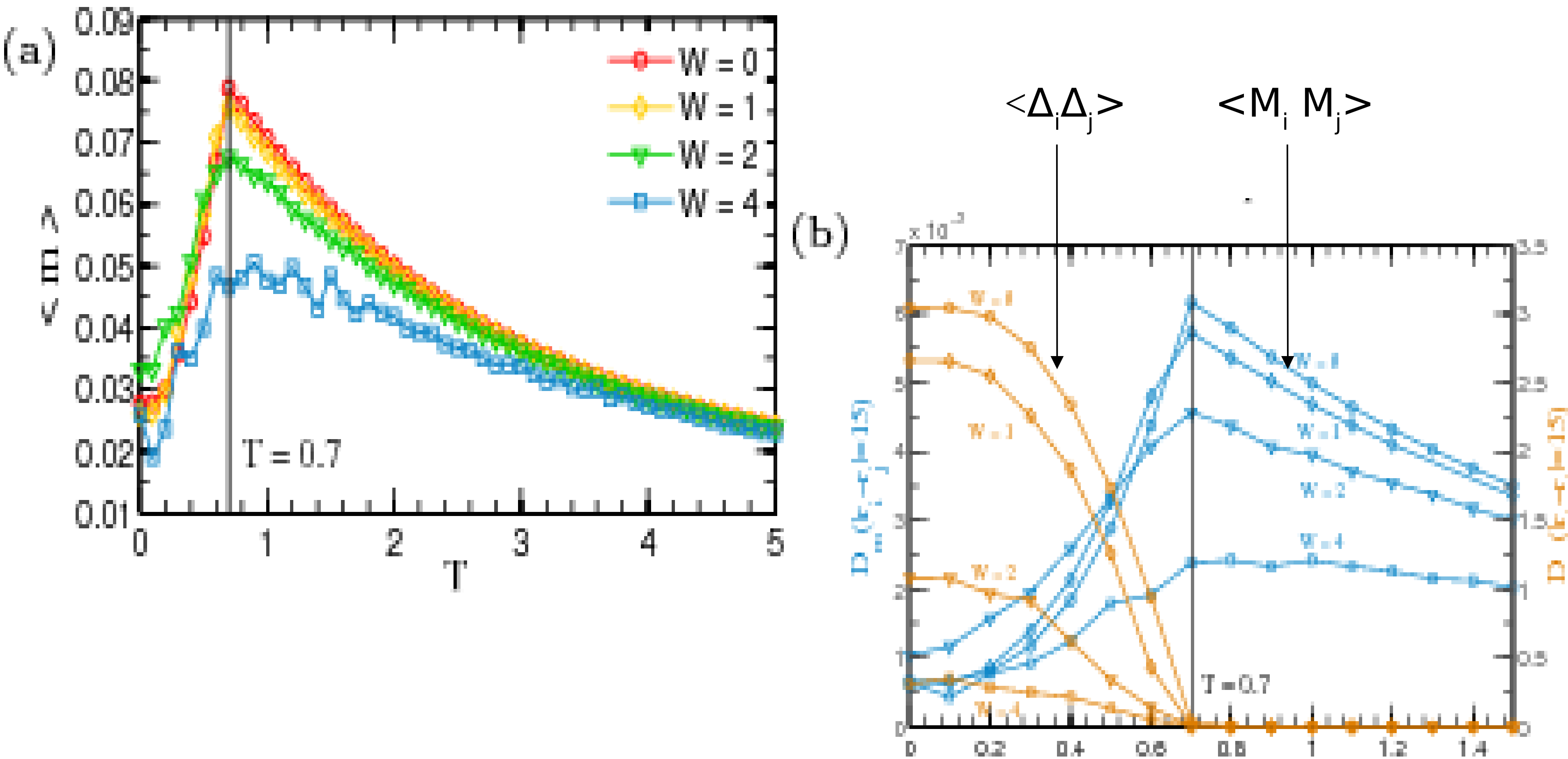

Figure 8. Temperature variations of (a) average magnetizations and (b) correlation functions for different disorder strengths. Beyond $T = 0.7$, superconducting correlation vanishes. Parameters used: $H_x = 0.5$, $\alpha = 0.8$.

N. Mohanta and A. Taraphder JPCM **26**, 025705 (2014)

Filling dependence

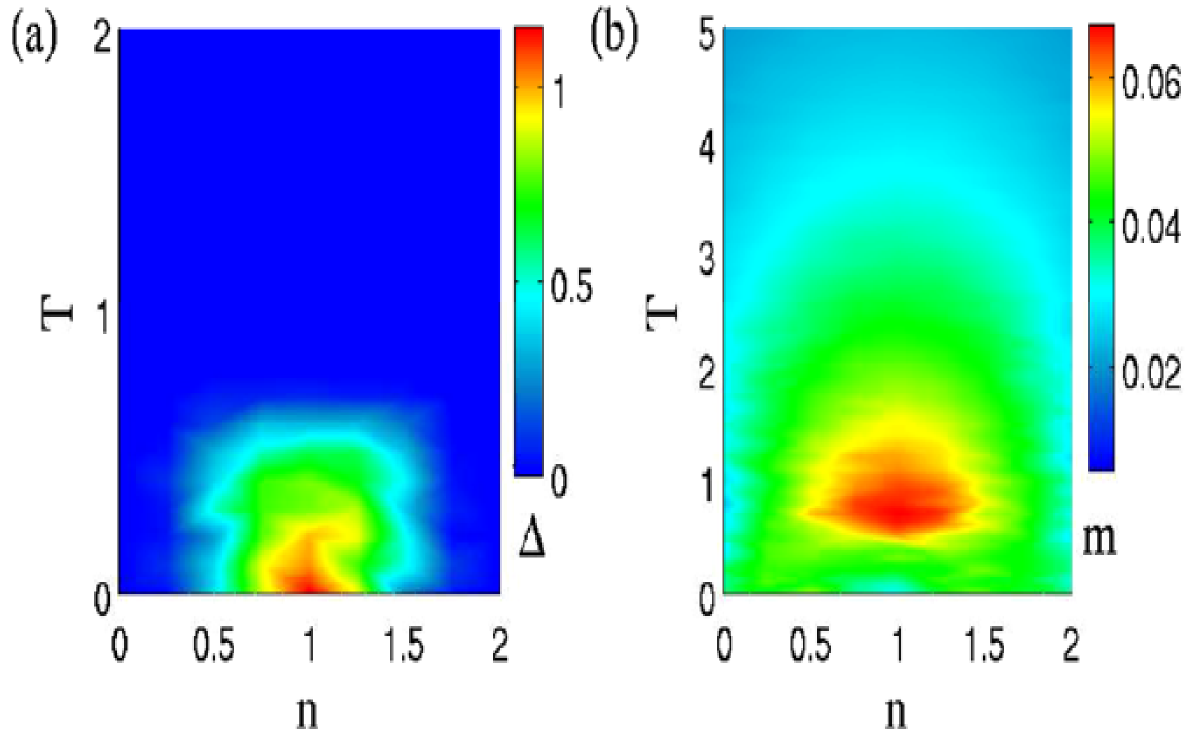

Figure 9. Plots of (a) average pairing amplitude and (b) magnetization in the n–T space for fixed disorder strength $W = 2$. Parameters used: $H_x = 0.5, \alpha = 0.8$.

P-type with O Vacancy

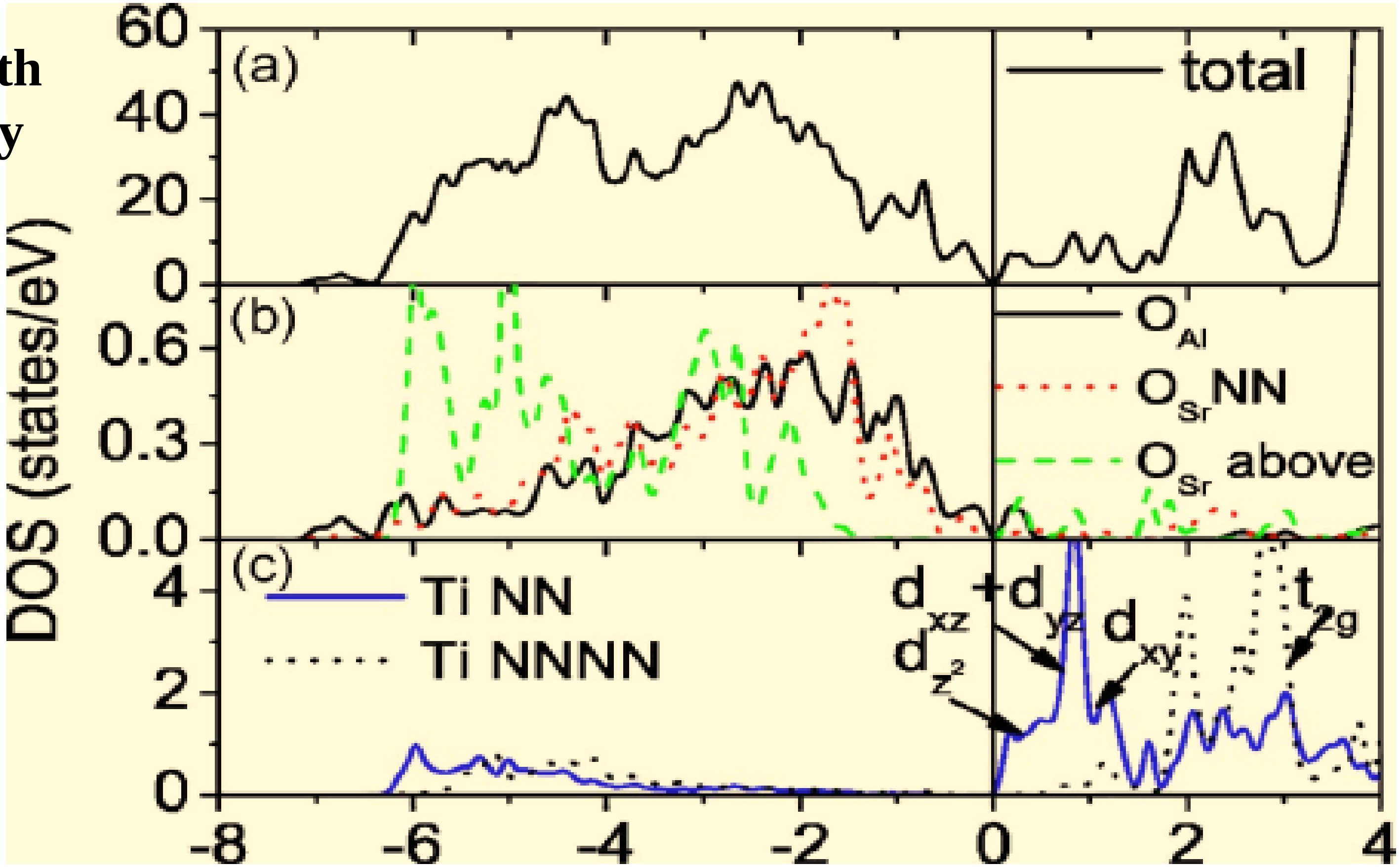

FIG. 9. Density of states of the interface with an oxygen vacancy in the SrO layer: (a) total; (b) projected DOS of the O 2p states of the oxygen atoms surrounding the vacancy in the AlO2 (black), SrO (red, short dashed), as well as in the next SrO layer on top of the vacancy (green, long dashed); (c) d states of the next (blue, solid) and third (black, dashed) Ti neighbor.

Pentcheva, loc. cit

Pseudogap instead of a full gap

Oxygen vacancy clustering: Monte-Carlo study

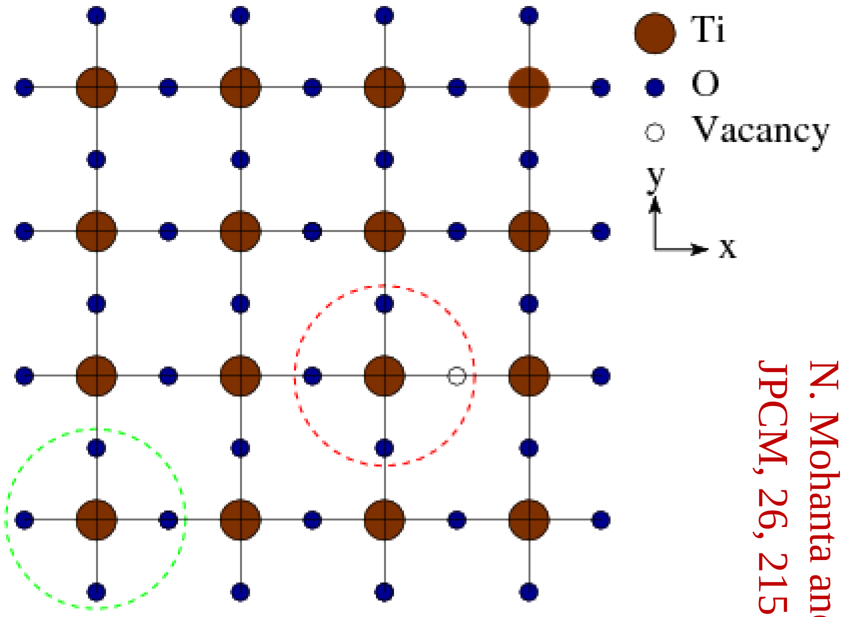

N. Mohanta and AT
JPCM, 26, 215703 (2014)

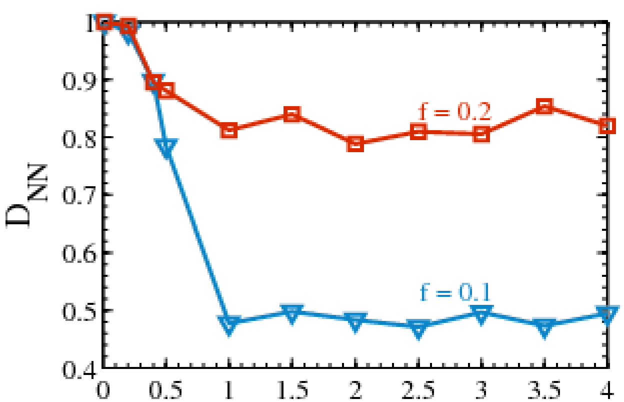

Figure 2. Temperature variation of the nearest neighbour vacancy–vacancy correlation function (normalized to unity) for vacancy concentrations $f = 0.1$ and $f = 0.2$. Parameters used: $\mu = 0$, $\alpha = 0.8$ and $H_x = 0.5$.

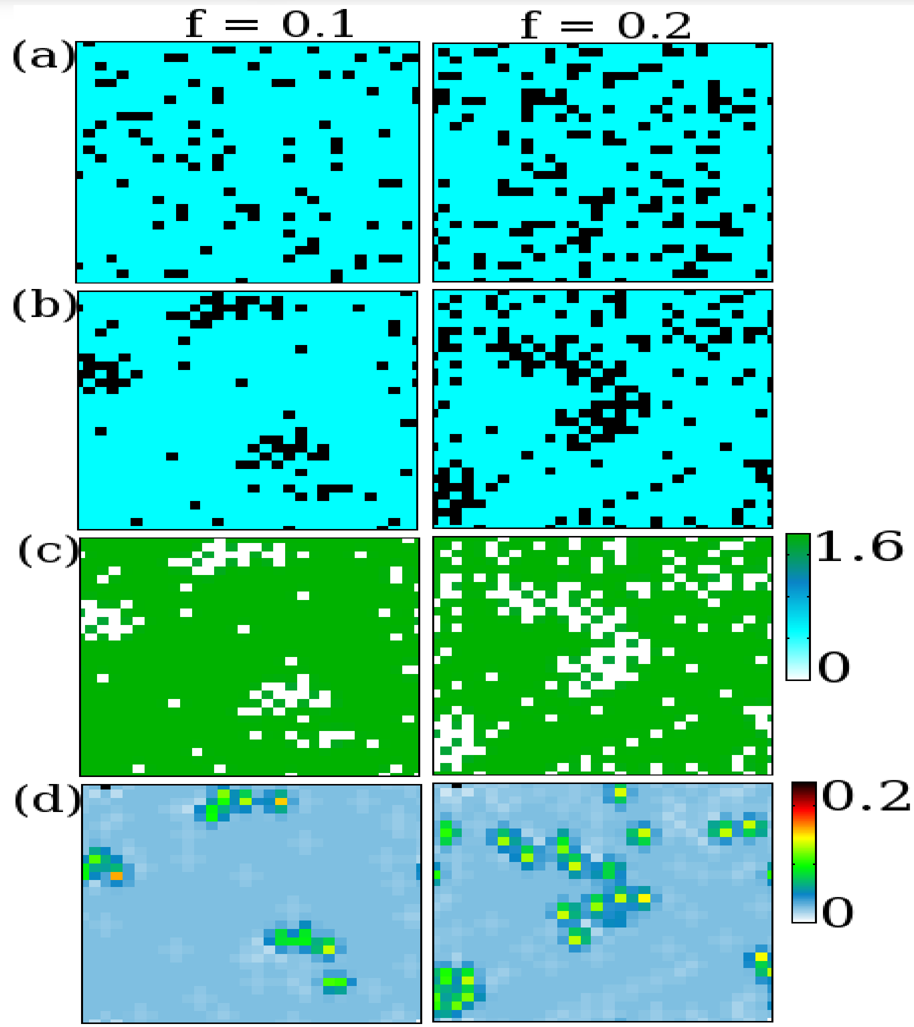

Figure 1. (*a*) Initial and (*b*) final vacancy configurations with vacancy concentration $f = 0.1$ (left column) and $f = 0.2$ (right column). (*c*) and (*d*) show the profiles of the local pairing amplitude and on-site magnetization respectively. Parameters used: $\mu = 0$, $\alpha = 0.8$ and $H_x = 0.5$.

Gap and magnetization

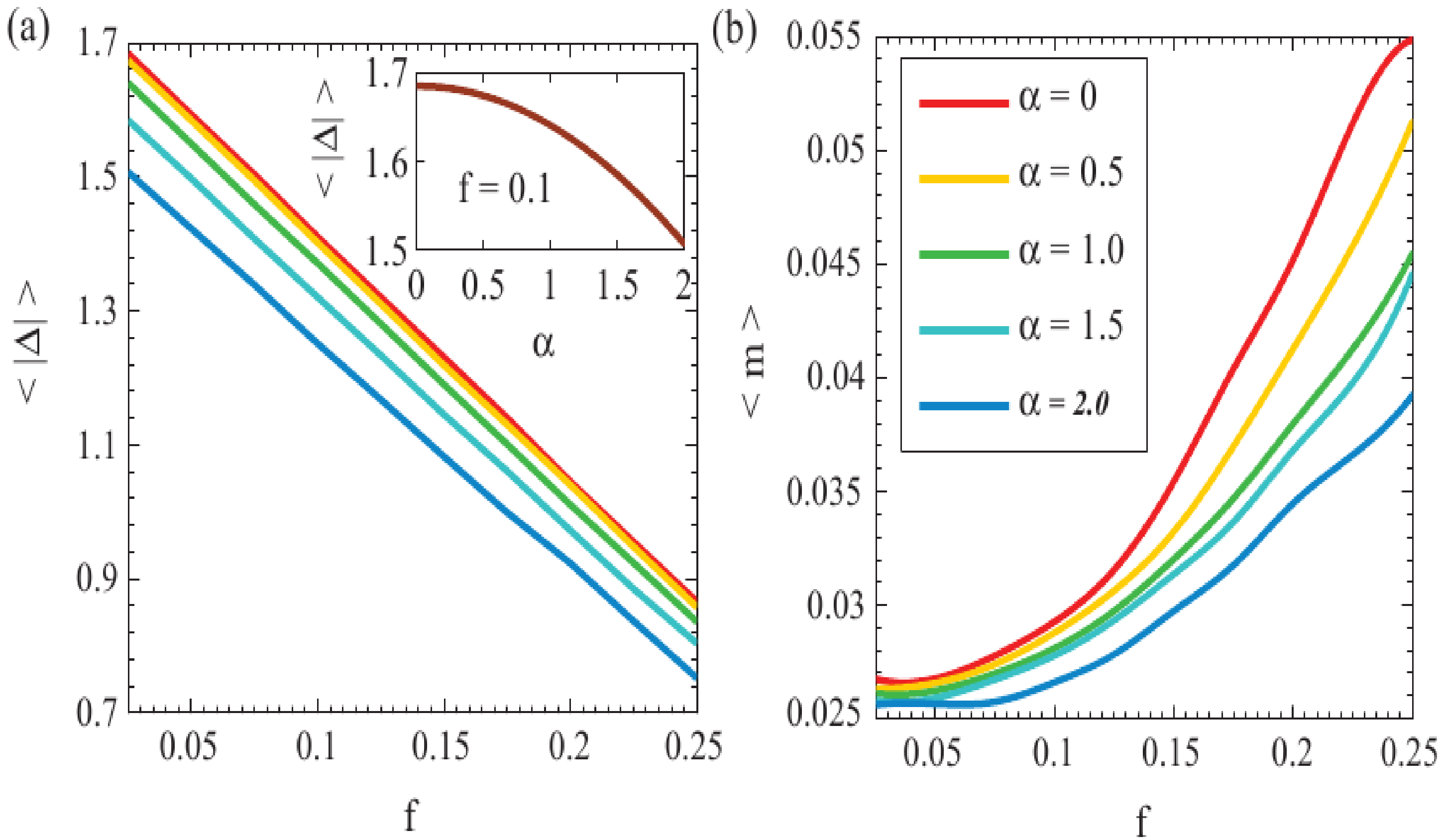

Figure 3. The variation of (*a*) the local superconducting gap parameter and (*b*) the on-site magnetization with the oxygen vacancy concentration for different SO strengths. The inset in (*a*) shows the variation of the mean pairing gap with the SO coupling strength. Parameters used: $\mu = 0$ and $H_x = 0.5$.

N. Mohanta and AT
JPCM, 26, 215703 (2014)

Career freeze-out

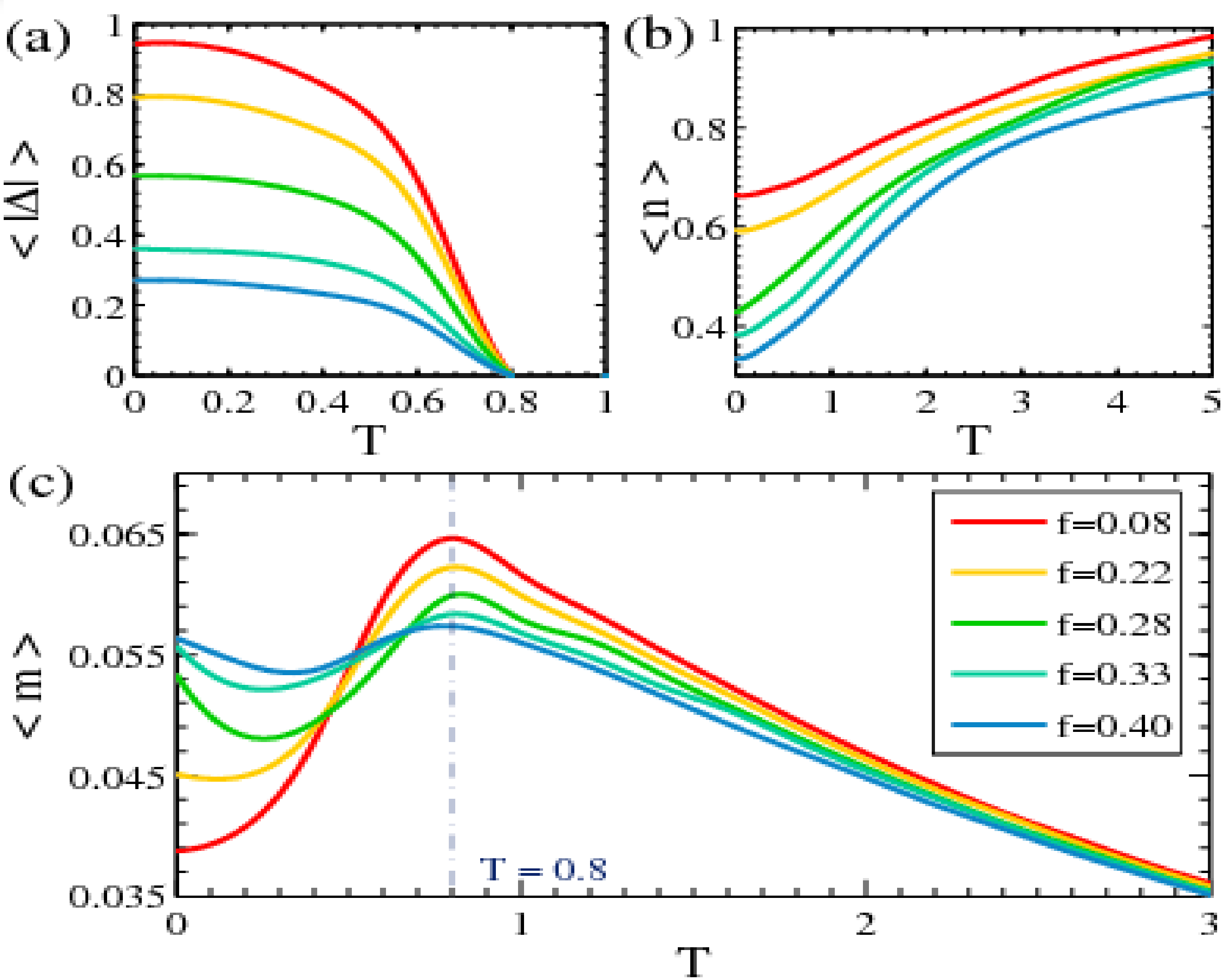

Figure 4. The temperature variations of (*a*) the mean pairing gap, (*b*) the average occupation number and (*c*) the average magnetization for a range of vacancy concentrations. Parameters used: $\alpha = 0.8$ and $H_x = 0.5$.

N. Mohanta and A. Taraphder, JPCM, 26 215703 (2014)

Lifshitz point in the band structure and DOS

N. Mohanata, AT, PRB **92**, 174531 (2015)

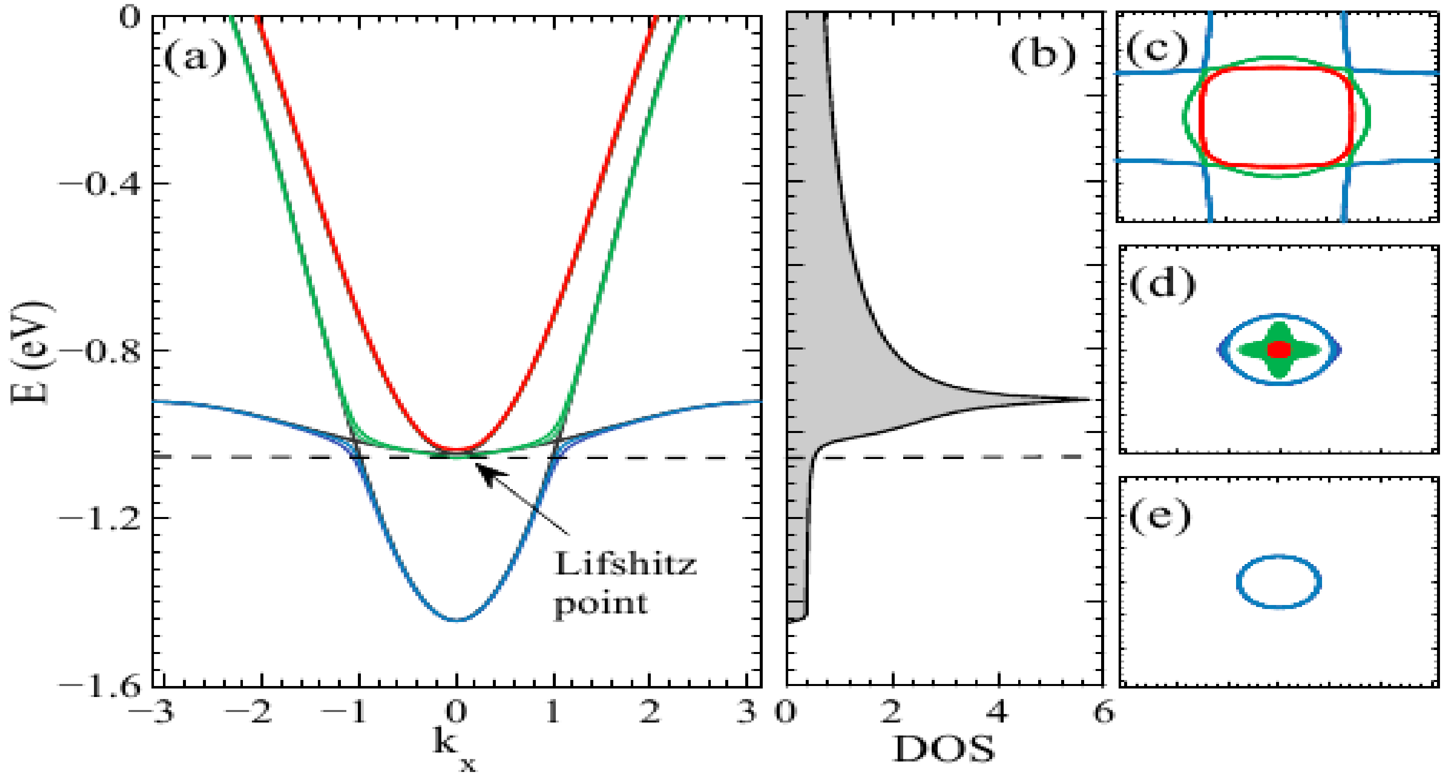

FIG. 1. (Color online) (a) The band structure of the three t_{2g} orbitals in the presence of the Rashba and atomic SOIs (spectrum of $\mathcal{H}_0 + \mathcal{H}_{ASO} + \mathcal{H}_{RSO}$). The spin-orbit interactions result in mixing of the original bands (plotted by black lines). The dashed horizontal line, at $\mu \simeq -1.04$ eV, denotes a Lifshitz transition point at which the two upper bands start getting occupied. (b) the total density of states as a function of energy. The Lifshitz transition is reflected by the sharp jump in the density of states near the transition point. The change in the Fermi-surface topology at energy (c) below, (d) near, and (e) above the Lifshitz transition.

Multi-band superconductivity

$$H = \sum_j \begin{pmatrix} \sum_\beta \Gamma_{\alpha\beta}^{ij\uparrow\uparrow} & \sum_\beta \Gamma_{\alpha\beta}^{ij\uparrow\downarrow} & \Delta_{\alpha\beta\uparrow\uparrow}^{tij}\delta_{\alpha\beta} & \Delta_{\alpha\beta}^{sij}\delta_{\alpha\beta} \\ \sum_\beta \Gamma_{\alpha\beta}^{ij\downarrow\uparrow} & \sum_\beta \Gamma_{\alpha\beta}^{ij\downarrow\downarrow} & -\Delta_{\alpha\beta}^{sij}\delta_{\alpha\beta} & \Delta_{\alpha\beta\downarrow\downarrow}^{tij}\delta_{\alpha\beta} \\ \Delta_{\alpha\beta\uparrow\uparrow}^{tij*}\delta_{\alpha\beta} & -\Delta_{\alpha\beta}^{sij*}\delta_{\alpha\beta} & -\sum_\beta \Gamma_{\alpha\beta}^{ij\uparrow\uparrow*} & -\sum_\beta \Gamma_{\alpha\beta}^{ij\uparrow\downarrow*} \\ \Delta_{\alpha\beta}^{sij*}\delta_{\alpha\beta} & \Delta_{\alpha\beta\downarrow\downarrow}^{tij*}\delta_{\alpha\beta} & -\sum_\beta \Gamma_{\alpha\beta}^{ij\downarrow\uparrow*} & -\sum_\beta \Gamma_{\alpha\beta}^{ij\downarrow\downarrow*} \end{pmatrix}$$

$$\times \begin{pmatrix} u_{n\alpha\uparrow}^j \\ u_{n\alpha\downarrow}^j \\ v_{n\alpha\uparrow}^j \\ v_{n\alpha\downarrow}^j \end{pmatrix} = E_n \begin{pmatrix} u_{n\alpha\uparrow}^j \\ u_{n\alpha\downarrow}^j \\ v_{n\alpha\uparrow}^j \\ v_{n\alpha\downarrow}^j \end{pmatrix}, \tag{5}$$

$$\Gamma_{\alpha\beta}^{ij\sigma\sigma'} = -t_{\alpha\beta}^{ij\sigma\sigma'} - [(\mu - V^{i_d}\delta_{ii_d})\delta_{\sigma\sigma'} - (h_{x\alpha}\sigma_x)_{\sigma\sigma'}]\delta_{ij}\delta_{\alpha\beta}$$

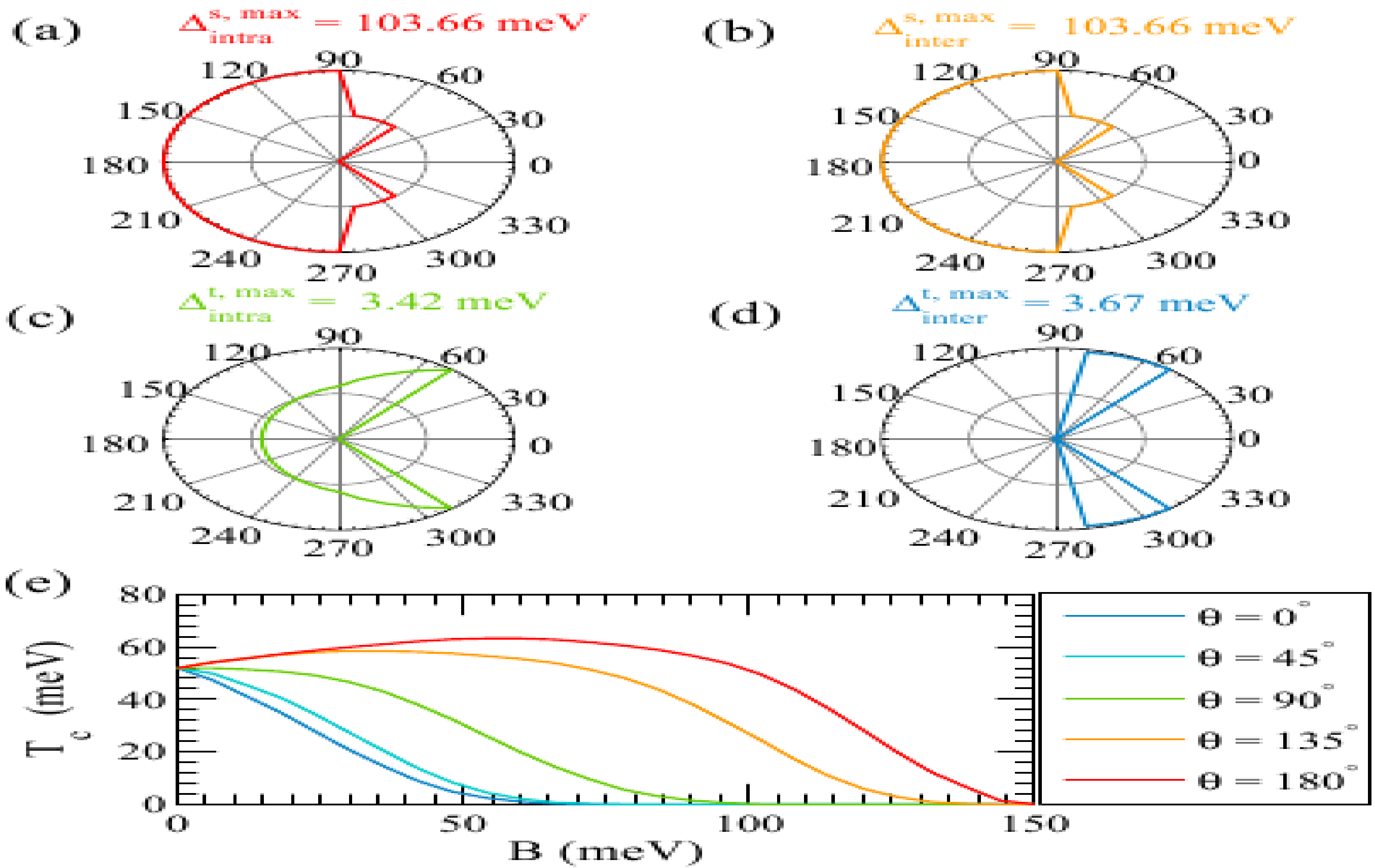

FIG. 5. (Color online) (a)–(d) Polar plots showing the angular variations of the maximum of singlet and triplet pairing amplitudes in the intraband and interband channels. The angle θ is between the initial polarization direction due to the intrinsic ferromagnetism and the applied magnetic field. (e) The variation of the superconducting transition temperature T_c with respect to the amplitude B of the magnetic field. Parameters used are $\mu = -0.6$ eV, $T = 0$ eV, $g = 0.135$ eV, $h_{x1} = 0.4$ eV, $h_{x2} = 0.1$ eV, and $n_d = 0$.

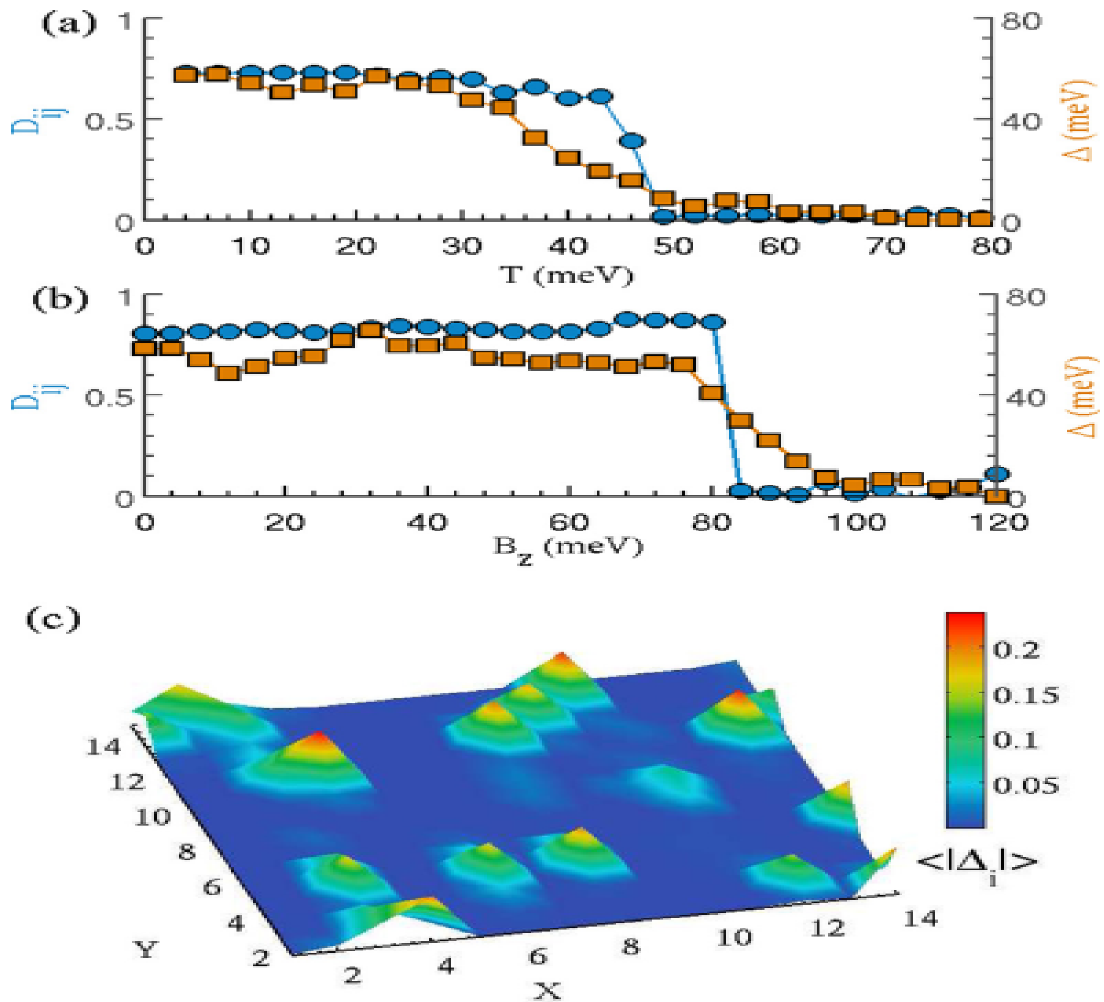

FIG. 7. (Color online) The variation of the phase correlation function D_{ij} and the disorder-averaged and site-averaged pairing amplitude $\langle|\Delta_i|\rangle$ with respect to (a) temperature T and (b) perpendicular magnetic field B_z. (c) The profile of the pairing amplitude $\langle|\Delta_i|\rangle$ at $T = 60$ meV describing the localized Cooper pairs in the nonsuperconducting side of the transition [in (a)]. A 14×14 lattice is used in the calculation. Other parameters are $\mu = -0.6$ eV, $g = 0.135$ eV, $h_{x1} = 0.4$ eV, $h_{x2} = 0.1$ eV, $W = 0.8$ eV, and $n_d = 50$.

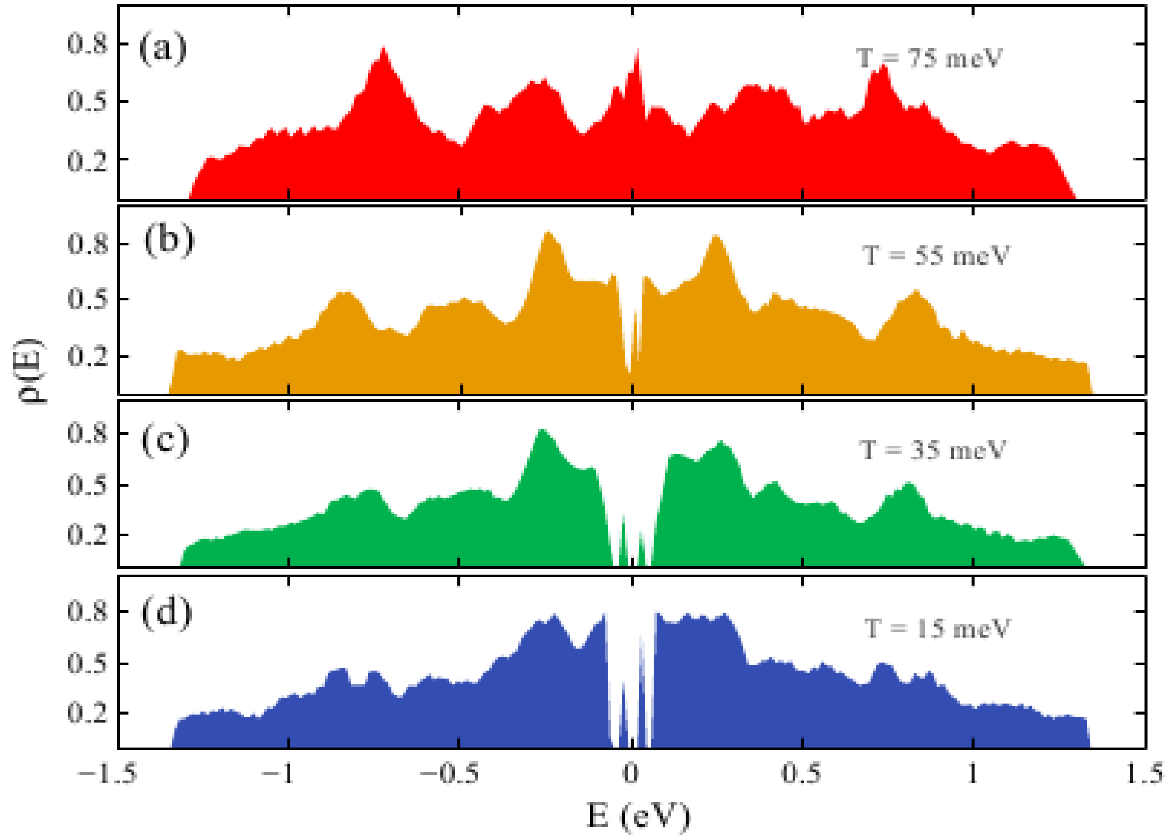

FIG. 8. (Color online) The density of states $\rho(E)$ at temperatures (a) $T = 75$ meV, (b) $T = 55$ meV, (c) $T = 35$ meV, and (d) $T = 15$ meV across the transition to the superconducting state. Parameters: are $\mu = -0.6$ eV, $g = 0.135$ eV, $h_{x1} = 0.4$ eV, $h_{x2} = 0.1$ eV, $W = 0.8$ eV, and $n_d = 50$.

Search for Lifshitz transition (LT) in LAO/STO

a

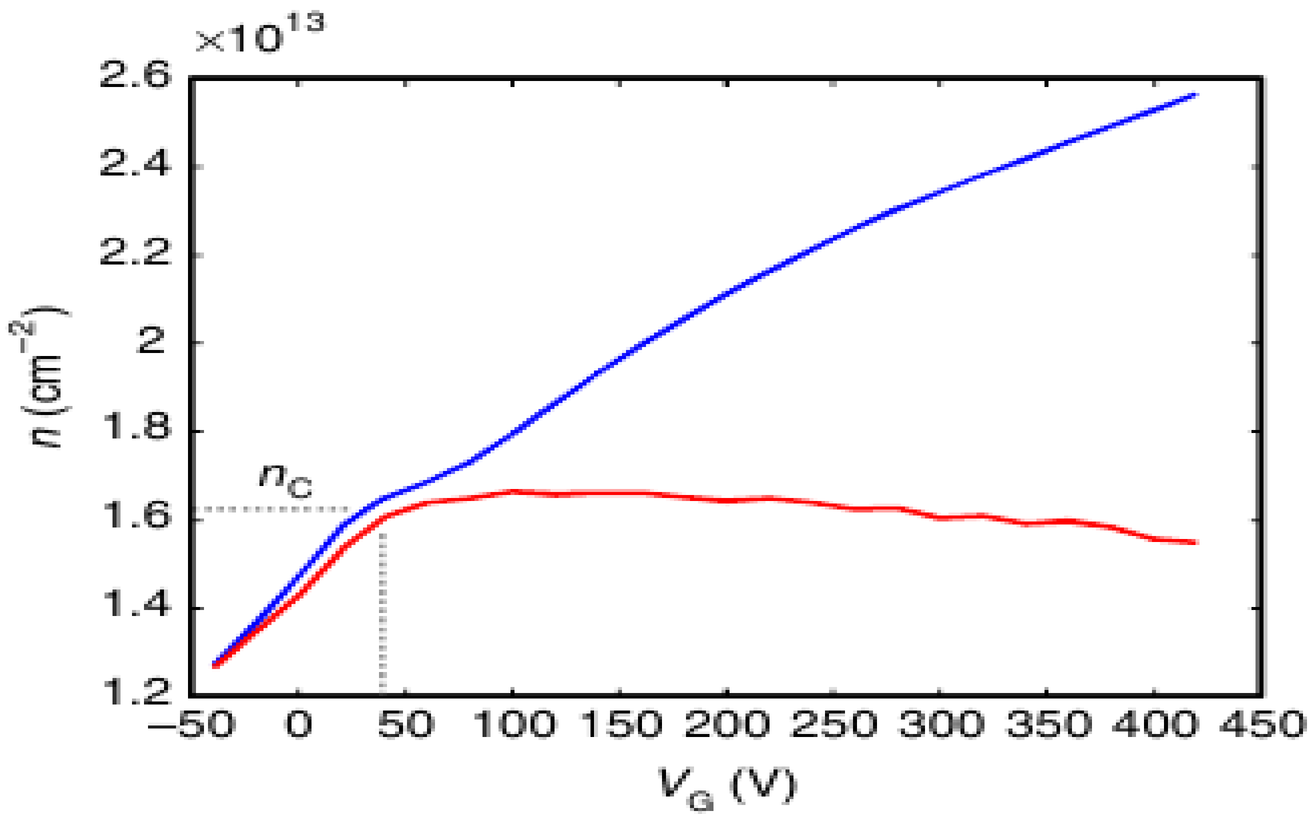

Figure 3 | Universality of the critical density and its energy bands origin. (**a**) Densities extracted from measured Hall coefficient ($n = 1/eR_H$, e is electr charge) at $B = 0\ T$ (red) and $B = 14$ T (blue) versus V_G. The former reflects (see text) the density of high mobility carriers, n_{hi}, and the latter the total density, n_{total}. Below V_C (dashed vertical line), $n_{total} \approx n_{hi}$ and both increase with V_G up to the critical value, n_C, (dashed horizontal line) reached at V_C. Above V_C, n_{hi} saturates whereas n_{total} continues to increase. The data shown are from a 6 u.c. sample grown at $T_{growth} = 800\,°C$. (**b**–**e**) Similar analysis

Joshua, et al. Nat.Comm. 2116 (2012)

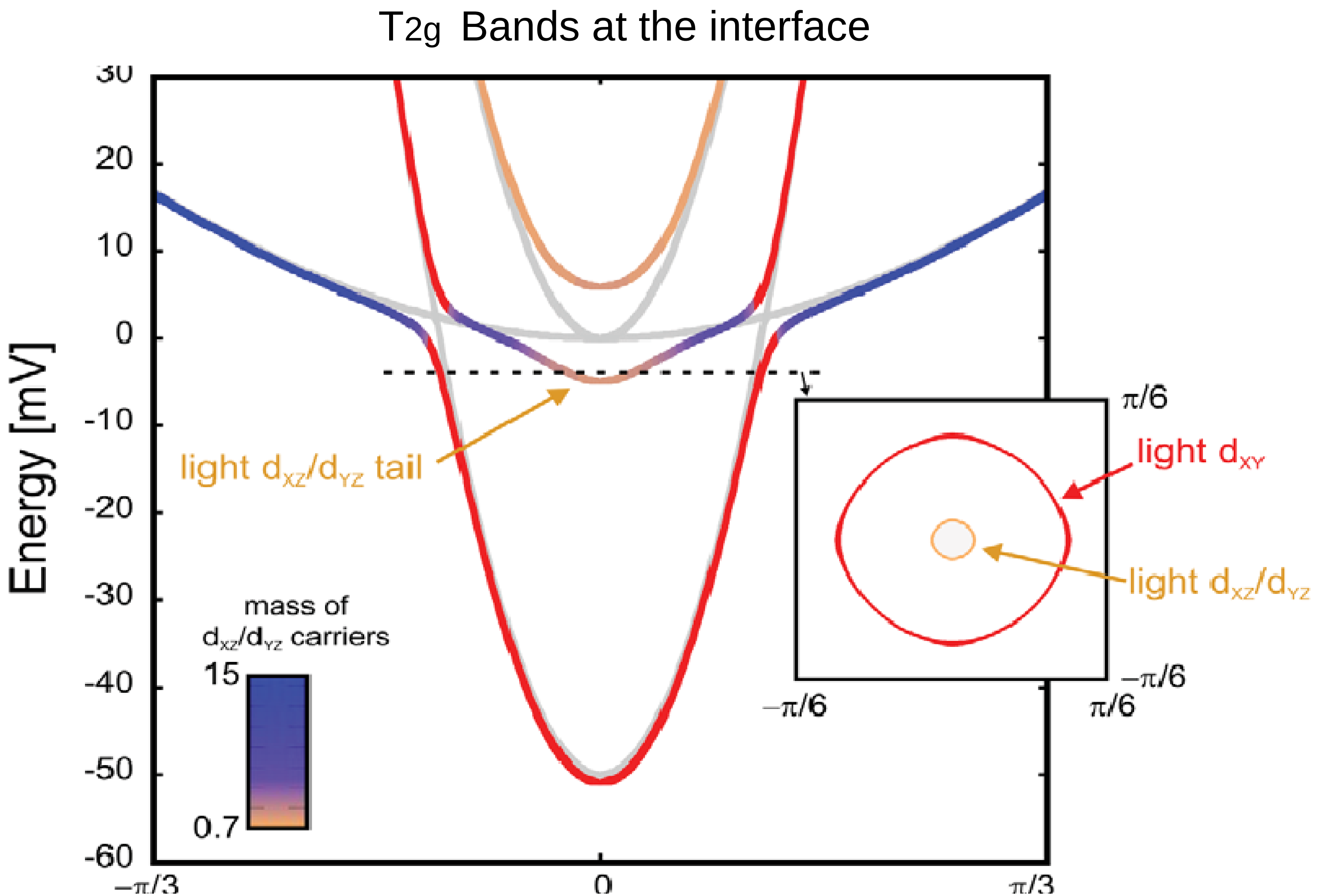

Figure S1: The band structure at the LAO/STO interface with atomic spin-orbit (ASO) interactions. The main panel shows the energy bands without ASO (gray) and with ASO (colored) calculated with the ARPES measured[6] values for the light and heavy masses, $m_l = 0.7m_e$ and $m_h = 15m_e$ (m_e is the electronic mass), an energy splitting of $\Delta_E = 50meV$, and taking the strength of ASO to be

Bands and DOS across LT

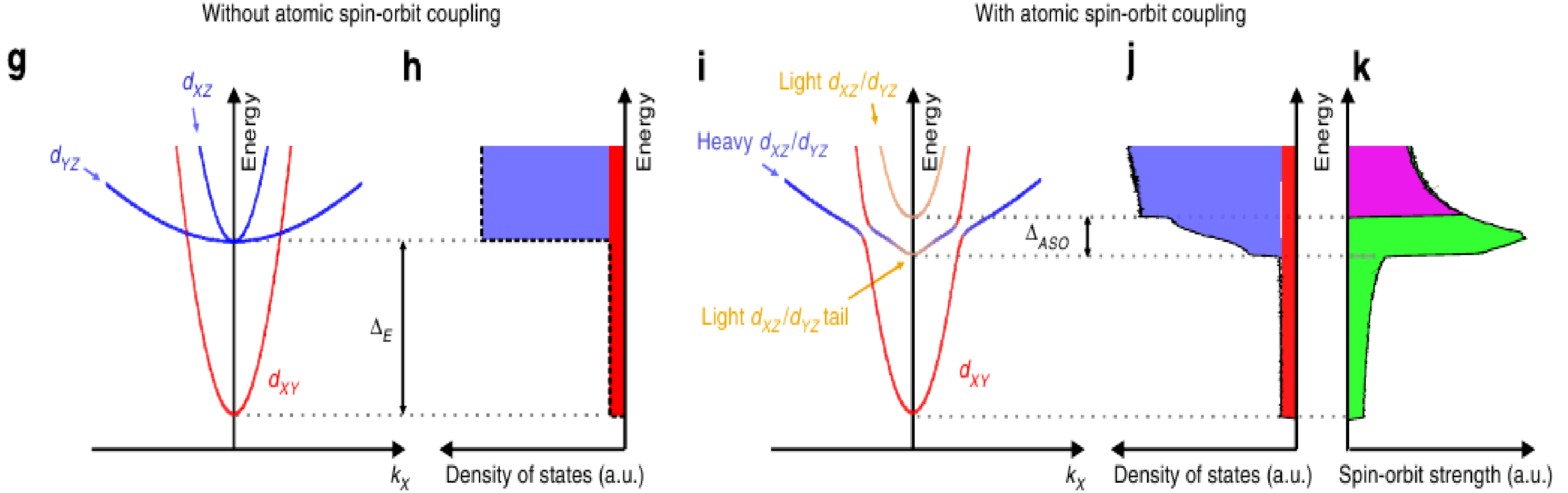

(green) and sample 4: 10 u.c., T_{growth} = 650 °C (blue). (**g**) *d*-Orbital energy bands of STO near its interface with LAO. The d_{XY} band is lower in energy by Δ_E compared with the d_{XZ} and d_{YZ} bands. (**h**) Schematic DOS versus energy. The d_{XY} band has approximately ten times smaller DOS (red) than combine DOS of d_{XZ} and d_{YZ} bands (blue; see text). (**i**) Calculated band structure including ASO interactions. At the Γ point the bands split by Δ_{ASO} (see also Supplementary Fig. S3 and Supplementary Methods). (**j**) Calculated DOS with ASO. The sharp jump of (**h**) is smeared over a Δ_{ASO} scale. (**k**) Strength

SC peak at LT

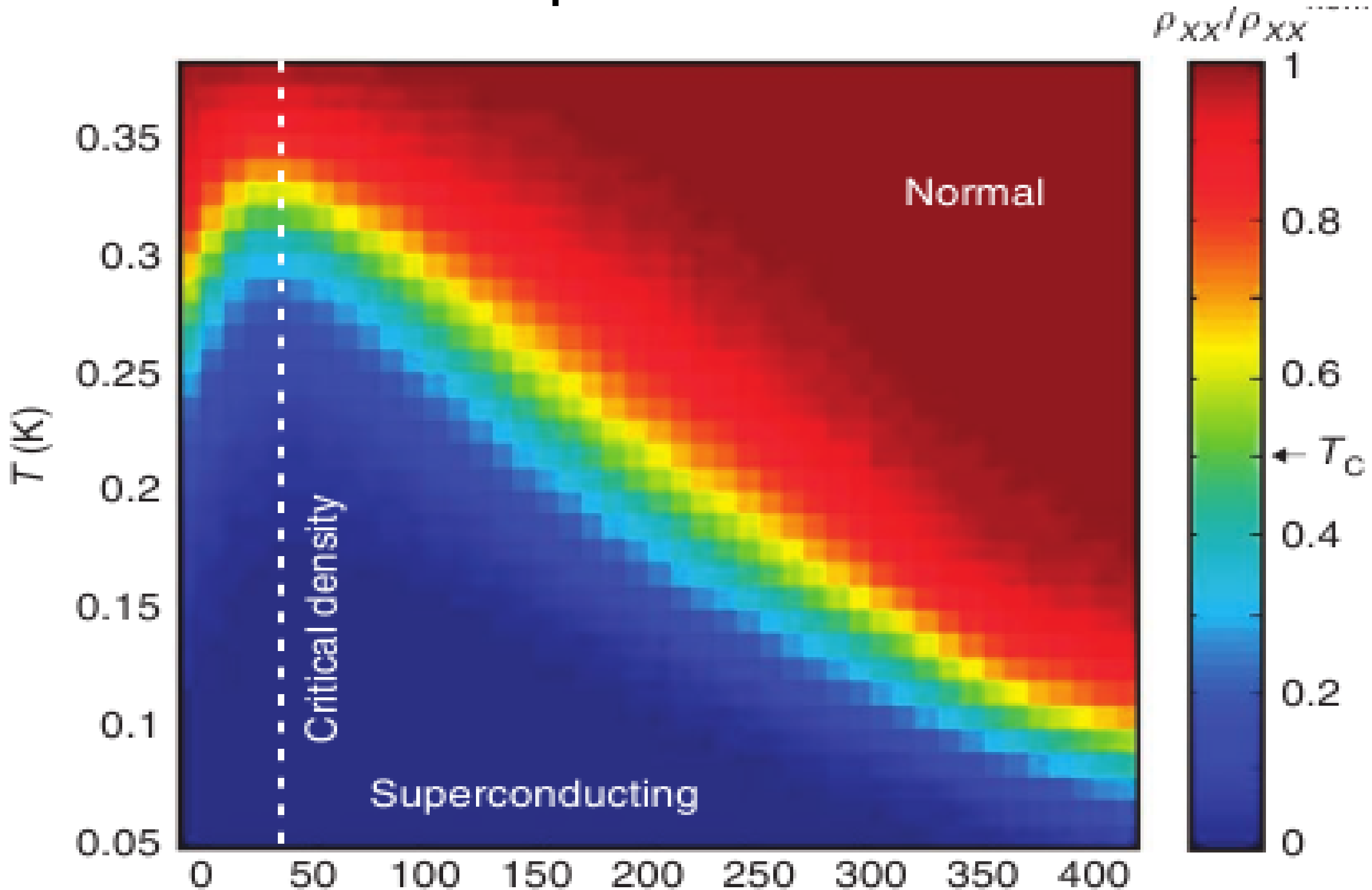

Figure 4 | Correlation between superconductivity and the critical density. ρ_{xx} measured versus temperature and gate voltage, divided by its normal-state value at $T = 0.38$ K. Red and blue colours correspond to the normal and superconducting states. The superconducting transition temperature, T_C, defined by $\rho_{xx}(T_C)/\rho_{xx}(T = 0.38K) = 1/2$, has a dome shape as function of V_G. The critical density (white dashed line) is found to be at the peak of the dome.

An LDA+DMFT Study

$$\mathcal{H}_{\rm eff} = \mathcal{H}_0 + \mathcal{H}_{\rm ASO} + \mathcal{H}_{\rm RSO} + \mathcal{H}_{\rm FM} + \mathcal{H}_{\rm SC} + \mathcal{H}_{\rm dis}$$

LDA

$$\mathcal{H}_{\rm ASO} = \Delta_{\rm so}\vec{l}\cdot\vec{s},$$

$$\mathcal{H}_{\rm ASO} = \frac{\Delta_{\rm so}}{2}\sum_k (c^\dagger_{ka\uparrow} \quad c^\dagger_{kb\uparrow} \quad c^\dagger_{kc\uparrow} \quad c^\dagger_{ka\downarrow} \quad c^\dagger_{kb\downarrow} \quad c^\dagger_{kc\downarrow})$$

$$\times \begin{pmatrix} 0 & 0 & 0 & 0 & 1 & -i \\ 0 & 0 & i & -1 & 0 & 0 \\ 0 & -i & 0 & i & 0 & 0 \\ 0 & -1 & -i & 0 & 0 & 0 \\ 1 & 0 & 0 & 0 & 0 & -i \\ i & 0 & 0 & 0 & i & 0 \end{pmatrix} \begin{pmatrix} c_{ka\uparrow} \\ c_{kb\uparrow} \\ c_{kc\uparrow} \\ c_{ka\downarrow} \\ c_{kb\downarrow} \\ c_{kc\downarrow} \end{pmatrix}, \quad (1)$$

$$\Delta_{\rm so} = 19.3 \text{ meV}$$

$$\mathcal{H}_{\rm RSO} = \gamma \sum_{k,\sigma} (c^\dagger_{ka\sigma} \quad c^\dagger_{kb\sigma} \quad c^\dagger_{kc\sigma})$$

$$\times \begin{pmatrix} 0 & -2i\sin k_x & -2i\sin k_y \\ 2i\sin k_x & 0 & 0 \\ 2i\sin k_y & 0 & 0 \end{pmatrix} \begin{pmatrix} c_{ka\sigma} \\ c_{kb\sigma} \\ c_{kc\sigma} \end{pmatrix}$$

$$\mathcal{H}_U = \sum_\alpha U_{\alpha\alpha'} n_\alpha n_{\alpha'} + \sum_{\alpha\neq\beta,\alpha+1} U_{\alpha\beta} n_\alpha n_\beta$$

Interaction

$$\alpha = 1,3,5, \ \alpha' = \alpha + 1, \ \beta = 1,2,3,4,5,6$$

3x2-BAND MODEL HAMILTONIAN

$$\mathcal{H} = \mathcal{H}_0 + \mathcal{H}_{ASO} + \mathcal{H}_{RSO}$$

describes the band dispersion of the electrons in the three t_{2g} orbitals.

Atomic spin-orbit coupling.

$$\Delta_{so}\vec{l} \cdot \vec{s}$$

$$\Delta_{so} = 19.3$$

Rashba Spin-orbit coupling

$$\gamma = 20 \text{ meV}$$

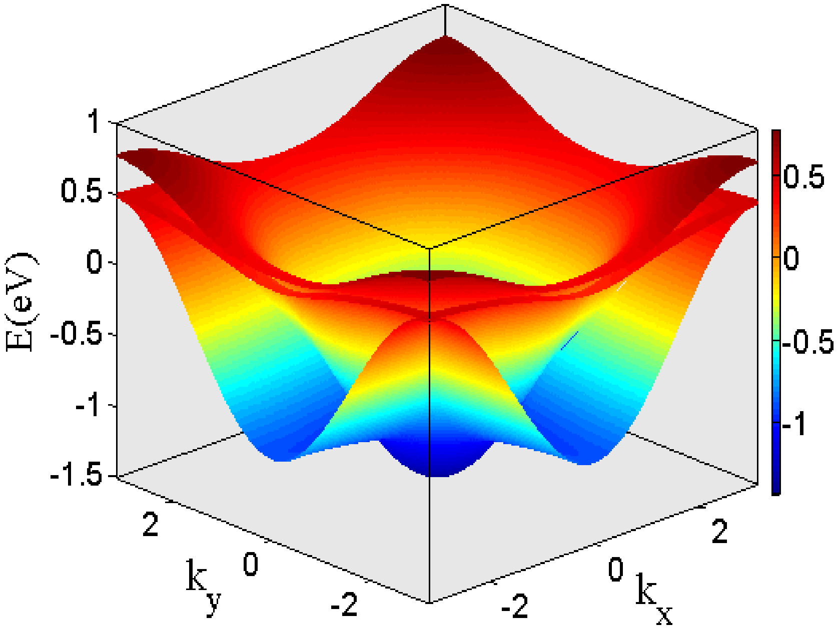

3D band dispersion of the q2DEL at the interface

Correlation effects on LT by DMFT

S. Nandy, S. Acharya, D. Dey, **A Taraphder**, *Phys. Rev. B* ***94***, *155103* (2016)

The effective Hamiltonian $\Rightarrow$ $\mathcal{H}_{eff} = \mathcal{H} + \mathcal{H}_U$

$$\mathcal{H} = \mathcal{H}_0 + \mathcal{H}_{ASO} + \mathcal{H}_{RSO}$$

$$\mathcal{H}_U = \sum_{\alpha,\alpha'} U_{\alpha\alpha'} n_\alpha n_{\alpha'} + \sum_{\alpha,\beta} U_{\alpha\beta} n_\alpha n_\beta$$

$U_{\alpha\alpha'}$ $\rightarrow$ Repulsive interaction energies for nearly degenerate orbitals. $\{\alpha = 1,3,5,\ \alpha' = \alpha + 1\}$

$U_{\alpha\beta}$ $\rightarrow$ Repulsive interaction energies for widely separated orbitals. $\{\alpha = 1,2,\ \beta = 3,4\}$ $\{\alpha = 3,4, \beta = 5,6\}$

$$U_{\alpha\beta} = \frac{U_{\alpha\alpha'}}{5}$$

Lifshitz transition: what is the signature in LAO/STO?

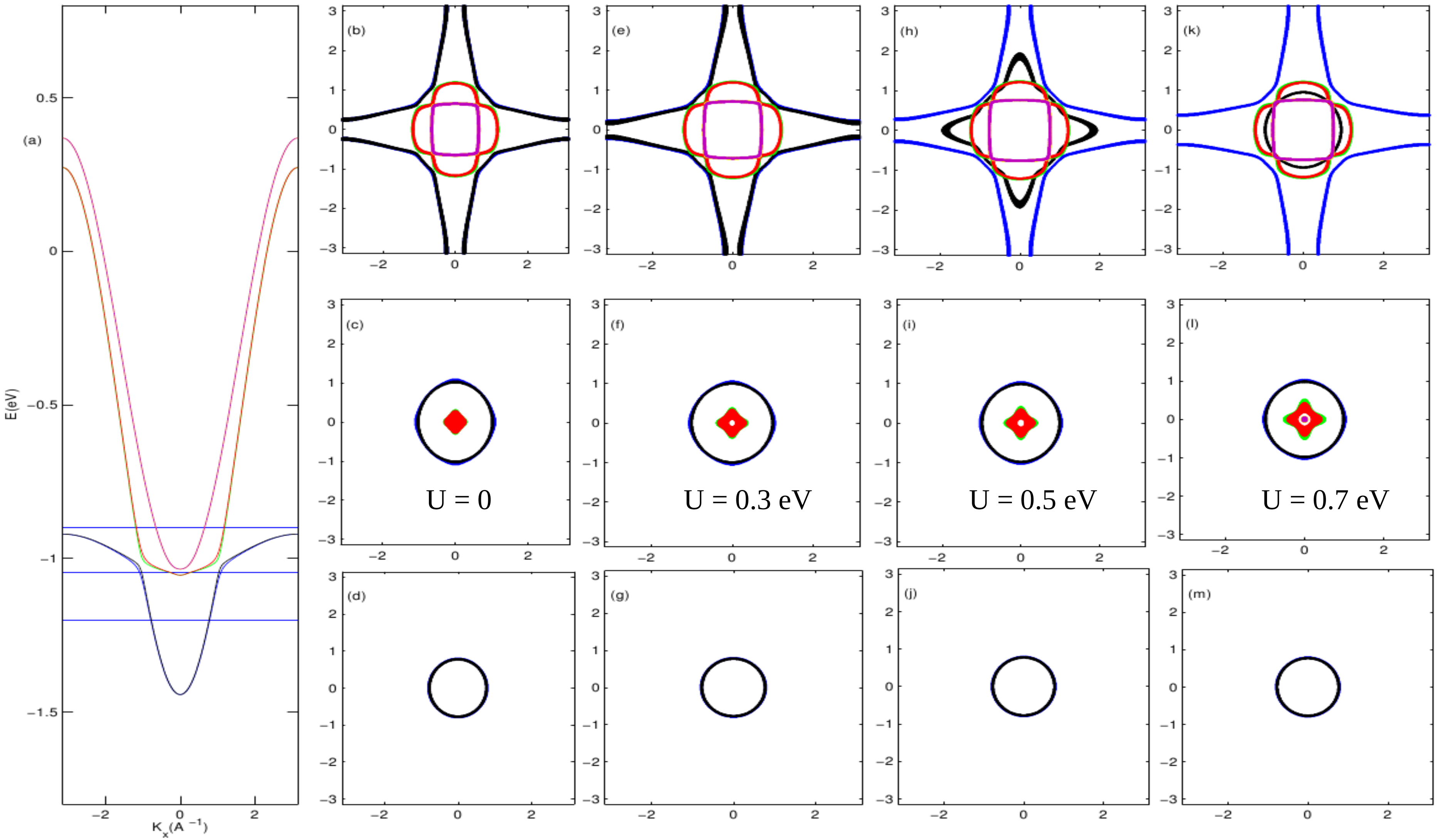

[Fig: (Color online)(a) The band structure of the three t_2g orbitals in presence of the Rashba and atomic SOI (spectrum of H_0 + H_ASO + H_RSO). There is a mixing of the d_xy orbital with the d_yz orbital and the d_zx orbital due to the Rashba SOI. After mixing we have six orbitals as shown (blue, black, green, red, magneta, cyan). (b)-(c)-(d) depict the non-interacting (U = 0) Fermi surfaces below (n = 0.0945), near (n = 0.1809) and above (n = 0.8030) the Lifshitz point ('mu ~ -1.05 eV) at which the third and fourth bands start getting occupied. (e)-(m) show interacting Fermi surfaces at 60K at the interface. Third column, Fourth column and Fifth column show the evolution of the Fermi surface topology

ARPES Spectral Function

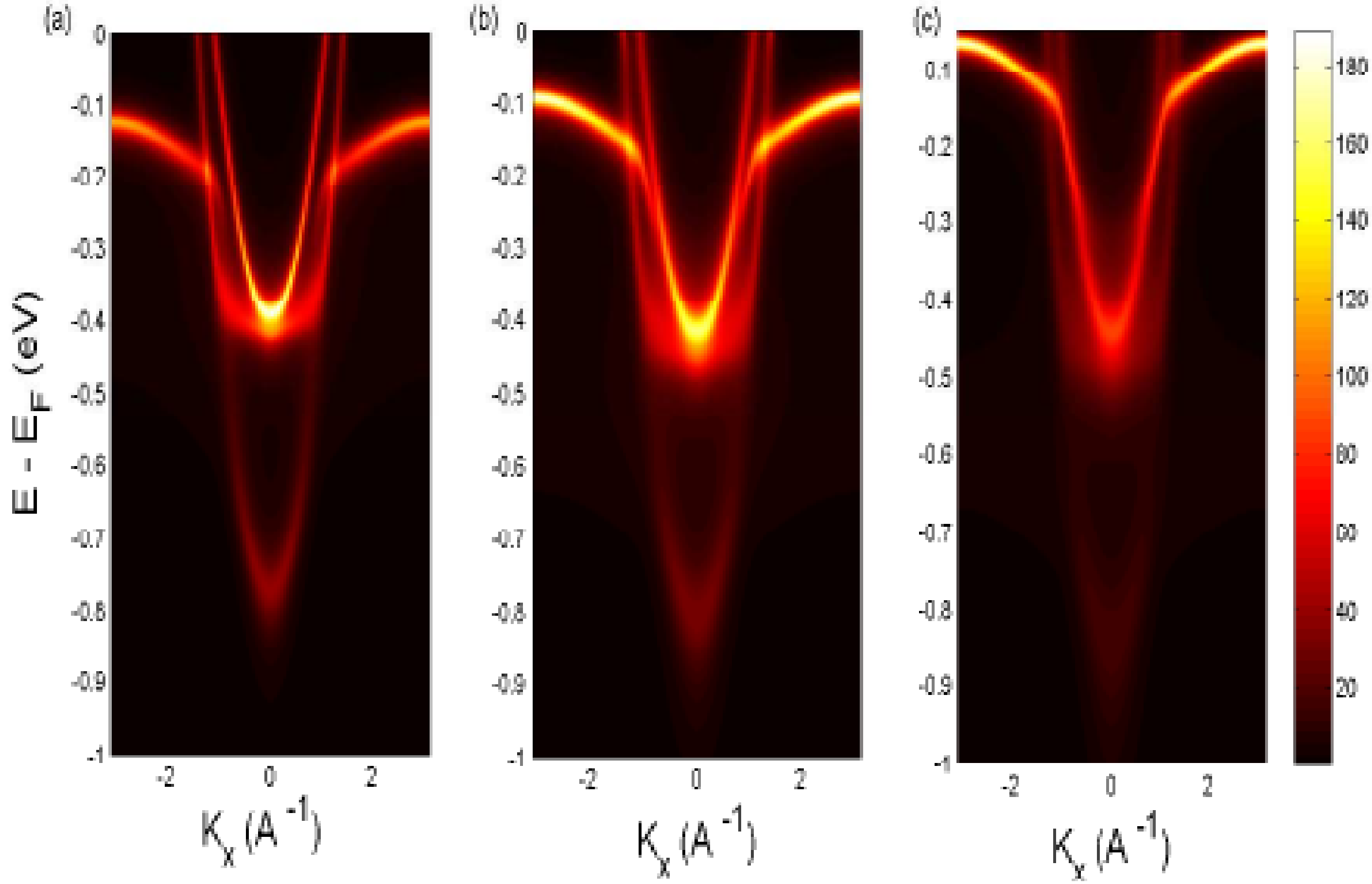

FIG. 6. (Color online) k-resolved spectral data of all bands at the interface at 60K. (a)-(b)-(c) depict the spectral data at filling $n = 1.4030$ for $U = 0.3$ eV, 0.4 eV and 0.5 eV respectively.

Correlation effects (from DMFT) on LT

The effective Hamiltonian

$$\mathcal{H}_{eff} = \mathcal{H} + \mathcal{H}_U$$

$$\mathcal{H} = \mathcal{H}_0 + \mathcal{H}_{ASO} + \mathcal{H}_{RSO}$$

$$\mathcal{H}_U = \sum_{\alpha,\alpha'} U_{\alpha\alpha'} n_\alpha n_{\alpha'} + \sum_{\alpha,\beta} U_{\alpha\beta} n_\alpha n_\beta$$

$U_{\alpha\alpha'}$ → Repulsive interaction energies for nearly degenerate orbitals. $\{\alpha = 1,3,5,\ \alpha' = \alpha + 1\}$

$U_{\alpha\beta}$ → Repulsive interaction energies for widely separated orbitals. $\{\alpha = 1,2,\ \beta = 3,4\}$ $\{\alpha = 3,4, \beta = 5,6\}$

$$U_{\alpha\beta} = \frac{U_{\alpha\alpha'}}{5}$$

DMFT FERMI SURFACES

2D dispersion **U= 0** **U=0.3 eV** **U=0.5 eV** **U=0.7 eV**

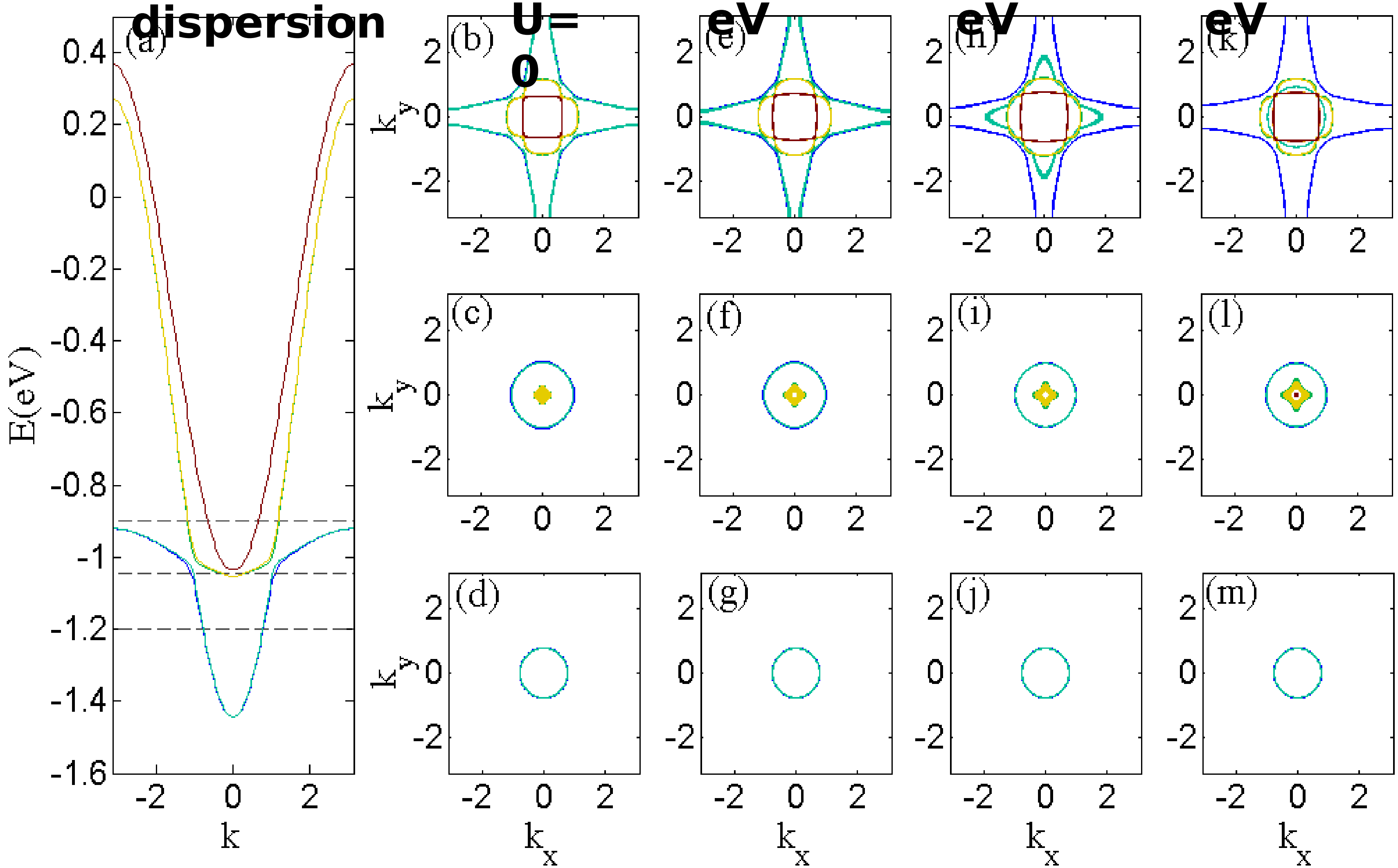

$\mu = -1.20$ eV
$n = 0.0945$ el./u.c.

$\mu = -1.05$ eV
$n = 0.1809$ el./u.c.

$\mu = -0.90$ eV
$n = 0.8030$ el./u.c.

Fermi Surfaces and LT

Non-interacting case

As μ is tuned up, new electron-like pockets appear at $\mu_c = 1.067$ eV where 3rd and 4th orbitals start getting occupied and **LT occurs**.

Exists another critical density → 5th and 6th orbitals will appear at the → Fermi Level new pockets will form.

difference between these two critical densities is quite small to distinguish

Interaction

$$E_{k\alpha} = E^0_{k\alpha} - \mu + Re\Sigma_\alpha(\mathrm{k}, E_{k\alpha})$$

With increasing U, nearly degenerate pairs of orbitals tend to split up.

The 5th and 6th orbitals also appear as new electron-like pockets in the Fermi surface

Critical densities for the transitions are reduced in the presence of strong interaction.

Seebeck coefficient

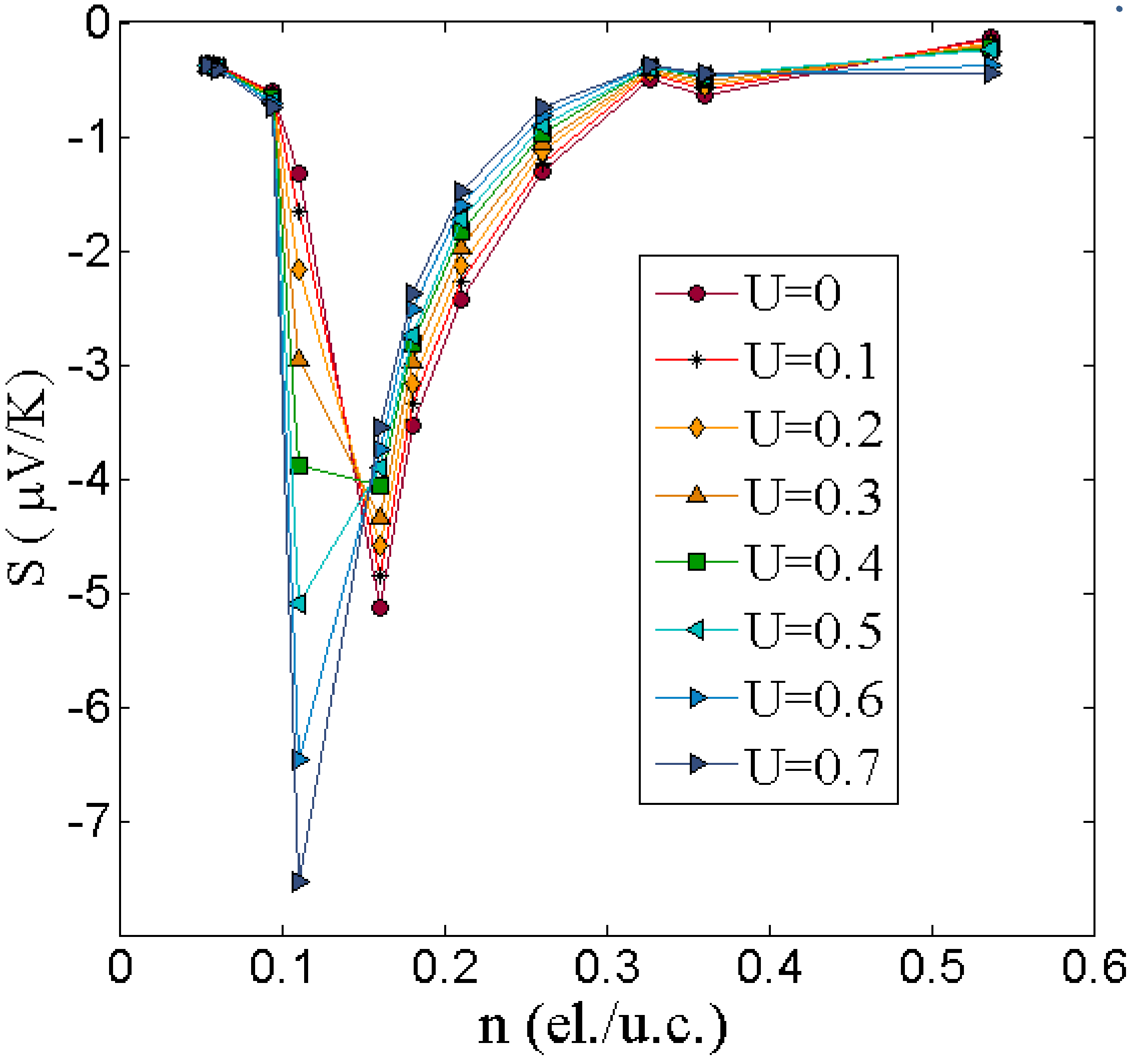

reveals a cusp at n_c for the LT.

With the enhancement in U the cusp shifts towards lower *n* values.

dc conductivity

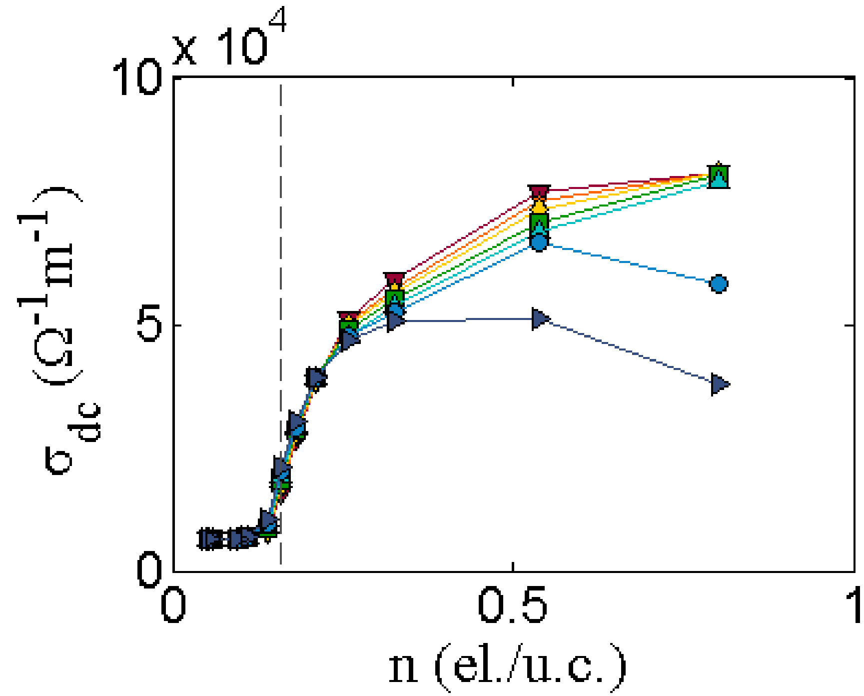

jump arises because a large number of accessible states appear at the Fermi level from the newly occupied orbitals and due to the nearly flat nature of the two lower orbitals above n_c

both the conductivities reduce with increasing U as a consequence of the piling up of the spectral weight

Thermal conductivity

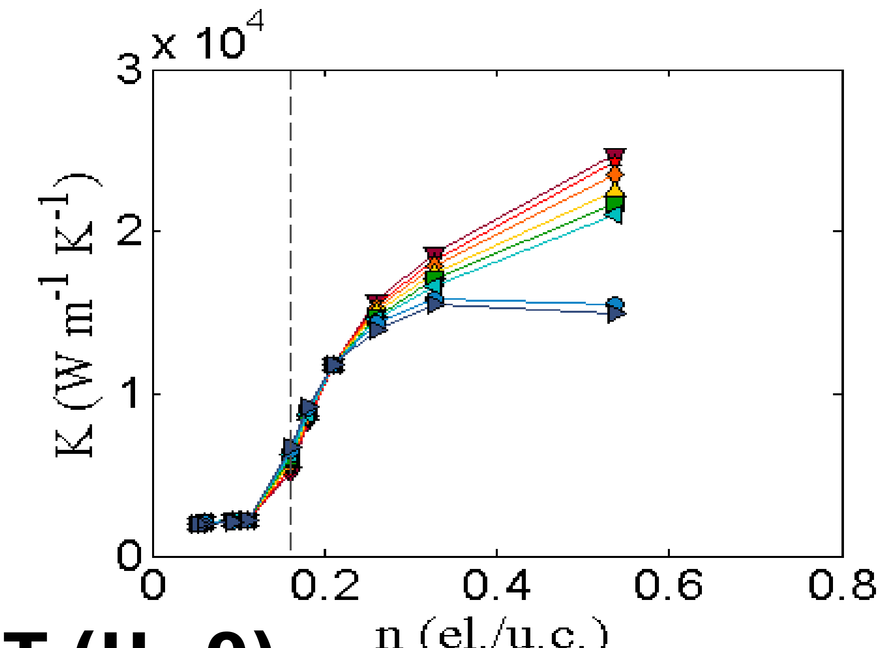

------ line indicates n_c for LT (U=0).

n = 0.0945 el./u.c.

n = 1.4030 el./u.c.

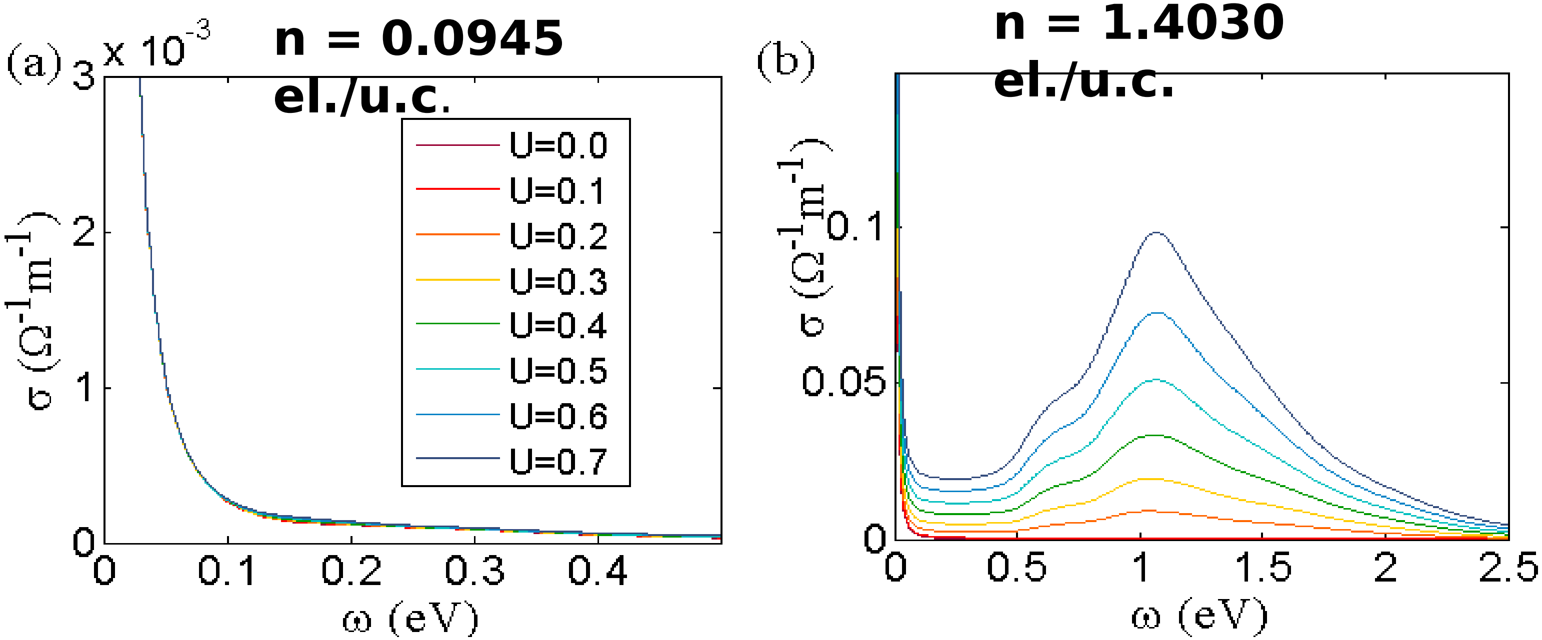

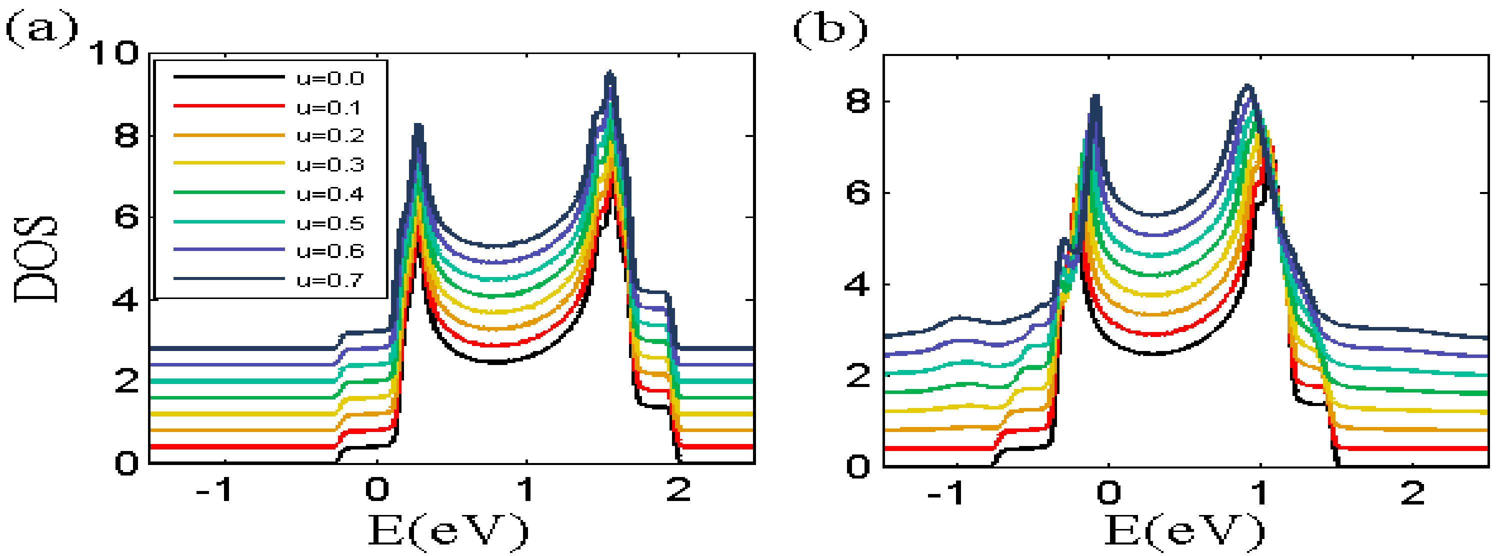

curves from U = 0.1 eV to U = 0.7 eV are progressively offse

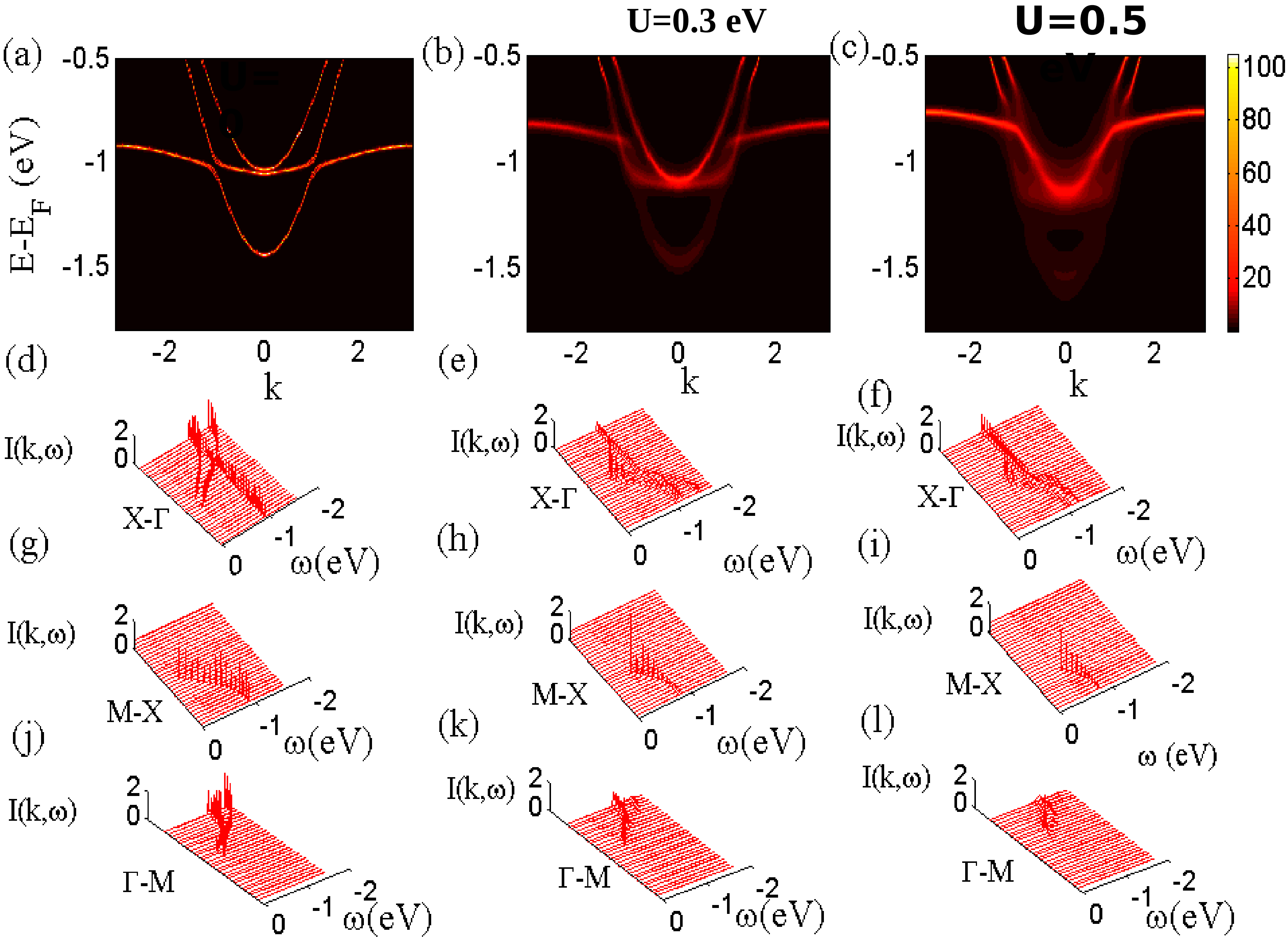

U=0.3 eV
U=0.5
eV
U=
0
(a)
(b)
(c)
(d)
(e)
(f)
(g)
(h)
(i)
(j)
(k)
(l)
E-E_F (eV)
k
I(k,ω)
X-Γ
M-X
Γ-M
ω(eV)
100
80
60
40
20

$$I(\mathbf{k},\omega) \propto \frac{Im\Sigma(\omega) f(\omega)}{[\omega - \epsilon_k - Re\Sigma(\omega)]^2 + [Im\Sigma(\omega)]^2}$$

With correlation the weight transfers over finite energy window.

around the Γ point

For the d_{xy} orbital $\rightarrow$ spectral weight gets transferred over an energy range of 0.15 eV and 0.3 eV for U = 0.3 eV and 0.5 eV respectively.

d_{xz} and d_{yz} orbitals $\rightarrow$ the spectral weights get transferred over an energy scale of 0.2 eV and 0.4 eV for U = 0.3 eV and 0.5 eV respectively.

Away from the Γ point

The spectral weight is transferred towards lower energies.

spectral weight transfers towards higher energies

Is there a regime where there

are multiple Lifshitz transitions?

Influence of magnetic field

$h_x = 0$

$h_x = 0.2$ eV

$h_x = 0.4$ eV

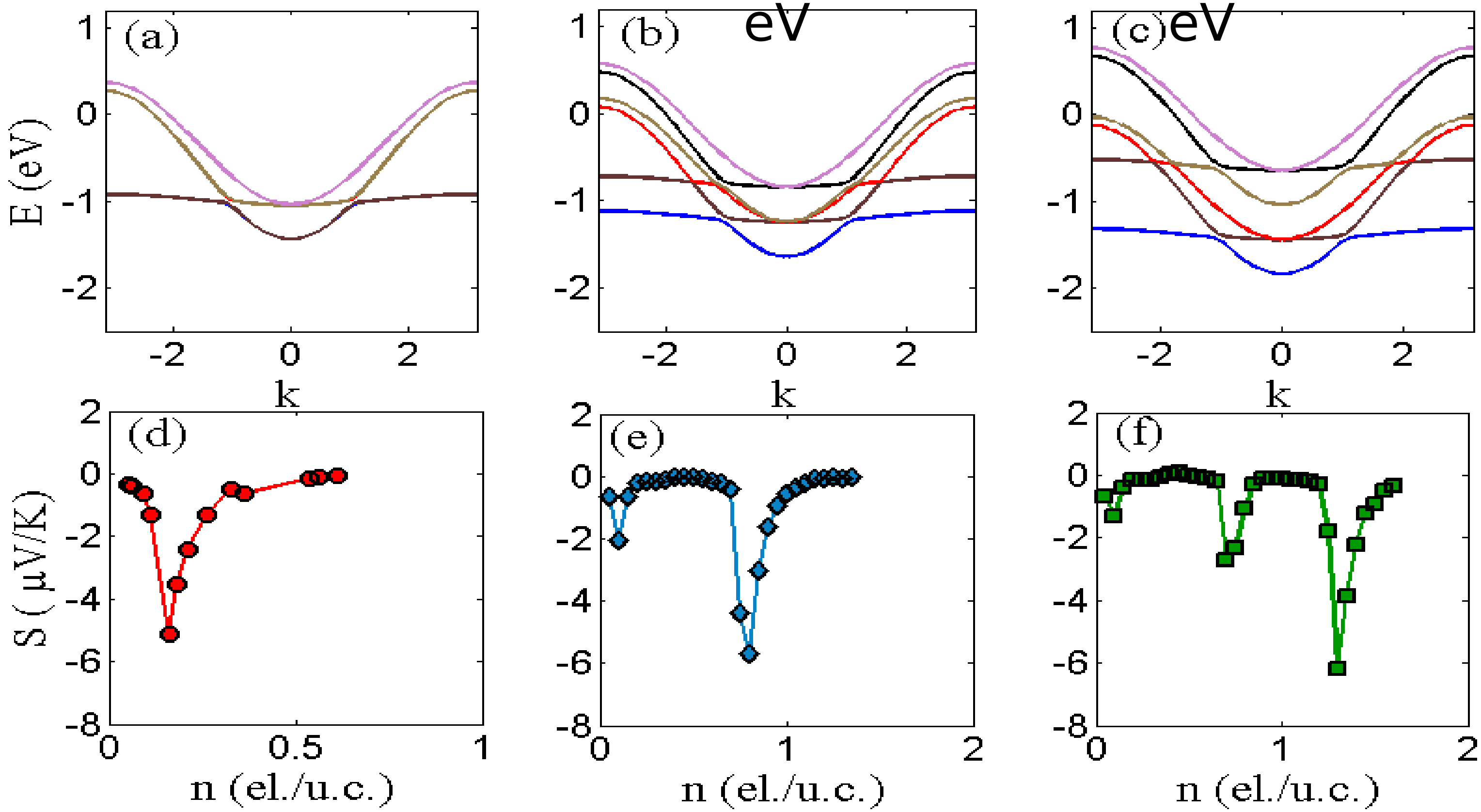

H applied along x axis.

With a finite field → $h_z = 0$; $h_y = 0$

degeneracy is lifted at all

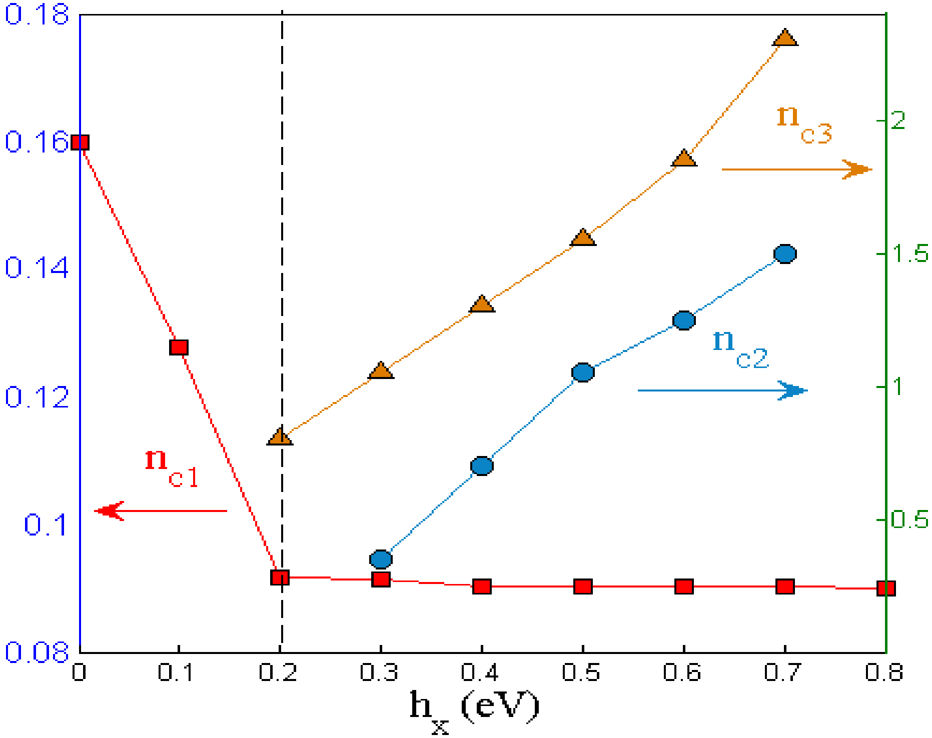

Two clear regimes of field strength:

low field regime (h_x < 0.2 eV)

only one kind of LT

n_{c1} decreases with increasing h_x

high field regime (h_x >= 0.2 eV)

multiple transitions appear

n_{c2} and n_{c3} increase with increasing h_x

n_{c2} and n_{c3} originally coincide with n_{c1} at lower fields and get separated with increasing h_x due to the removed degeneracy at the Γ point.

The third LT occurs at lower fields than the second transition.

magnetic field applied perpendicular to the interface

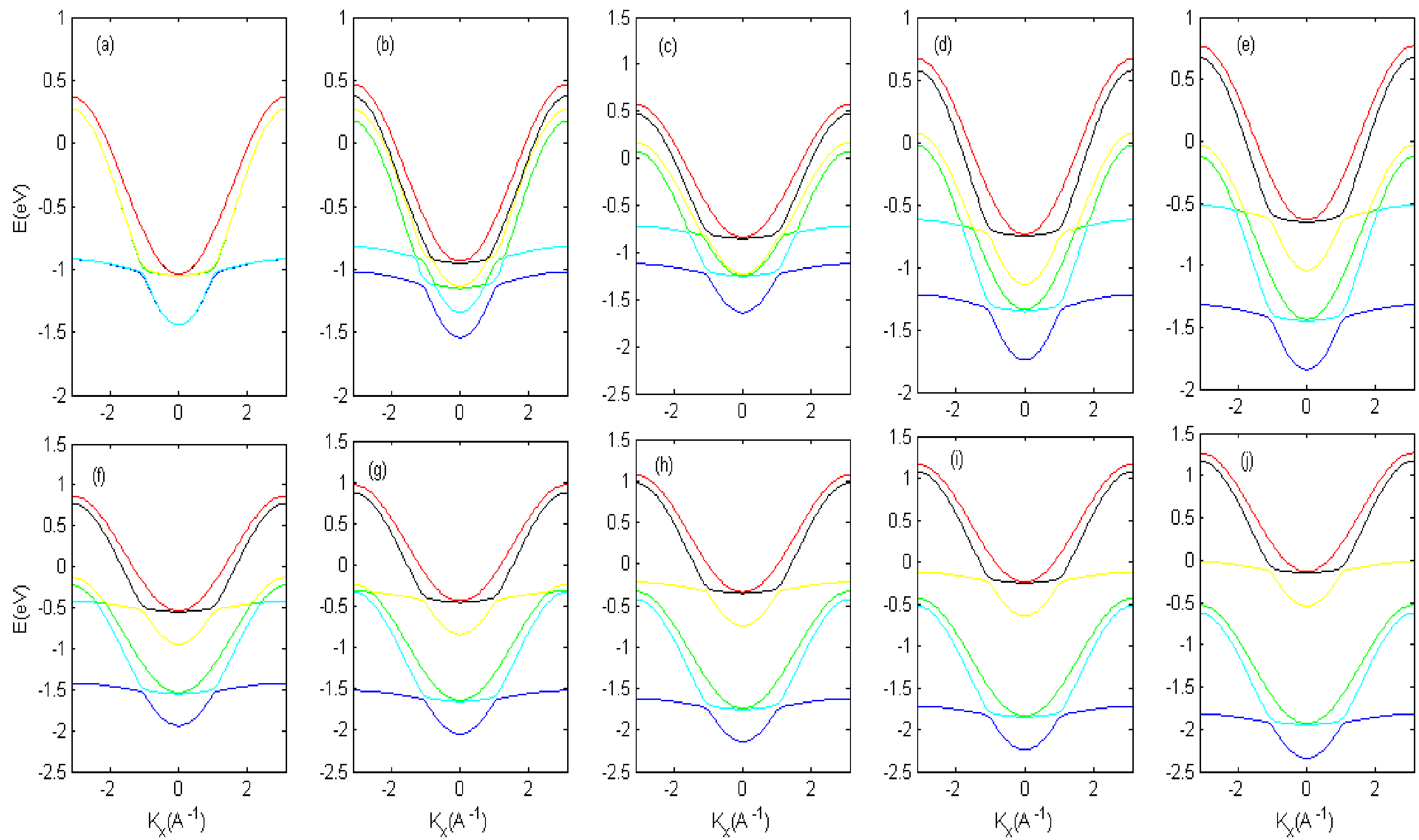

Similar to

LT: Conclusions

The LT occurs when new carriers from the d_{yz} and d_{zx} orbitals populate the Fermi level and new electron-like pockets appear at the Fermi surface.

The change in the Fermi surface topology appears as a jump in the dc and thermal conductivities and as a cusp in the Seebeck coefficient.

The repulsive electron-electron interaction reduces the n_c for the transition.

In the presence of external magnetic field, the n_c further reduces with increasing field strength and multiple transitions appear at sufficiently large fields.

The problem is hard, experimentally even more, but

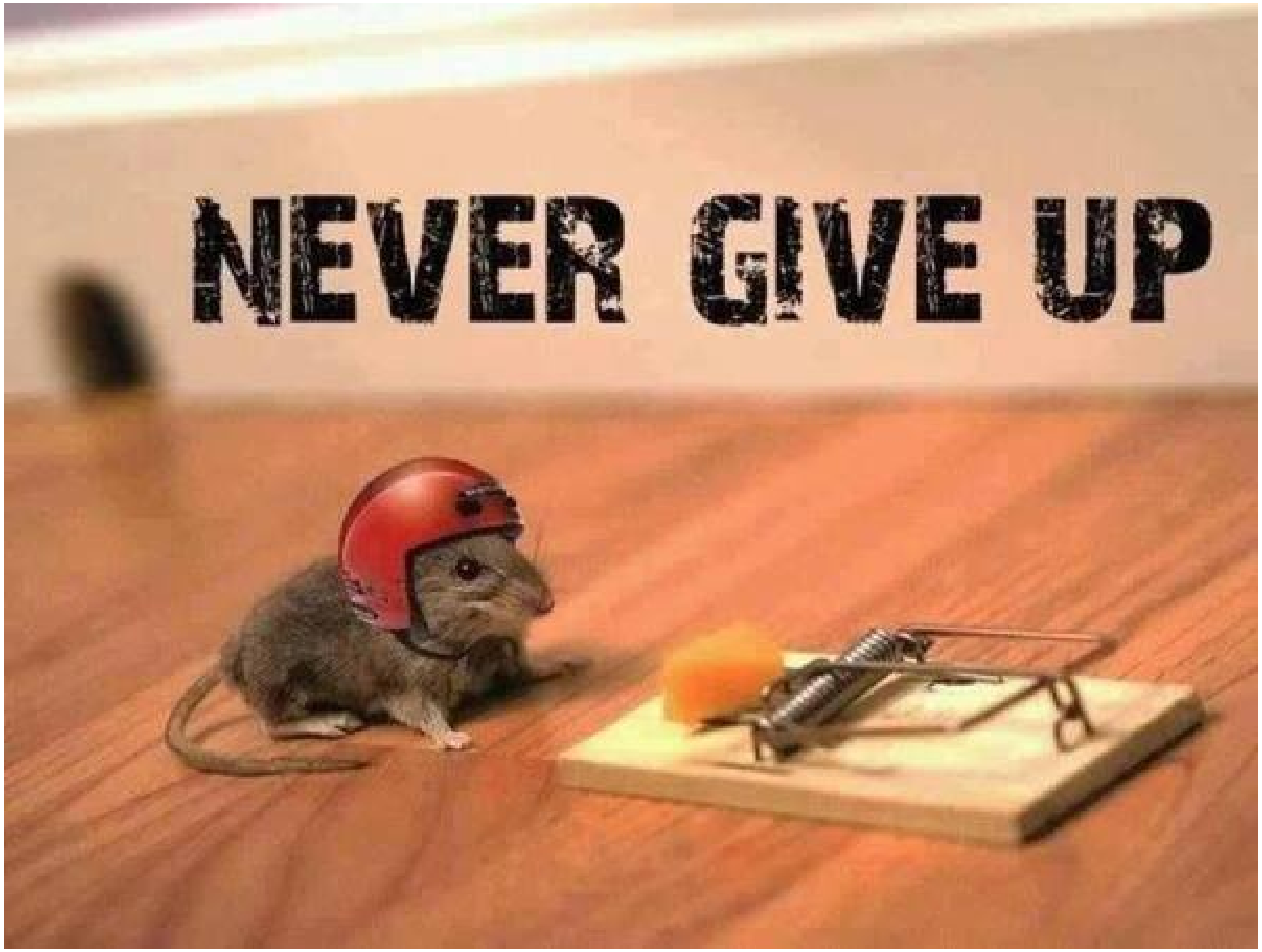


Thank You..